Fe_8N_x Thin Films and Nanoparticles: from Intrinsic Properties Towards Magnetic Applications

Fe_8N_x dünne Schichten und Nanopartikel: von intrinsischen Eigenschaften zu magnetischer Anwendungen

Zur Erlangung des Grades eines Doktors der Naturwissenschaften (Dr. rer. nat.)
genehmigte Dissertation von M. Sc. Imants Dirba aus Riga
Tag der Einreichung: 23 March 2017, Tag der Prüfung: 22 May 2017
Darmstadt 2017 — D 17

1. Gutachten: Prof. Dr. Oliver Gutfleisch
2. Gutachten: Prof. Dr. Rainer Niewa

TECHNISCHE
UNIVERSITÄT
DARMSTADT

Fachbereich Material- und Geowissenschaften
Fachgebiet Funktionale Materialien

Fe_8N_x Thin Films and Nanoparticles: from Intrinsic Properties Towards Magnetic Applications
Fe_8N_x dünne Schichten und Nanopartikel: von intrinsischen Eigenschaften zu magnetischer Anwendungen

Genehmigte Dissertation von M. Sc. Imants Dirba aus Riga

1. Gutachten: Prof. Dr. Oliver Gutfleisch
2. Gutachten: Prof. Dr. Rainer Niewa

Tag der Einreichung: 23 March 2017
Tag der Prüfung: 22 May 2017

Darmstadt 2017 — D 17

Bitte zitieren Sie dieses Dokument als:
URN: urn:nbn:de:tuda-tuprints-62591
URL: http://tuprints.ulb.tu-darmstadt.de/6259

Erklärung zur Dissertation

Hiermit versichere ich, die vorliegende Dissertation ohne Hilfe Dritter nur mit den angegebenen Quellen und Hilfsmitteln angefertigt zu haben. Alle Stellen, die aus Quellen entnommen wurden, sind als solche kenntlich gemacht. Diese Arbeit hat in gleicher oder ähnlicher Form noch keiner Prüfungsbehörde vorgelegen.

Darmstadt, den

(M. Sc. Imants Dirba)

Abstract

Iron nitride Fe_8N_x could potentially provide an environmentally friendly and resource-efficient functional magnetic material in the areas of permanent magnets, magnetic recording as well as biomedical applications. Despite the amount of research within the last decades, questions remain on whether or not the intrinsic magnetic properties are sufficient and if they can, by sustainable means, be engineered into the useful extrinsic properties. Another key issue is the phase stability in different environments which needs a thorough investigation.

In this thesis, the Fe_8N_x material synthesis, an analysis of structure and the corresponding magnetic properties, particularly in thin films and nanoparticles, are presented. The focus lies first on the fabrication of buffer-free, phase-pure α'-Fe_8N_x and α''-$Fe_{16}N_2$ samples in order to converge towards an unambiguous interpretation of the observed physical phenomena. The main aim of this work is to study the magnetic properties, the thermal stability and consequently feasibility for the proposed applications, by performing advanced synthesis and in-depth characterization of high-quality α'-Fe_8N_x and α''-$Fe_{16}N_2$ samples.

α'-Fe_8N_x thin films are deposited in the full range of $0 \leq x \leq 1$. The nitrogen incorporation leads to a gradually induced tetragonal unit cell expansion of the compounds which is accompanied by an increase in the magnetic moment, reaching $2.50 \pm 0.09\,\mu_B$ per Fe atom at 10 K. The origin of the increased magnetic moment is solely the lattice expansion. The uniaxial anisotropy constant increases with c/a ratio (or resp. nitrogen content) reaching a value of $0.54\,\mathrm{MJ\,m^{-3}}$ for $c/a \approx 1.1$. The interstitial N atoms play a decisive role in stabilizing the enhanced perpendicular magnetocrystalline anisotropy. These findings can be generalized to other nitrogen containing interstitial Fe alloys.

The second major activity is the development of a novel route with a high-pressure hydrogen reduction step for the synthesis of α''-$Fe_{16}N_2$ nanoparticles. With this route, phase-pure α''-$Fe_{16}N_2$ nanoparticles are successfully synthesized and characterized. The $M_s(0)$ for α''-$Fe_{16}N_2$ nanoparticles is found to be $215\,\mathrm{Am^2kg^{-1}}$ and coercivity $\mu_0 H_c = 0.22\,\mathrm{T}$. Fe-O shells form around the particles when exposed to atmosphere which leads to a reduced magnetization.

Overall the Fe_8N_x alloys are shown to possess semi-hard magnetic properties as well as relatively poor phase stability, which has direct consequences on applications, such as bulk permanent magnets, nanocomposites and magnetic nanoparticle hyperthermia.

Zusammenfassung

Der Werkstoff Eisennitrid Fe_8N_x ist ein potentieller Kandidat für ein umweltfreundliches und ressourceneffizientes Funktionsmaterial mit Anwendungsmöglichkeiten als Permanentmagnet, magnetischer Datenträger oder in biomedizinischen Anwendungen. Trotz eines nicht unerheblichen Forschungsaufwandes in den letzten Jahrzehnten bleibt die Frage, ob die intrinsischen magnetischen Eigenschaften ausreichend sind um die erwünschten extrinsischen Eigenschaften durch geeignete Verarbeitung erreicht zu können. Zusätzlich bedarf es weiter Untersuchungen hinsichtlich der Phasenstabilität unter verschiedenen Umwelteinflüssen.

In der vorliegenden Arbeit wird eine Reihe an Erkenntnissen zur Materialsynthese, der Struktur und den zugehörigen magnetischen Eigenschaften vorgestellt, insbesondere anhand von Dünnschichten und Nanopartikeln. Das Augenmerk liegt auf der Herstellung von phasenreinen α'-Fe_8N_x und α''-$Fe_{16}N_2$ Proben die ohne zusätzliche epitaktische Vermittlungsschicht auskommen, um eine unverfälschte Interpretation auftretender physikalischer Effekte zu ermöglichen. Hauptziel dieser Arbeit ist daher, die magnetischen Eigenschaften und thermische Stabilität näher zu beleuchten und somit die Machbarkeit der vorgestellten Anwendungen zu evaluieren. Dies wurde durch Synthesemethoden und ausführlicher Charakterisierung von hochqualitativen α'-Fe_8N_x und α''-$Fe_{16}N_2$ Proben erreicht.

Es wurde eine vollständige Probenreihe von α'-Fe_8N_x mit $0 \leq x \leq 1$ in Form von Dünnschichten abgeschieden. Die Inkorporation von Stickstoff führt zu einer kontinuierlich steigenden, tetragonalen Gitterverzerrung der Einheitszelle, was mit einer Vergrößerung des magnetischen Moments bis hin zu $2.50 \pm 0.09\,\mu_B$ pro Eisenatom bei 10 K einhergeht. Die Ursache für das zunehmende magnetische Moment liegt alleine in der Gitteraufweitung. Die uniaxiale Anisotropiekonstante nimmt mit steigendem c/a Verhältnis (bzw. der Menge an Stickstoff) zu bis hin zu einem Wert von $0.54\,\mathrm{MJ\,m^{-3}}$ für $c/a \approx 1.1$. Die interstitiellen Stickstoffatome spielen eine entscheidende Rolle bei der Stabilisierung der erhöhten perpendikulären magnetokristallinen Anisotropie. Diese Erkenntnisse können verallgemeinert und auf andere stickstoffhaltige Eisenlegierungen übertragen werden.

Eine neue Syntheseroute für die Synthese von α''-$Fe_{16}N_2$ wird erstmalig vorgestellt. Diese beinhaltet einen Zwischenschritt, in welchem Eisenoxid unter Hochdruck per Wasserstoffreduktion zu α-Fe reduziert wird. Mit dieser Route ist es möglich phasenreine α''-$Fe_{16}N_2$ Nanopartikel erfolgreich zu synthetisieren und charakterisieren. Die $M_s(0)$ für α''-$Fe_{16}N_2$ Nanopartikel wurde zu $215\,\mathrm{Am^2kg^{-1}}$ bestimmt, während für die Koerzitivfeldstärke $\mu_0 H_c = 0.22\,\mathrm{T}$ gemessen wurde. Die Partikel bilden bei Kontakt mit Luft eine Hülle aus Fe-O an der Oberfläche, was zu einer herabgesetzten Magnetisierung führt.

Zusammenfassend besitzen die Fe_8N_x Legierungen semi-harte magnetische Eigenschaften und eine relativ geringe Phasenstabilität, was direkte Konsequenzen in Bezug auf die vorgestellten Anwendungen hat.

Contents

List of Figures

Nomenclature

$(BH)_{max}$	Maximum energy product
χ	Tilting axis
$\Delta\mu_L$	Variation in orbital moments along the different magnetization directions
$\Delta_f G^0$	Standard Gibbs free energy of formation
$\Delta_f H^0$	Standard enthalpy of formation
Δ_i	Atomic magnetic anisotropy contributions
δ_w	Domain wall width
λ	Wavelength
$\mathcal{J}$	Exchange integral
μ_0	Permeability of free space
μ_B	Bohr magneton
μ_N	Nuclear magneton
ω	Angular frequency
ϕ	In-plane rotation axis
τ	Effective relaxation time
ξ	Atomic spin-orbit coupling
A	Exchange stiffness parameter
a, b, c	Lattice parameters
D	Nitrogen atom ordering parameter
D_{sp}	Critical superparamagnetic particle diameter
E_a	Anisotropy energy

E_{ij}^{exch}	Interatomic exchange interaction energy
E_{ms}	Magnetostatic energy density
f	Frequency
g	Landé factor
h	Planck constant
H_a	Anisotropy field
H_c	Coercive field
H_d	Demagnetization field
H_N	Nucleation field
H_w	Write field
K	Anisotropy constant
k	Magnetic hardness parameter
k_B	Boltzmann constant
K_r	Reaction constant
l_{ex}	Exchange length
M_r	Remanent magnetization
M_s	Saturation magnetization
$M_s(0)$	Saturation magnetization extrapolated to 0 K
N_d	Demagnetization factor
P_H	Dissipated heat power
Q	Number of atoms per unit cell
R	Gas constant
r_4	Tetrahedral interstitial site
r_6	Octahedral interstitial site
r_{ab}	Inter-atomic separation

r_d	d-orbital radius
R_{sd}	Single-domain radius
S	Electron spin
T	Temperature
t	Film thickness
T_C	Curie temperature
V	Volume
X_{N}	Number of interstitial N atoms per 100 Fe atoms
Z	Number of nearest neighbors
bcc	Body-centered cubic
bct	Body-centered tetragonal
DFT	Density functional theory
DOS	Density of states
EELS	Electron energy-loss spectroscopy
HAADF	High-angle angular dark-field
MAE	Magnetic anisotropy energy
MFM	Magnetic force microscopy
PMA	Perpendicular magnetic anisotropy
SEM	Scanning electron microscopy
SIMS	Secondary ion mass spectroscopy
SPD	Singular point detection
SQUID	Superconducting quantum interference device
STEM	Scanning transmission electron microscope
TEM	Transmission electron microscope
VSM	Vibrating sample magnetometer

XPS	X-ray photoelectron spectroscopy
XRD	X-ray diffraction
XRR	X-ray reflectometry

1 Introduction

Magnetism and magnetic materials have always fascinated the human mind and in many aspects shaped the world as we see it today. Already thousands of years ago our ancestors were amazed by the properties of lodestones [1] and its application in the compass was a significant advancement in ship navigation in comparison to earlier navigation by the position of the stars. Centuries later, in 1820, the discovery by Oersted that an electrical current moves a compass needle [2] lead to the development of electric motors and generators catalyzing the second industrial revolution. In mid-twentieth century magnetism provided a way for another major breakthrough without which our lives today cannot be imagined - magnetic recording. Starting from magnetic tapes and the first hard disk drives, storage densities have increased at an annual rate of 40 % [3].

Recent emphasis on the green energy technologies, stimulated by the growing concern about human influence on the global warming [4] as well as geopolitical concerns, have drawn significant attention to resource and energy efficient hard magnetic materials. Applications, such as electric transportation and electric power generation by wind, rise the demand for high-performance permanent-magnets. The energy density of modern permanent magnet materials doubled every 14 years [5], increasing from about $10\,\mathrm{kJ\,m^{-3}}$ in Alnicos (1932) and about $36\,\mathrm{kJ\,m^{-3}}$ in hard ferrites introduced in 1950's to about $400\,\mathrm{kJ\,m^{-3}}$ in modern rare-earth magnets [6]. Nd-Fe-B magnets show the highest energy product and thus are relevant for a variety of energy-related and other industrial applications [7]. However, after the rare-earth crisis [8], the search for alternative materials without rare-earths has regained attention [9]. One approach is to investigate new magnets with moderate performance that could fill the maximum energy product gap between hard ferrites and rare-earth permanent magnets [10].

Another emerging field of application for magnetic materials, especially ferromagnetic and superparamagnetic nanoparticles, is biomedicine [11]. For example, magnetic nanoparticles could be used as vectors for targeted drug delivery [12, 13], contrast agents for magnetic resonance imaging (MRI) [14] and heating media for magnetic hyperthermia cancer therapy [15, 16, 17]. Here mostly iron oxides have been dominating due to their reasonable magnetic properties, bio-compatibility and chemical stability.

These already established and continuously advancing as well as newly emerging applications demonstrate that even though to the outward world not always as visible as silicon, magnetic materials play a fundamental role in the scientific and technological progress of humanity. Accordingly, a quest for high-performance, from geopolitical and economic perspective sustainable magnetic materials, is and will be an on-going challenge in all those above mentioned areas.

In this work, the focus is on one such material, namely iron nitride α'-Fe_8N_x/α''-$Fe_{16}N_2$. It consists only of iron and nitrogen which are both cheap, abundant and non-toxic, and would thus provide a recyclable, environmentally friendly and resource-efficient functional magnetic material. The α''-$Fe_{16}N_2$

has been reported to possess high saturation magnetization M_s [18] as well as a significant uniaxial magnetocrystalline anisotropy K_u [19] and therefore has been suggested as a possible rare-earth-free permanent magnet candidate [20, 21, 22, 23], as well as a semi-hard phase in hard-soft composite magnets [24]. The enhanced magnetocrystalline anisotropy also could enable reduction of the grain size without reaching the critical superparamagnetic limit which is crucial for magnetic recording. Consequently, the α''-$Fe_{16}N_2$ phase has been recognized as a potential candidate for high density recording [25]. Both high magnetization and anisotropy, as well as the potential bio-compatibility indicate that α''-$Fe_{16}N_2$ could possibly be developed as a perspective material for biomedical purposes [26].

These applications require control over the particle size and corresponding magnetic properties on the nanometer scale. Therefore, this thesis aims to study the synthesis and characterization of α'-Fe_8N_x and α''-$Fe_{16}N_2$ in a form of thin films and nanoparticles.

From the above it might seem that the α''-$Fe_{16}N_2$ phase provides kind of a "holy grail" of magnetic technology being promising for various and quite different applications. In reality however, there are fundamental problems concerning the synthesis of phase-pure material, thermal stability and even despite numerous works for decades, the intrinsic magnetic properties are still under debate, triggering phrases like, "α''-$Fe_{16}N_2$ is one of the most fantastic and mysterious materials in the field of magnetism for over 25 yrs because it is not clear whether 'its giant magnetic moment is true or not'" [27], and, "Magic moments in magnetism" [28], by prominent scientists in the magnetism community.

In this light a legitimate question to ask is, how is this work going to make a difference? American writer R. M. Brown wrote that, "Insanity is doing the same thing over and over again, but expecting different results" [29]. Considering all the previous works done on synthesis and characterization of α''-$Fe_{16}N_2$, one should ask if and what can be done better in the present study, otherwise it would simply result in a repetition of the same experiments conducted by many other researchers in past, but expecting to obtain better results. Therefore, explicit research goals to be accomplished by the current thesis have been defined, which in case of success should elucidate the above mentioned controversial issues in the α'-Fe_8N_x/α''-$Fe_{16}N_2$ system:

1. Synthesis and characterization of buffer-free α'-Fe_8N_x, α''-$Fe_{16}N_2$ thin films followed by accurate measurements of the saturation magnetization and the corresponding magnetic moment.

2. Investigation of the development of the magnetocrystalline anisotropy in α'-Fe_8N_x.

3. Estimation of the Curie temperature in α'-Fe_8N_x and α''-$Fe_{16}N_2$

4. Investigation of the influence of N site ordering on the magnetic properties of α'-Fe_8N_x.

5. Synthesis and characterization of phase-pure, fine α''-$Fe_{16}N_2$ nanoparticles, performing a comprehensive set of measurements, including neutron diffraction, in order to properly interpret the magnetic properties and account for significantly scattered values reported in the literature.

6. Investigation of the thermal stability of α'-Fe_8N_x, α''-$Fe_{16}N_2$.

7. Correlating the observed magnetic properties with the proposed potential applications.

The main aim of this work is therefore, by performing advanced synthesis of α'-Fe_8N_x and α''-$Fe_{16}N_2$ samples in a phase-pure form and in-depth characterization, to understand better the magnetic properties, thermal stability and consequently feasibility for the proposed applications.

Structure of the thesis

Chapter 2 gives a general overview on interstitial iron nitrides with a focus on structure and magnetic properties of the primary α'-Fe_8N_x and the secondary α''-$Fe_{16}N_2$ iron-nitrogen martensites in particular. It provides a historical reflection upon the quest on synthesis of high-quality samples and understanding of the magnetic properties in α' and α''.

The experimental sample preparation and characterization techniques used in this thesis are described in Chapter 3.

Chapters 4 and 5 present the results on γ'-Fe_4N and α'-Fe_8N_x thin films deposited by RF magnetron sputtering onto MgO substrates. The focus here is on the intrinsic magnetic properties. Interpretation of the development of the magnetic moment and perpendicular magnetic anisotropy in α'-Fe_8N_x is provided.

Chapter 6 describes synthesis and characterization of phase-pure α''-$Fe_{16}N_2$ nanoparticles. A novel route with high-pressure hydrogen reduction step for lowering the processing temperature, thus avoiding the disadvantageous particle coalescence is demonstrated for the first time.

Finally, based on the magnetic properties explored in previous chapters, the feasibility of the Fe_8N_x phases for the proposed applications, such as magnetic recording, permanent magnets and magnetic hyperthermia is critically assessed.

Conclusions from the conducted research and outlook for further studies is given at the end of the thesis.

This thesis merges materials from author's publications during the thesis time. Numerous figures have been adapted/used directly as well as several passages have been rewritten or used verbatim from these individual studies. Chapter 4 presents results from Reference [30]. Chapter 5 uses material from [31] as well as Reference [32] done in collaboration with Jun. Prof. H. Zhang at the TU Darmstadt, Theory of Magnetic Materials research group. Chapter 6 is largely based on Reference [33].

2 Interstitial iron nitrides

Nitriding (introduction of atomic nitrogen into the target material) process was developed in early 1900s in US [34] and Germany [35]. Ever since it has served as one of the most versatile, simple and efficient surface hardening techniques of iron-based materials [36].

Extensive studies on iron-nitrogen system have been done in mid-last century [37, 38, 39, 40, 41, 42]. The Fe-N phase diagram has been well established and the one summarized by Jack [41], with additional illustrative schematics of the crystal structures of interstitial magnetic iron nitrides relevant for this work is shown in Figure 2.1.

Interstitial alloys will be discussed throughout this thesis therefore it is useful to define its meaning in the beginning. They are alloys where small atoms, such as H, C, N, B, are incorporated in the empty voids between the host metal atoms. Depending on the size of the interstitial atom and the corresponding geometry, this can lead to a distortion of the parent phase lattice.

For better understanding of the iron nidrides formed, an insight into the polymorphism of Fe is helpful.

At atmospheric pressure iron has two different crystal structures: α-Fe (bcc, stable at room temperature, ferromagnetic up to T_C =1041 K) and γ-Fe (fcc, stable in range 1184 K–1665 K, nonmagnetic). Under high pressures also the third, ϵ-Fe (hcp, stable above around 13 GPa [43], nonmagnetic) exists. The information about the different phases is summarized in Table 2.1 (data from [44] and the respective references).

Each of these allotropes is forming (and even stabilized by interstitial N) an interstitial nitride phase with the corresponding structures shown in Figure 2.1. The focus of the present thesis is on the synthesis and magnetic properties of the low-nitrogen-content (up to roughly 11 at.% or 3 wt.% nitrogen) part of the phase diagram (the lower left corner in Figure 2.1), representing α-Fe, α'-Fe_8N_x and α''-$Fe_{16}N_2$ phases. The next one towards higher N content, the γ'-Fe_4N will be briefly studied in Chapter 4 in form of thin films and the ϵ-Fe_3N will only appear as an impurity phase in Chapter 6, and therefore will not be described in detail in the following sections. A first site occupancy estimation for the interstitial light elements in the polymorphs of iron can be obtained by treating the atoms as rigid spheres and the crystals as periodic stacks of these spheres.

Table 2.1: Allotropy of Fe.

Phase	Structure	Stability	Magnetism	Reference
α-Fe	bcc, Im-3m (229), a =2.865 Å	Ambient	Ferromagnetic	[45]
γ-Fe	fcc, Fm-3m (225), a =3.571 Å	1184 K–1665 K	Nonmagnetic	[41]
ϵ-Fe	hcp, P63/mmc (194), a =2.473 Å; c =3.962 Å	>13 kbar	Nonmagnetic	[46]

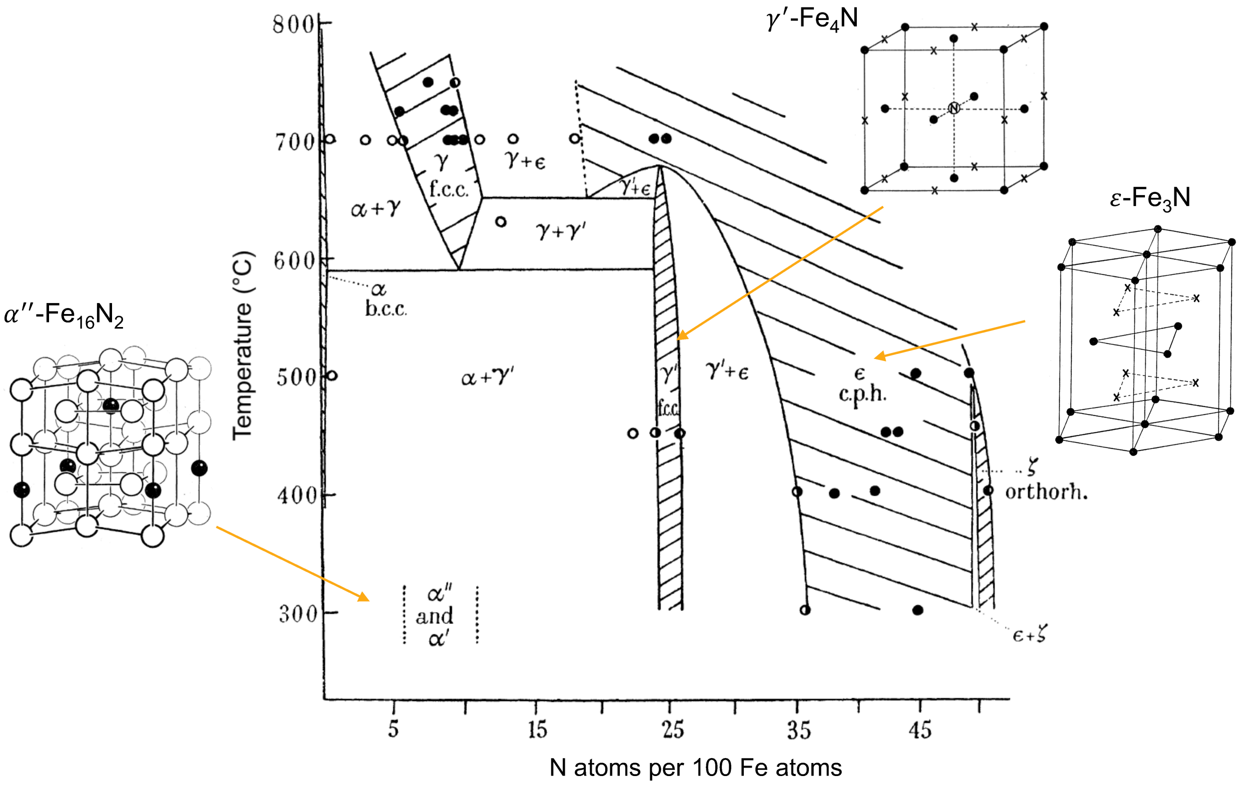

Figure 2.1: The iron-nitrogen phase diagram and the corresponding crystal structures according to Jack [40, 47, 41].

In close-packed structures, such as, face-centered cubic (fcc) and hexagonal close-packed (hcp) the spheres are packed as tightly as possible resulting in the maximum theoretical packing density of 74 % with the remaining 26 % of the space being divided between the *octahedral*, r_6 (subscript refers to the coordination number) and *tetrahedral*, r_4 interstitial sites. As an example, the octahedral interstitial sites for bcc α-Fe and fcc γ-Fe are shown in Figure 2.2. Purely by geometrical considerations one can show that in fcc structure $r_6 = 0.414R$ and $r_4 = 0.225R$ (here R stands for the radius of the host atoms), which denotes the radii of the maximum sphere size which can be accommodated by an interstice without distorting the host lattice.

The body-centered cubic (bcc) is less closely packed and has a filling factor of 68 %, consequently leaving slightly more space, 32 %, for r_6 and r_4 interstitial sites. Sizes of both interstices for γ and α iron is given in Table 2.2.

Table 2.2: Atomic radii and sizes of interstitial sites in α-Fe and γ-Fe (adapted from [48]).

Phase	R (Å)	r_6 (Å)	r_4 (Å)
α-Fe (bcc)	1.24	0.19	0.36
γ-Fe (fcc)	1.27	0.53	0.29

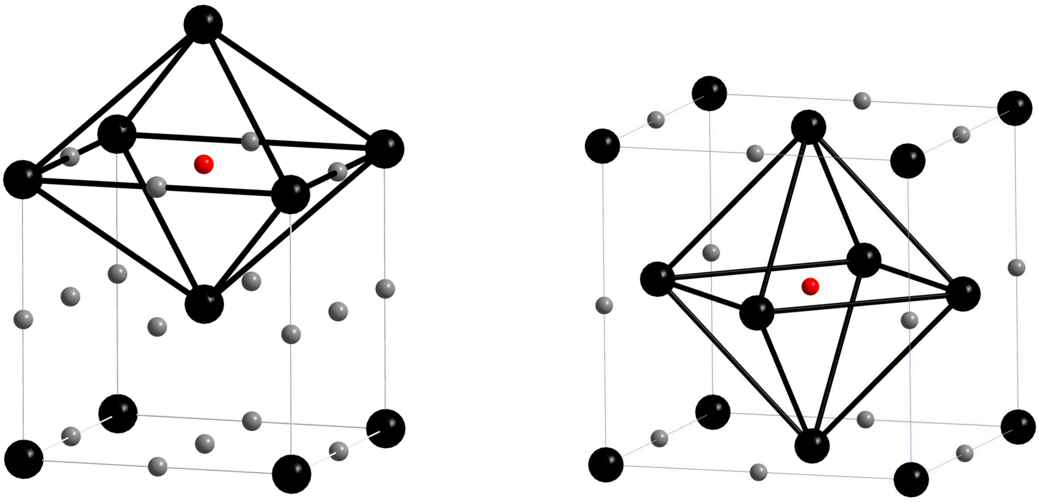

Figure 2.2: Positions of the octahedral interstitial sites in bcc and fcc lattices with the corresponding iron octahedra occupied by N atom in α'-Fe_8N_x (left) and γ'-Fe_4N (right) phases (adapted from [44]).

2.1 The γ'-Fe_4N phase

γ'-Fe_4N has a fcc structure similar to that of γ-Fe with a nitrogen atom occupying the center of the cube (as illustrated in Figure 4.1). This results in an isotropic expansion of the unit cell with a corresponding lattice constant of $a = 3.79\,\text{Å}$. The crystal structure, as obtained from x-ray diffraction on single crystals grown by high pressure ammonolysis, is cubic $Pm\overline{3}m$ (space group No. 221), where the nitrogen occupies in an ideally ordered sample the corner sharing ocathedra of the iron atoms at the face centered site ($3b$) [49]. While γ-Fe is ‚non-magnetic', it was immediately recognized that γ'-Fe_4N has a large magnetic moment, comparable to α-Fe. It had already been suggested for γ-Fe based on first principles calculations that there exists a high-spin high-volume state as well as a low-spin low-volume state which are close in energy [50]. Later, a continuous transition from a ferromagnetic state with high-volume to a disordered non-collinear spin configuration with low-volume has been proposed as the origin of the so-called Invar effect [51, 52]. In this line of thinking, γ'-Fe_4N can be regarded as a kind of expanded high-volume γ-Fe having a high-spin state. Even more, since for α-Fe a lattice expansion is predicted to lead to a strong increase of magnetic moment [53], one could speculate that the same effect is present also for γ'-Fe_4N [54].

The magnetic properties of γ-Fe are volume-dependent. This is illustrated in Figure 2.3. The ground state of γ-Fe is antiferromagnetic (AF) and it becomes nonmagnetic under compression. The calculated equilibrium volume is slightly lower than the experimental one (indicated by the blue dashed line). Two ferromagnetic (FM) states are possible - an unstable low-spin (LS) and a stable high-spin (HS) state at expanded volumes. In the HS state, the magnetic moment per Fe atom increases linearly with the volume expansion and reaches about 2.7 μ_B at the position of γ'-Fe_4N (indicated by the orange dashed line).

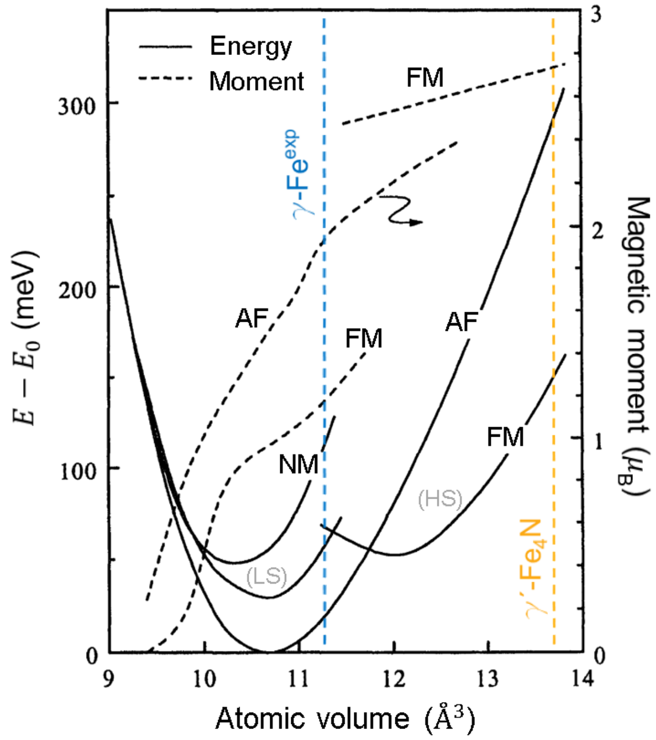

Figure 2.3: The calculated magnetic moment and total energy for γ-Fe as a function of the atomic volume (adapted from [44, 52]). At the atomic volume corresponding to γ'-Fe$_4$N, the γ-Fe would be in the high-spin (HS) state with a magnetic moment of about 2.7 μ_B.

The magnetic properties of γ'-Fe$_4$N made this material interesting for applications in high-density magnetic recording [55]. Also a very high spin polarization of almost 1.0 has been calculated theoretically [56], thus pointing towards possible spin injection applications. A lower value of 0.59 however has been measured experimentally [57].

Numerous reports can be found in literature on the growth and characterization of γ'-Fe$_4$N thin films. A recent comprehensive overview on theoretical and experimental results including bulk and thin films has been provided by Peltzer y Blancá et al.[58]. Unfortunately, experimental results are still differing, in particular with respect to the magnetization. One reason is the non-trivial synthesis of phase-pure samples. Magnetization measurements of γ'-Fe$_4$N thin films vary between a magnetic moment of 2.17 μ_B per Fe atom (fabrication method: RF sputtering in ammonia gas on Si wafers and kapton substrates) [59] and values as high as 2.9 μ_B per Fe atom (fabrication method: DC sputtering in an Ar/N$_2$ gas mixture on LaAlO$_3$ substrates) [60]. This strongly increased magnetic moment has been attributed to the low lattice mismatch between LaAlO$_3$ and γ'-Fe$_4$N [60]. In contrast, based on the magnetization of 10 nm thick films (fabrication method: molecular beam epitaxy on LaAlO$_3$ and MgO) as measured by x-ray magnetic circular dichroism, it has been concluded that the saturation magnetization of about 2.45 μ_B does not depend on lattice strain [61]. From Mössbauer and neutron diffraction studies, a value of approximately 2.25 μ_B per Fe atom has been obtained [62, 63].

With respect to the thermal stability of γ'-Fe$_4$N, it was reported that the highest possible growth temperatures are about 623 K (fabrication method: DC sputtering in Ar/N$_2$ mixture) [64]. But there are also higher growth temperatures up to 723 K reported in literature [60, 61]. In this work, a deposition temperature of 673 K was found to be optimal, however it has to be mentioned that the actual substrate temperature differs from the one measured by the thermocouple and therefore this value should not be considered as absolute.

2.2 The primary Fe-N martensite: α'-Fe$_8$N$_x$

2.2.1 Structural properties

The primary Fe-N martensite α'-Fe$_8$N$_x$ is an interstitial solution of N in bcc α-Fe with $0 \leq x \leq 1$. As discussed before, nitrogen can occupy two different types of interstitial voids in bcc iron. The r_6 sites are located at the midpoints of the unit cell cube edges and centers of the faces as shown in Figure 2.2. In the case of α-Fe (bcc), according to Table 2.2, the tetrahedral r_4 interstitial sites are almost twice as large as the octahedral r_6 ones and therefore could be expected to accommodate the interstitial N atoms. That is however in contradiction with experimental observations on nitrogen-martensite [41, 65], which show that the N atoms prefer the r_6 sites. Another apparent problem is that the reported radius of N atoms is about 0.7 ± 0.1 Å [41] which is much larger than even the r_4 site and thus makes it clear that a crystal distortion is required in order to accommodate nitrogen atoms in α-Fe.

The explanation for the r_6 instead of r_4 occupancy is as follows. In a bcc crystal the two host atoms located directly above and below the face-centered r_6 interstice are relatively close together and therefore less energy is required (by means of simple elasticity considerations based on *Hooke's law*) to stretch them apart than the four atoms surrounding the corresponding r_4 site. Figure 2.4 shows that actually the interstitial N atom in bcc Fe is not occupying only the octahedral, but partially also the four surrounding tetrahedral interstitial sites, pushing the Fe atoms above and below axially apart, which leads to a local lattice expansion along z ([001] in this case) direction and a small contraction within the xy plane resulting in a local tetragonal distortion.

This indeed has been confirmed experimentally [41]. The corresponding evolution of the lattice parameters a and c as well as the induced tetragonality (c/a ratio) as a function of the nitrogen concentration is shown in Figure 2.5. Once the local anisotropic distortion is induced by the interstitial atom, it will alter the local strain distribution and occupation probability for other sites around it. Site occupied along c-axis will inhibit introduction of the next N atom directly above and below it, but will require lower distortion energy for the second atom in the same horizontal plane. As a result, interstitial solutions where all the foreign atoms occupy uniaxial interstices are being formed which is manifested as a macroscopic change of the lattice parameters according to Figure 2.5. The crystal symmetry then is being altered from body-centered cubic to body-centered tetragonal (bct).

Based on the discussion above, the α'-Fe$_8$N$_x$ "phase" can be defined as an interstitial solution of atomic nitrogen in α-Fe, where N atoms occupy with respect to the principal crystal axis similar octahedral sites in a random manner. It has a solubility region of roughly 0-11 at.% N, the lattice parameters vary linearly with the N atom concentration [66] and c/a ratio of about 1.1 is reached at 11 at.% N corresponding to

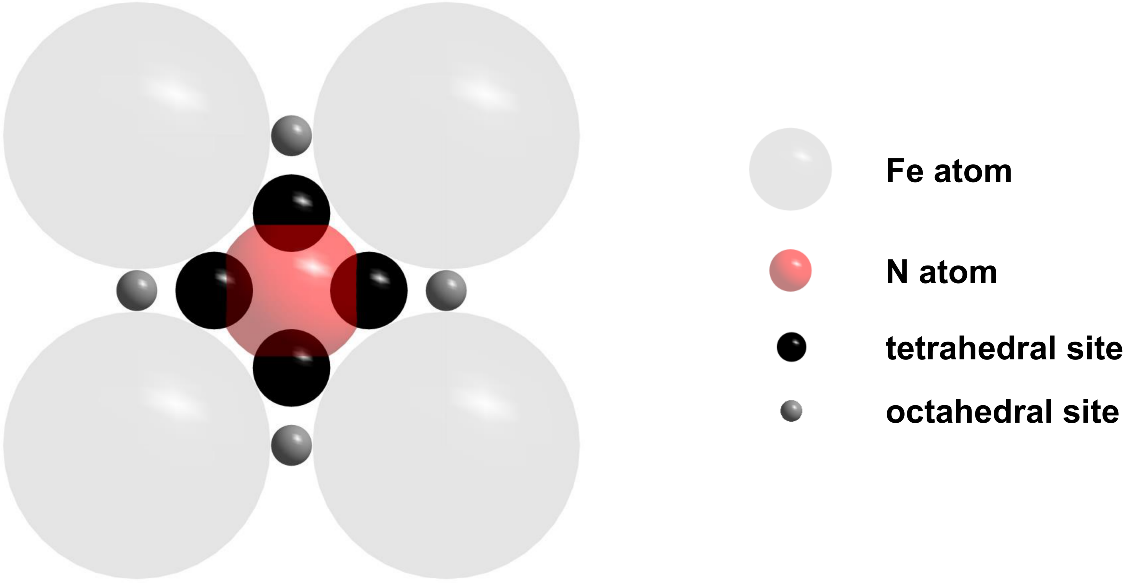

Figure 2.4: Top (001) free view of the unit cell of bcc Fe shown in Figure 2.2 with the sizes of atoms and interstices corresponding to the values presented in Table 2.2 (the figure is to scale). The N atom accupies not only the octahedral, but partially also the four surrounding tetrahedral interstitial sites (adapted from [48]).

α'-Fe_8N_1 composition. The variation of the lattice parameters a and c, c/a ratio as well as the volume (V) per Fe atom can be expressed quantitatively according to Cheng et al. [66] as follows:

$$a = 2.8664 - (0.0017 \pm 0.0002) \cdot X_{\mathrm{N}} \tag{2.1}$$

$$c = 2.8664 + (0.0242 \pm 0.0006) \cdot X_{\mathrm{N}} \tag{2.2}$$

$$c/a = 1 + (0.009 \pm 0.0002) \cdot X \tag{2.3}$$

$$V = 11.776 + (0.085 \pm 0.003) \cdot X_{\mathrm{N}}, \tag{2.4}$$

where X_{N} denotes the number of the interstitial N atoms per 100 Fe atoms.

2.2.2 Magnetic properties

The magnetic moment

As discussed in the previous section, the α'-Fe_8N_x is regarded as a tetragonally expanded derivation from the α-Fe phase. Due to this reason, also its magnetic properties can be understood best when starting from α-Fe as a reference and gradually applying the respective crystallographic distortions.

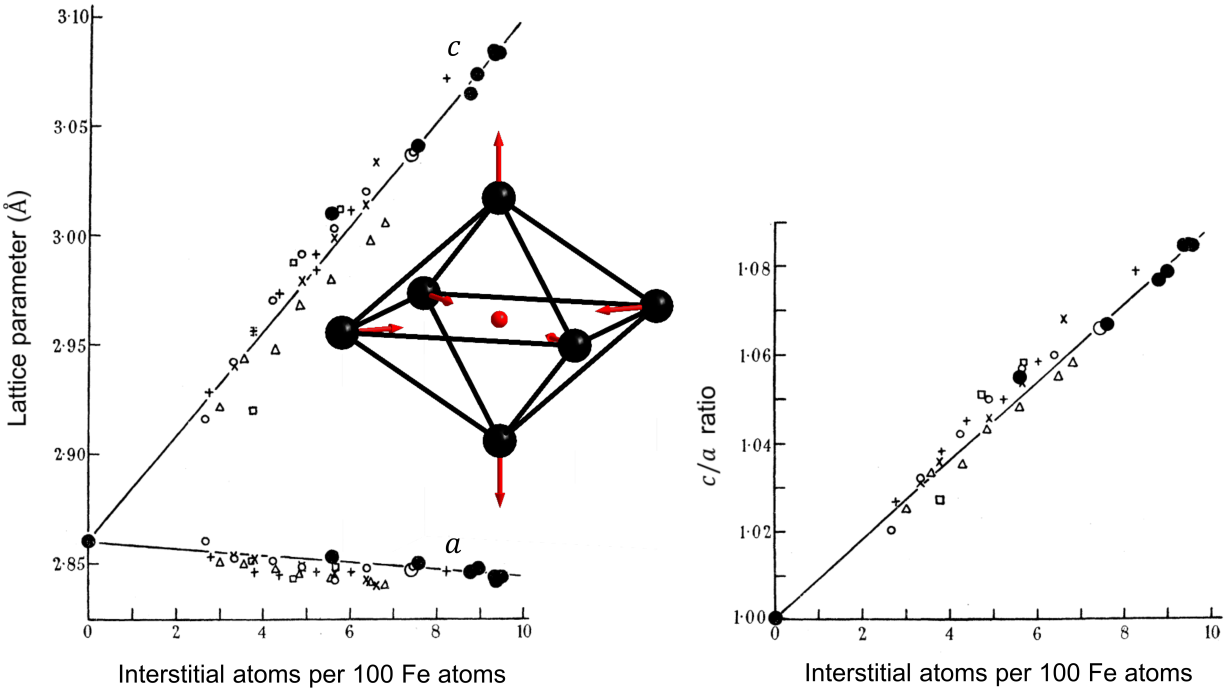

Figure 2.5: Unit cell dimensions and c/a ratios for nitrogen and carbon martensites. The lattice parameters vary lineary with the interstitial atom concentration (adapted from [41]).

Iron is the 26th element in the Periodic table with the electron configuration of $1s^2\ 2s^2\ 2p^6\ 3s^2\ 3p^6\ 3d^6\ 4s^2$. According to *Hund's rules* a free Fe^{2+} ion has the following $3d^6$ ($n = 3$, $l = 2$) electron spin distribution:

m_l	-2	-1	0	1	2
m_s	1/2	1/2	1/2	1/2	±1/2
Spin	↑	↑	↑	↑	↑↓

This gives $L = \sum m_l = 2$ and $S = \sum m_s = 2$ and $J = L + S = 4$, resulting in the spin moment of 4 μ_B (spin-only, assuming that the orbital momentum is quenched).

The alignment of neighboring spins is determined by *exchange interaction energy* E_{ij}^{exch}. The interatomic exchange energy according to Dirac and Heisenberg is given by:

$$E_{ij}^{exch} = -2\mathcal{J}_{ij} S_i \cdot S_j \tag{2.5}$$

where $\mathcal{J}_{ij}$ is the exchange integral between atoms i and j and the S_i, S_j are the spin angular momenta. $\mathcal{J}_{ij} > 0$ results in an energy minimum for parallel spin alignment (ferromagnetism) and $\mathcal{J}_{ij} < 0$ for an antiparallel (antiferromagnetism) respectively.

In iron metal the outer shell electrons are not localized, but able to propagate throughout the material, i.e., *itinerant*, and form energy bands (*Stoner model*). The exchange field (or the internal *molecular field* according to Weiss [67]) causes splitting in the spin ↑ and spin ↓ d subbands making the transfer of the electrons from the spin ↓ subband to the spin ↑ subband energetically feasible as illustrated schematically in Figure 2.6a.

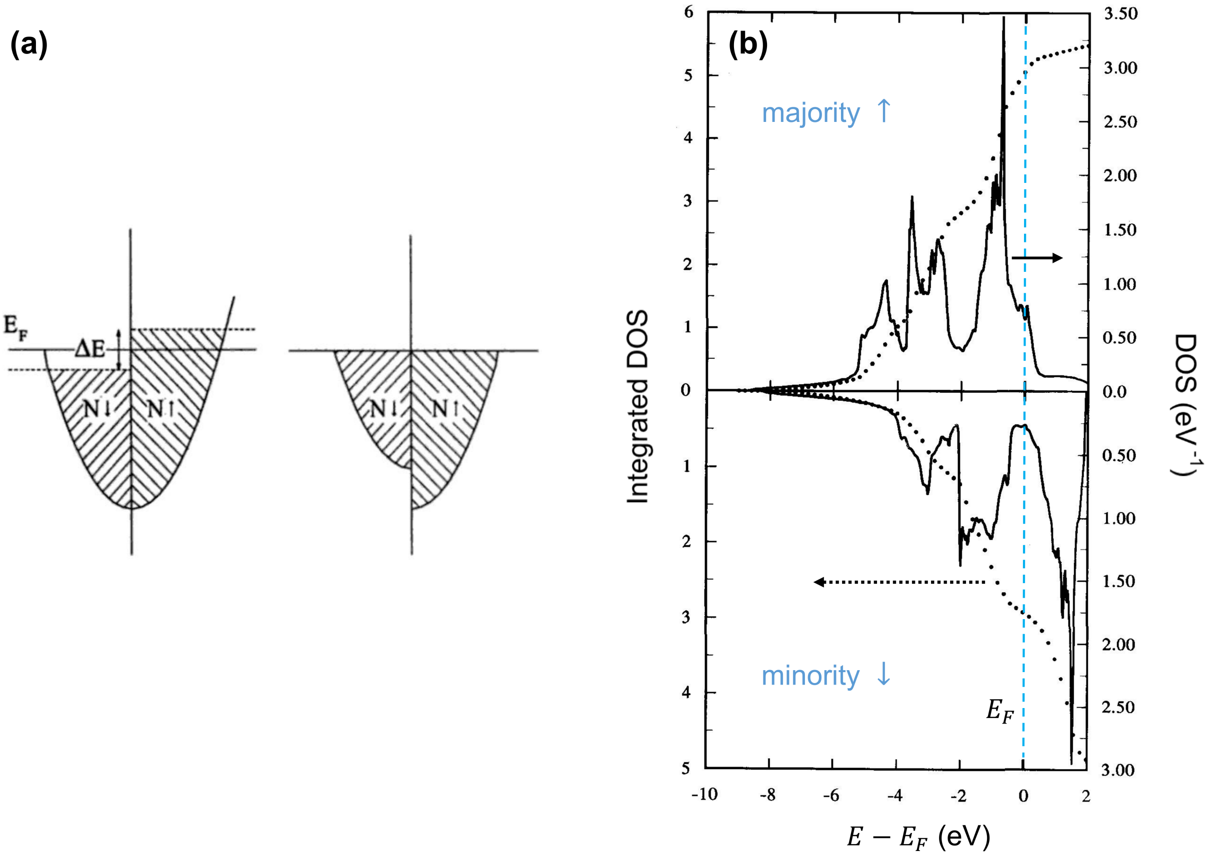

Figure 2.6: (a) Illustration of exchange splitting of the spin ↑ and spin ↓ d bands resulting in a net magnetic moment due to the transfer of electrons at the Fermi level. (b) Density of states according to spin polarized band calculations for α-Fe, showing the occurance of the net magnetic moment (adapted from [44] and [68]).

A quantitative description of this scenario for the case α-Fe is shown in Figure 2.6b. The exchange splitting δE is ≈ 2 eV and the resultant magnetic moment is given by the difference in the integrated density of states (the dotted line in Figure 2.6b). The number of electrons in spin ↑ at the E_F is 5.1 (majority band) and 2.9 for the spin down (minority band) respectively, resulting in N↑ - N↓ = 2.2, which is in very good agreement with the experimentally observed 2.226 μ_B/Fe atom (extrapolated to 0 K) [69].

A remarkable feature in the density of states (DOS) in Figure 2.6b is that the Fermi energy E_F cuts the majority band through the shoulder leaving roughly 0.2-0.3 states unoccupied. This, at first glance marginal, effect has a significant influence on the development of the magnetic moment in α-Fe. It shows that in case of a completely filled majority band, an enhancement of the magnetic moment up to 2.4-2.5 μ_B/Fe is to be expected. This indeed can be realized by, for example, alloying elements (such as Co) or tuning the inter-atomic separation. Both concepts are manifested by the famous Bethe-Slater [70]

(Figure 2.7a) and Slater-Pauling [71, 72] (Figure 2.7b) curves. The former one plays a critical role in understanding the magnetization in α'-Fe_8N_x.

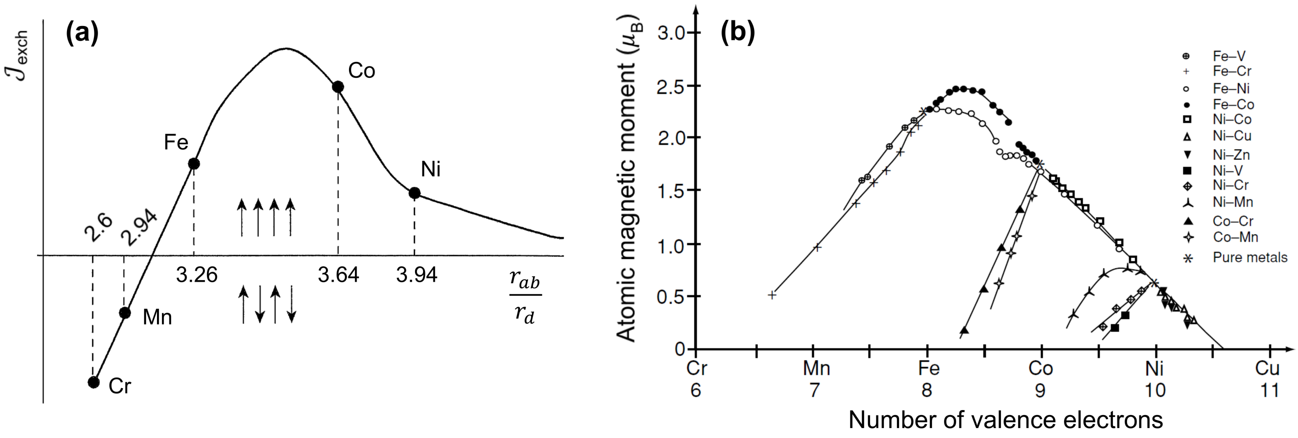

Figure 2.7: Bethe-Slater (a) and Slater-Pauling (b) curves showing the dependence of the atomic magnetic moment on the inter-atomic separation and alloying elements with different number of valence electrons (from [73] and [5]). r_d stands for the radius of the d-orbital, r_{ab} the distance between the atoms and $\mathcal{J}_{exch}$ is the exchange integral.

The *magnetovolume effect* for pure expanded α-Fe has been calculated in a number of works [74, 75, 53] and the results from Moruzzi et al. [74, 44] are presented in Figure 2.8. The results show that in agreement with the Bethe-Slater curve, at low inter-atomic separation (small atomic volume) the ground state of bcc Fe is nonmagnetic. The equilibrium atomic volume of $11.8\,\text{Å}^3$ (the calculated value of $11.15\,\text{Å}^3$ is slightly smaller than the one observed experimentally) results in the magnetic moment of about 2.2 μ_B/Fe atom followed by a continuous increase in the magnetic moment with further lattice expansion. At very large volumes, the free atom $3d^64s^2$ value of 4 μ_B is asymptotically reached. It is also evident from the Figure 2.8 that there is a steep increase in the total energy relative to the ground state when departing from the equilibrium volume, showing that equilibrium state is very stable and realizing significant compressive/tensile strain in order to tune the magnetic properties of bcc Fe is energetically costly.

However, one way to realize a reasonable unit cell expansion is by interstitial N atoms as described in the previous section. Alloying of 0-11 at.% nitrogen in bcc Fe, thus forming the α'-Fe_8N_x in the full range of $0 \leq x \leq 1$ would lead to atomic volume increase up to roughly $12.8\,\text{Å}^3$ (calculated using relation 2.4) as illustrated by the shaded area in Figure 2.8. This would consequently lead to enhanced magnetic moment, yet with the actual gain in the volume magnetization remaining less pronounced due to the concurrent unit cell volume increase.

The predicted enhancement of the magnetic moment in bcc Fe with alloying N has indeed been observed experimentally. For example, Mitsuoka et al. [76] showed that the magnetic moment in Fe-N and Fe-C martensites increases from 2.2 μ_B to 2.6 μ_B with the interstitial atom concentration as shown in Figure 2.9. These results are in reasonable agreement with the estimation from the band structure calcu-

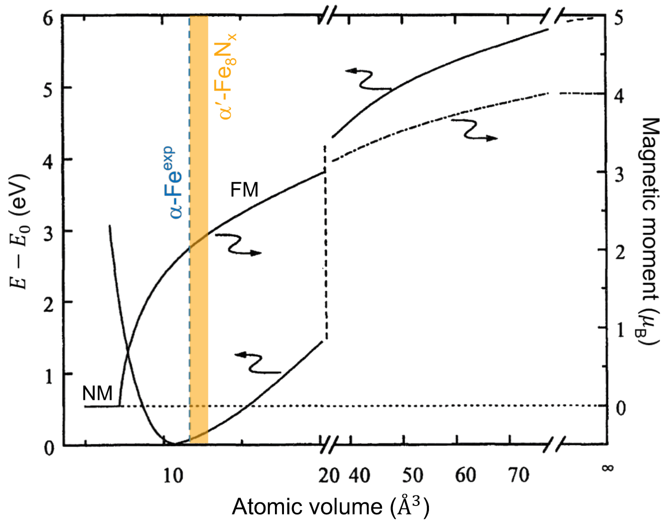

Figure 2.8: The calculated magnetic moment and total energy for α-Fe as a functon of the atomic volume (adapted from [74, 44]). The dashed line stands for the experimental atomic bcc Fe volume and the shaded area corresponds to the α'-Fe$_8$N$_x$ region. A continuous increase in magnetic moment with the atomic volume is predicted.

lations. Even higher magnetic moments could be realized in iron nano-clusters with a variable number of Fe atoms (between 25 and 700). A maximum value of 3 μ_B per Fe has been reported [77].

Two points are not obvious from the above and ought to be investigated further:

- First, the band structure calculation results considered so far are for isotropic unit cell expansion (not altering the crystal symmetry), whereas in the case of α'-Fe$_8$N$_x$ the actual expansion is tetragonal. Authors in [76] mention that the increased magnetic moment is actually caused by a superposition of both volume expansion and tetragonality effects.

- Second, whether the N atoms simply serve to stabilize the strain in the bct Fe or do they also contribute to the enhanced magnetic moment.

Both of the questions will be addressed later in this thesis. The magnetic moment increases linearly (a slope of 1 eV/μ_B) with the exchange splitting [78]. In the case for α'-Fe$_8$N$_x$ δE is assumed not to be influenced by the presence of nitrogen.

The magnetic anisotropy

The exchange interactions described in the previous section represented by a scalar product (Equation 2.5) are isotropic and therefore as long as the neighboring magnetic moments are aligned according to minimum energy, no preferential direction of magnetization is imposed to the system. In reality however, in a ferromagnetic material the magnetization prefers (the internal energy has a minimum as illustrated in Figure 2.11) to align along certain crystallographic directions. This effect is called *magnetocrystalline anisotropy* and is an intrinsic property of the material (in contrast to the *shape anisotropy*

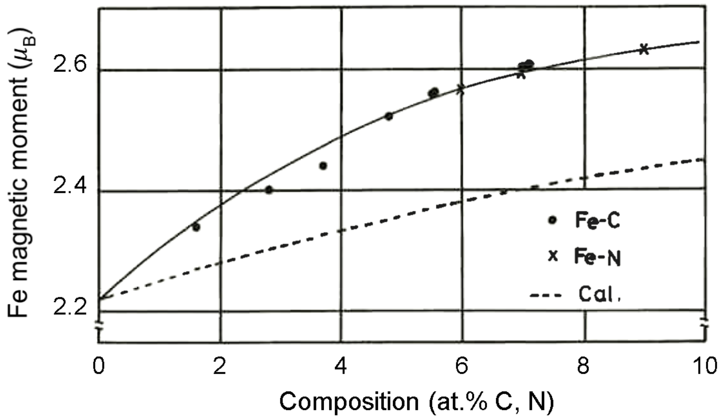

Figure 2.9: Experimentally observed increase in magnetic moment of Fe atoms in Fe-N and Fe-C martensites [76] (solid line is guide-to-the-eye).

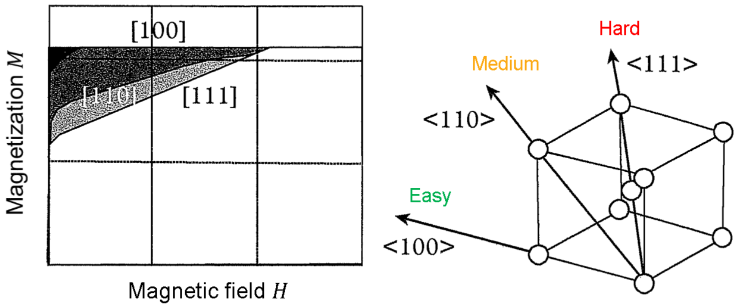

Figure 2.10: Magnetization of bcc Fe along different crystallographic directions (from [73]).

which is extrinsic and governed by the shape of the sample). Directions along which the magnetization saturates at the lowest applied field are called *easy directions* or *easy axis*. Conversely, the directions where the maximum field has to be applied are called *hard directions* as shown in Figure 2.10 for a bcc Fe crystal. α-Fe is a soft magnetic material with a low anisotropy constant of about 50 kJ m^{-3} [79, 80]. The easy axis are along <100> crystallographic directions as illustrated in Figure 2.10 with the corresponding anisotropy energy surface shown in Figure 2.11a.

The magnetocrystalline anisotropy in α'-Fe$_8$N$_x$ has not been fully understood yet. As a tetragonal crystal it should possess a uniaxial anisotropy according to Figure 2.11b, where the *anisotropy-energy* can be described by the expression

$$E_a = K_1 V \sin^2\theta \tag{2.6}$$

and the corresponding *anisotropy field* is

$$H_\mathrm{a} = \frac{2K_1}{\mu_0 M_\mathrm{s}}. \tag{2.7}$$

Here K_1 is the first uniaxial *anisotropy constant*, V is the magnet volume, θ the angle between the magnetization and the easy axis and M_s is the saturation magnetization. It is generally expected that lowering of the symmetry leads to an enhancement in magnetocrystalline anisotropy energy (MAE) (a

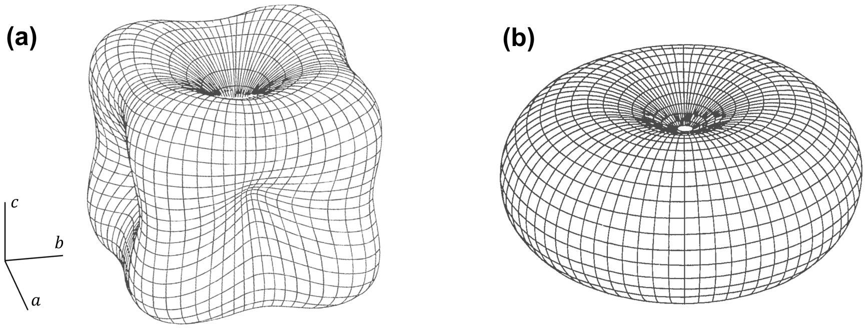

Figure 2.11: Anisotropy energy surfaces for cubic (a) and uniaxial (b) crystals (from [81]).

comprehensive treatment of this problem is given by Bruno [82]). For example, a significant MAE has been predicted for tetragonal (with c/a of about 1.20-1.25) Fe-Co alloys [83]. Therefore one could also expect MAE to increase strongly if the cubic symmetry of bcc Fe is broken, i.e., the case with introducing interstitial nitrogen. However, calculations for tetragonally (bct) distorted Fe done by Burkert et al. [84] reveal much more complicated picture as shown in Figure 2.12. At first, MAE increases with small distortions, but an easy axis reorientation from [001] to [100] occurs at a ratio $c/a \approx 1.07$. The c/a ratio for the α'-Fe_8N_x is indicated by the shaded area and it is obvious that based on these results α'-Fe_8N_x should exhibit a uniaxial anisotropy with the easy axis along the [001] direction (tetragonally distorted c-axis) for small c/a values (small N concentrations respectively) and a strongly negative anisotropy energy corresponding to the easy direction of the magnetization within the basal plane at the end of these series. Yet this is contrary to the experimental data. An increase in the coercivity in Fe_8N precipitates in bulk samples has been observed already decades ago [85] and more recent report by Ji et al. [86] also shows a continuous increase in the in-plane saturation field with the c lattice constant in α' thin films, thus, clearly demonstrating the development of perpendicular anisotropy component in the Fe-N layer due to the increasing magnetocrystalline anisotropy. The uniaxial anisotropy constant has shown to be roughly

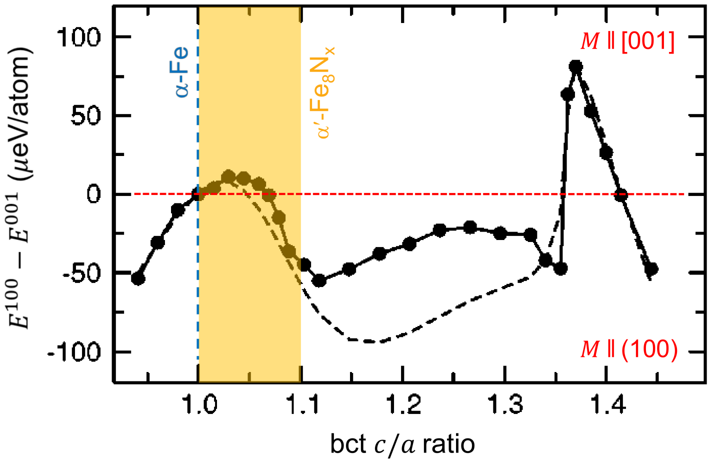

Figure 2.12: Calculated magnetocrystalline anisotropy energy for tetragonally (bct) strained Fe (adapted from [84]).

$0.5\,\mathrm{MJ\,m^{-3}}$ which is one order of magnitude larger that of the initial bcc Fe. This discrepancy suggests that, when it comes to the MAE, the nitrogen atoms play far more important role than just stabilizing the tetragonal distortions as it could be treated for the case of the enhanced magnetic moment in α-Fe. The interstitial N atoms might be crucial for stabilizing the uniaxial MAE in α'-Fe_8N_x. This question will be addressed in Chapter 5.

The Curie temperature

Despite the amount of studies, no reports on the exact Curie temperature of α'-Fe_8N_x can be found in the literature. An approximation of the Equation 2.5 considering a single sublattice and only the nearest neighbor interactions leads to a relation [73]:

$$\mathcal{J}_{exch} = \frac{3k_\mathrm{B}T}{2ZS(S+1)}. \tag{2.8}$$

k_B is the Boltzmann constant, T_C is Curie temperature, Z is the number of nearest neighbors and S is the electron spin momentum. This would point towards raising T_C with $\mathcal{J}_{exch}$ for α'-Fe_8N_x, in the same manner as the magnetic moment (the Bethe-Slater curve shown in Figure 2.7 can also analogically be plotted with T_C on the ordinate). However, this treatment is possibly overly simplified. For example, if the coordination number also changes due to the change of the crystal symmetry (lowering of the symmetry in the case of α'-Fe_8N_x), instead of $Z = 8$ as it is for α-Fe, the coordination number would be reduced and consequently the Equation 2.8 would lead to a lower T_C value for the same $\mathcal{J}_{exch}$. For example, a Curie temperature values significantly lower than for bulk Fe (1043 K) have been observed experimentally in iron clusters [77] and ultrathin films [87].

2.3 The secondary Fe-N martensite: α''-$Fe_{16}N_2$

2.3.1 Structural properties

An intermediate phase before precipitation of γ'-Fe_4N during aging of solid solution of nitrogen in α-Fe was observed by Dijkstra in 1949 [37]. A new Fe-N phase occurred before the decomposition into γ'-Fe_4N and was thought to correspond to a transition phase from ferrite to Fe_4N.

The identification as a distinct ordered secondary martensite α''-$Fe_{16}N_2$ phase with description of the space group, lattice parameters and atomic positions was first done in 1951 by Jack [47]. The samples were synthesized by quenching from austenite and subsequent low temperature (393 K) heat treatment of the martensite powders with different N concentrations. The α''-$Fe_{16}N_2$ phase has a body-centered crystal structure with space group $I4/mmm$ (139). It is a superstructure of the original saturated Fe-N martensite with Fe_8N_1 chemical composition. The α''-$Fe_{16}N_2$ unit cell consists of 2x2x2 unit cells of α', as such having twice the lattice parameters, $a = b = 5.72$ Å, $c = 6.29$ Å and the $c/a = 1.1$. The nitrogen atoms occupy octahedral interstitial sites in a completely ordered manner. The exact crystallographic lattice sites for Fe and N are summarized in Table 2.3. The unit cell of the α''-$Fe_{16}N_2$ phase is illustrated in Figure 2.13.

Table 2.3: Atomic sites in α''-$Fe_{16}N_2$ according to Jack [47].

Atom	Site	x	y	z
Fe1	$4e$	0	0	0.31
Fe2	$4d$	0	0.5	0.25
Fe3	$8h$	0.25	0.25	0
N	$2a$	0	0	0

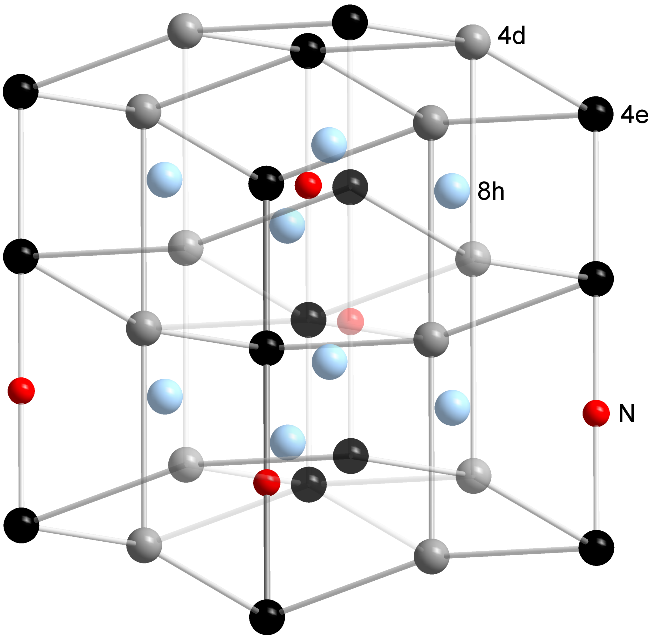

Figure 2.13: Unit cell of α''-$Fe_{16}N_2$ consisting of 2x2x2 unit cells of the α' martensite. Three different iron sites are distinguished and the nitrogen atoms occupy the octahedral interstitial sites ($2a$) in an ordered manner.

2.3.2 Magnetic properties

The magnetic moment

As described in the previous section, the α''-$Fe_{16}N_2$ phase can be treated as a supercell of the saturated the α'-Fe_8N_1 martensite. Therefore, unless the ordering of the N atoms plays a critical role, intuitively the magnetic properties comparable to those of the α' martensite could be expected.

In the original work by Jack magnetic properties of α''-$Fe_{16}N_2$ were not investigated. About two decades later, in 1972, Kim and Takahashi [18] reported a, "new magnetic material having ultrahigh magnetic moment", where the magnetic moment reached $3.0\,\mu_B$ per Fe atom and was attributed to formation of α''-$Fe_{16}N_2$ phase. Numerous studies followed, trying to reproduce the results. Extraordinary high magnetic moment (3.1 μ_B to 3.5 μ_B per Fe atom at room temperature) was reported by Komuro and Sugita [88, 89, 90, 91] in thin films grown by molecular beam epitaxy onto InGaAs and GaAs substrates. Ever since there have been many discussions and controversy concerning the magnetic properties of α''-$Fe_{16}N_2$. Other works have shown that the average iron moment at 0 K does not exceed 2.6 μ_B from both experimental and theoretical points of view [76, 92, 93, 94, 95, 96, 97, 94, 31, 98, 99, 100, 101], which results in a moderate increase in M_s due to the accompanied unit cell volume expansion.

Due to this controversy between different reports, phrases like, "the magnetism of $Fe_{16}N_2$ has been a mystery for 40 years" [102], "it is clear that α''-$Fe_{16}N_2$ is a low-magnetic phase when it is prepared in pure form and that the high-magnetic moments which were measured by Sugita et al. and other workers are probably due to other phases of the Fe-N system" [103], or, "α''-$Fe_{16}N_2$ is one of the most fantastic and mysterious materials in the field of magnetism for over 25 yrs because it is not clear whether 'its giant magnetic moment is true or not' since its discovery in 1972" [27], and "Magic moments in magnetism" by J. M. D. Coey [28], emerge in literature.

A summary of the magnetic properties obtained via different synthesis routes is provided in Table 2.4. As evident from the data, the saturation magnetization M_s values vary in a broad range.

Table 2.4: Overview of the synthesis and magnetic properties of α''-Fe$_{16}$N$_2$ in form of thin films, bulk and nanoparticles.

Form	Method	$\mu_0 M_S$ (T)	$\mu_0 H_c$ (T)	K_u (MJm^{-3})	Phases present	Buffer	Reference
Thin film	Evaporation	2.83@0 K	-	-	$\alpha+\alpha''$	-	[18]
Thin film	MBE	2.8-3.0@RT	0.001-0.005	0.048	α''	Fe	[89]
Thin film	MBE	2.9@RT	-	-	α''	-	[90]
Thin film	MBE	2.8@RT	-	0.780	α''	-	[104]
Thin film	MBE	3.23@0 K	-	-	α''	-	[91]
Thin film	Sputtering	2.68@RT	-	-	$\alpha'+\alpha''$	Fe	[102]
Thin film	Sputtering	0.31@RT	-	-	α''	-	[103]
Thin film	Sputtering	2.24@RT	-	-	$\alpha'+\alpha''$	Fe	[96]
Thin film	Sputtering	2.17@RT	-	-	$\alpha'+\alpha''$	Fe	[93]
Thin film	Sputtering	2.38@RT	-	-	$\alpha'+\alpha''$	Ag/Fe	[105]
Thin film	N ion implantation	2.30@RT	-	-	$\alpha+\alpha''$	Si/Fe	[106]
Bulk (foil)	Quenching from γ	2.1-2.5@RT	-	-	$\alpha+\gamma+\gamma'+\alpha''$	-	[94]
Bulk (foil)	Quenching from γ	2.5@RT	-	-	$\gamma+\alpha'$	-	[76]
Bulk (powder)	Quenching from γ	2.66@RT	-	0.78	$\alpha+\gamma+\alpha''$	-	[107]
Bulk (powder)	Ball milling	1.96@RT	0.0854	-	$Fe_2O_3+\alpha+\alpha''$	-	[22]
Foil	N ion implantation	2.9@RT	0.191	-	$\alpha+\gamma'+\alpha''$	-	[108]
Bulk	Strained-wire	2.56@RT	0.122	-	$\alpha+\gamma'+\alpha'+\alpha''$	-	[109]
Nanoparticles	Fe-O$\rightarrow H_2 \rightarrow NH_3$	2.11@RT	-	0.96	α''	-	[20]
Nanoparticles	Fe-O$\rightarrow H_2 \rightarrow NH_3$	1.54@RT	0.1	-	α''	-	[110]
Nanoparticles	Fe-O$\rightarrow H_2 \rightarrow NH_3$	1.83@RT	0.335	0.44	Fe-O, α''	-	[111]
Nanoparticles	Fe-C$\rightarrow H_2 \rightarrow NH_3$	1.54-2.17@RT	0.093	-	$\alpha+\gamma'+\alpha''+\epsilon$+Fe-O	-	[112]

Many theoretical studies have been conducted in order to clarify the experimentally reported contradictory magnetic moment values. A vast majority of those works predict an enhancement in the magnetic moment with respect to the initial α-Fe, up to roughly 2.4 μ_B–2.6 μ_B per Fe atom, in agreement with what would be expected for the corresponding magnetovolume effect. Some of the results are summarized in Table 2.5. All the three atomic sites show magnetic moment values correlated to the respective bond length to the nearest neighbor Fe atom, which is consistent with the band structure model discussed in the Section 2.2.2 for α' martensite. The highest magnetic moment ($\approx 2.85\,\mu_B$) for the 4d site has been attributed to the d-band localization [113] due to the large Fe-Fe distance of 2.56 Å. The Fe-Fe distance for the 8h site is still slightly larger than that of the α-Fe leading to an enhancement in magnetic moment, whereas due to the hybridization with N as well as the 5 % shorter Fe-Fe distance than in α-Fe, the magnetic moment is reduced even below 2.22 μ_B for the 4e site.

Table 2.5: Theoretically calculated magnetic moment values for different crystallographic sites in α''-$Fe_{16}N_2$.

Magnetic moment per Fe atom (μ_B)				
Fe (4e)	Fe (8h)	Fe (4d)	Average	Reference
2.27	2.25	2.83	2.55	[98]
1.96	2.41	2.91	2.55	[114]
2.13	2.5	2.85	2.5	[113]
2.21	2.39	2.81	2.45	[94]
2.04	2.33	2.82	2.38	[115]
2.19	2.38	2.84	2.44	[100]

It has been proposed that the order/disorder of the interstitial N atoms is notably influencing the magnetization of α''-$Fe_{16}N_2$. It was reported by Sugita [89] that ordering of N atoms (by subsequent annealing) increased M_s from 2.5 T to 3.0 T. Also later [90] N atom ordering was induced by post annealing at 473 K and as a result an increase in M_s from 2.4 T for α'-Fe_8N to 2.9 T for α''-$Fe_{16}N_2$ was observed. More recent study by Ji et al. [102] affirms that ordering of nitrogen atoms plays a significant role in the development of the magnetic moment. The ordering parameter D is defined as follows:

$$D = \frac{I^{obs}(002)/I^{obs}(004)}{I^{cal}(002)/I^{cal}(004)}, \tag{2.9}$$

where I^{obs} refer to the integral intensities of the measured XRD peaks and I^{cal} represent the theoretical intensities for α''-$Fe_{16}N_2$ respectively. Figure 2.14a shows that in the Fe-N films deposited on GaAs substrates with using Fe buffer layer the M_s increases gradually with the N site ordering parameter D from about 2.05 T to 2.68 T for $D > 0.3$. This resulted in the equivalent magnetic moment per Fe atom of 2.93 μ_B.

It has to be noted that the observed magnetic moment values in these works by far exceed the theoretically predicted ones as well as the $\approx 2.5\,\mu_B$ per Fe atom at room temperature for $Fe_{70}Co_{30}$. The physical mechanism of this phenomena as well as credibility of the data is still neither entirely clear nor accepted by the scientific community.

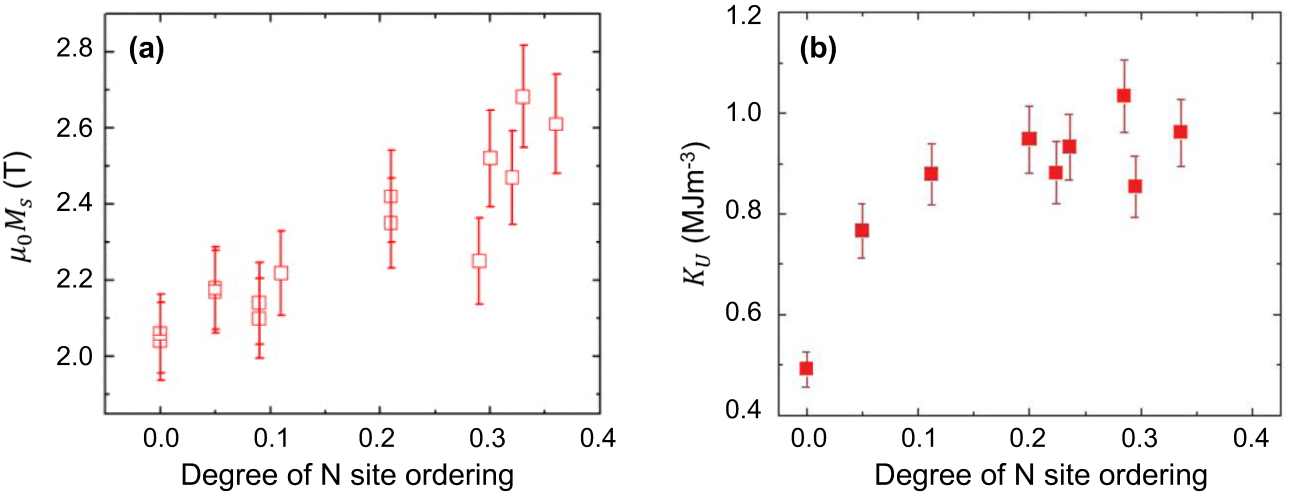

Figure 2.14: M_s (a) and K_u (b) as a function of N site ordering D for Fe-N (50 nm)/Fe (24 nm)/GaAs thin film samples (adapted from [102] and [86])

The magnetic anisotropy

Magnetic anisotropy for α''-$Fe_{16}N_2$ has been measured in different works [89, 19, 111, 86, 20, 107] and also here a unified picture has not yet evolved. The MAE values vary in a range from 0.44 MJ m^{-3} [111] to 2 MJ m^{-3} [19]. Takahashi et al. [19] states that the MAE for α'' is larger than for α' martensite. This seems to be in agreement with the reported increase in MAE with the degree of N site ordering D [86], which is displayed in Figure 2.14b.

As discussed in the Section 2.2.2, the N atoms might play a crucial role in stabilizing uniaxial anisotropy in α'. This idea is supported by the results from Ke et al. on the ordered α'' phase [101]. The atomic magnetic anisotropy contributions for the three different Fe sites have been calculated. Figure 2.15a shows that the largest (and positive) contribution to the MAE comes from the Fe 4e site with the energy minimum corresponding to the [001] crystallographic direction which is the easy axis of the tetragonal structure. Furthermore, the 4e site is the one with Fe atoms right above and below the N, thus equivalent to the distorted octahedra model in α'. The authors also report a strong, roughly linear increase in the anisotropy with the tetragonality, i.e., c/a ratio (Figure 2.15b), which is thought to mainly originate from distortion of the Fe atoms surrounding N atom and the respective hybridization. Experimentally $c/a > 1.1$ is not realized in α'/α'' system and therefore this result is hard to be verified.

The Curie temperature

The Curie temperature of α''-$Fe_{16}N_2$ can not be measured directly, due to the decomposition of the phase [116, 21]. Therefore the T_C values have to be estimated from fitting of the $M(T)$ data in a temperature range where α''-$Fe_{16}N_2$ is still stable and performing an extrapolation. By this method (fitting the $M(T)$ data with the Langevin function) Sugita et al. have estimated the Curie temperature to be $T_C \approx$

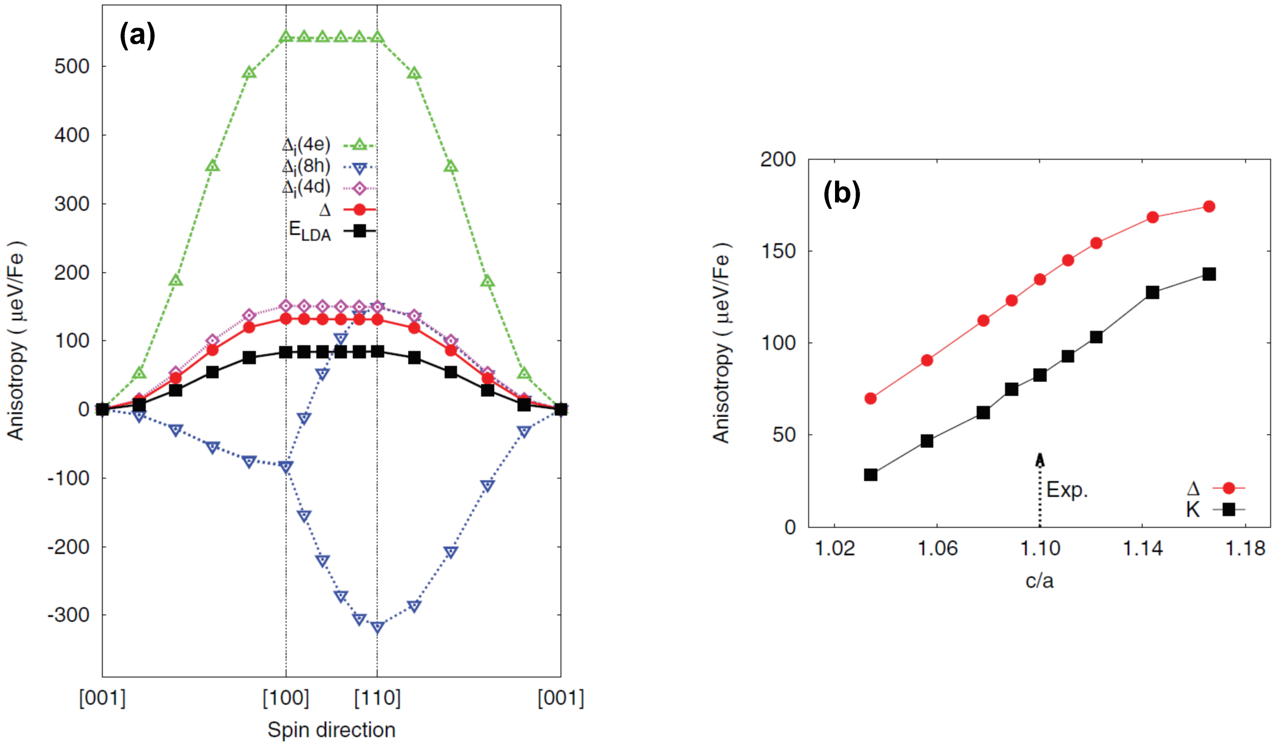

Figure 2.15: Atomic magnetic anisotropy contributions Δ_i for the three different Fe sites in α''-$Fe_{16}N_2$ (a) and their average value Δ as a function of the c/a ratio (b). E_{LDA} represents the total energy with respect to the ground state and K the MAE (from [101]).

810 K [89]. Even though the precise T_C value might be inaccurate, the data clearly indicates significantly steeper negative slope for α''-$Fe_{16}N_2$ than for pure Fe [89, 91] and therefore a lower Curie temperature (Figure 2.16). Ke et al. [101] mention that contrary to the experiments, their calculations predict T_C for α''-$Fe_{16}N_2$ to be higher than that of α-Fe. The authors state that the discrepancy with experimental results might be caused by the experimental obstacles and in high quality samples of pure α''-$Fe_{16}N_2$ a much larger, probably larger than in pure bcc Fe, T_C is to be expected. Sakuma [117], on the other hand, reports that the Curie temperature should be comparable with iron or lower which agrees with the experimental findings. Takahashi et al. [118] has shown that the slope for the decrease of the magnetization with temperature is steeper for α'' than for α' martensite (Figure 2.16) which indicates lower Curie temperature and thus would imply that the N atom ordering influences not only the magnetic moment and anisotropy as discussed above, but also the critical behavior.

In this work, in order to estimate the Curie temperature T_C for Fe and Fe-N samples, the magnetization versus temperature data has been fitted (in a temperature range were the respective phases are stable) with Equation 2.10 proposed by Kuz'min [119] instead of the Langevin function. The Equation 2.10 is constructed to obey Bloch's 3/2 power law at low temperatures and a power of 1/3 of the Heisenberg model in the critical region. This is therefore expected to deliver more accurate results. Here $\tau = T/T_C$, $M_s(0)$ is the saturation magnetization at 0 K and s, p are fitting parameters.

$$M_s(T) = M_s(0)\left[1 - s\tau^{3/2} - (1-s)\tau^p\right]^{1/3}. \tag{2.10}$$

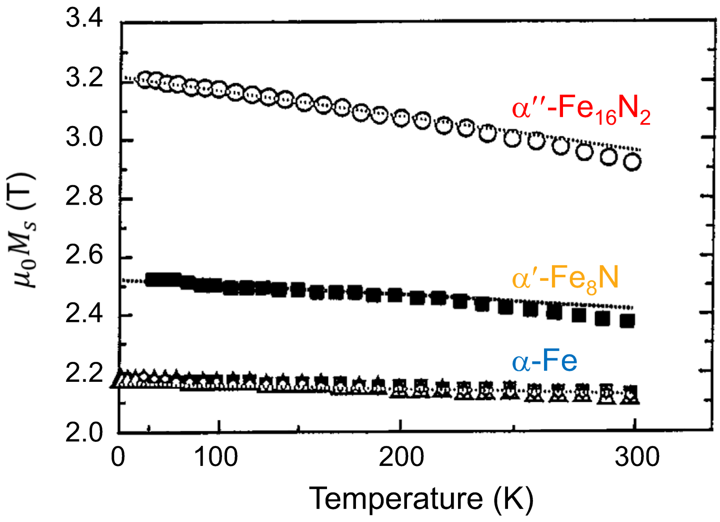

Figure 2.16: Temperature dependence of the saturation magnetization for α-Fe, α'-Fe_8N and α''-$Fe_{16}N_2$ thin films. A much more negative slope for α'' suggests a lower Curie temperature. Adapted from [89, 118]).

3 Experimental

In this chapter the most relevant experimental techniques used in this thesis are described. A number of additional methods, such as magnetic force microscopy (MFM) in thin film studies or hot-pressing, ball-milling for bulk nanocomposite magnets, are briefly introduced within the corresponding chapters.

The first section deals with sample preparation in a form of thin films and nanoparticles. The second part summarizes the corresponding material characterization principles.

3.1 Sample preparation

3.1.1 Thin film deposition

The first part of this thesis is dedicated to studies of α-Fe, γ'-Fe_4N and α'-Fe_8N_x thin films.

The thin film samples were deposited by RF (13.56 MHz) magnetron sputtering onto single-crystal MgO (001) substrates with a chamber base pressure of 8.0×10^{-8} mbar. The schematic of the deposition chamber is shown in Figure 3.1. The substrates were loaded via a loadlock followed by pumping the chamber until the desired pressure has been reached. Prior to deposition, all the substrates were heated to 923 K for 10 min under continuous pumping for surface cleaning and then cooled down to the desired deposition temperature. Due to the distance between the heater bulb and the substrate with the substrate-holder in between, a strong temperature gradient is to be expected. Therefore, once reached, the temperature was allowed to thermalize for 10 min. In order to improve reproducibility, a pre-sputtering step for 10 min with the shutter closed, allowing the process to stabilize was performed before starting the deposition.

In order to find the optimum deposition conditions for the phase formation of Fe and Fe-N phases, the deposition power, argon and nitrogen flow, deposition pressure, substrate temperature, and target-substrate distance were varied.

In case of the γ'-Fe_4N studies, the optimum parameters for pure Fe (99.90% purity Fe target) films were: 40 W RF power, 4.0 sccm argon (99.999% purity) flow, 0.025 mbar deposition pressure, 673 K substrate temperature, 12 cm target-substrate distance and 10 min deposition time. The optimum parameters for γ'-Fe_4N films were found to be identical, except that the deposition gas mixture consisted of 3.9 sccm Ar and 0.1 sccm N_2 (99.9999% purity). The resulting deposition rate was about 0.45 Å/s.

In case of the α'-Fe_8N_x studies, the optimum parameters for pure Fe (99.90% purity Fe target) films were: 100 W RF power, 1.0 sccm argon (99.999% purity) flow, 0.003 mbar deposition pressure, 373 K substrate temperature, 15 cm target-substrate distance and 10 min deposition time. α'-Fe_8N films have been prepared using the same conditions, except that the plasma gas flow consisted of 1.0 sccm argon and additional nitrogen (99.9999% purity). The deposition rate was around 1.1 Å/s.

All films were in situ capped with a Ta (99.95% purity) layer directly after the deposition in order to prevent oxidation when exposed to air.

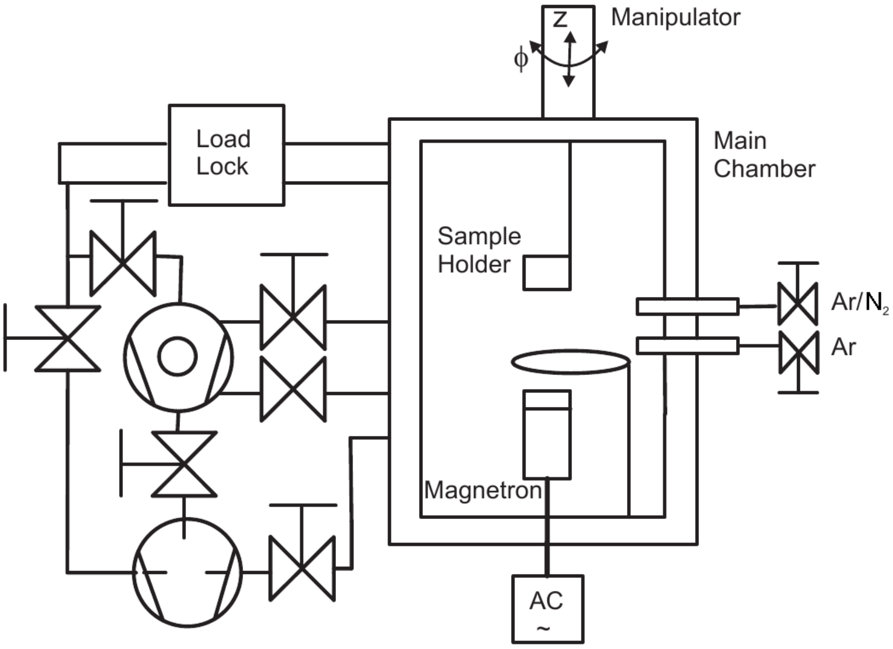

Figure 3.1: Schematic of the used magnetron sputtering chamber setup. Figure adapted from [120].

3.1.2 Nanoparticle synthesis

The second part of the thesis deals with synthesis and characterization of α''-$Fe_{16}N_2$ nanoparticles. Various works have been done on production of α''-$Fe_{16}N_2$ in a form of nanoparticles. Bao and Metzger [121] used a route where γ-Fe_2O_3 was reduced to α-Fe under H_2, nitrogenated in NH_3-H_2 flow at 923 K–973 K, quenched in liquid nitrogen and subsequently tempered at 393 K–473 K in order to transform α' martensite into α''-$Fe_{16}N_2$. The estimated mole fraction of α''-$Fe_{16}N_2$ was about 0.30-0.40. A different approach by using direct synthesis of α'' from α-Fe fine particles by low temperature nitrogenation instead of austenite-martensite transformation has proven to be more effective in yielding higher fraction of α'' and high-purity samples have been reported [122, 123, 124, 125, 20, 116, 110].

One possibility for hindering the disadvantageous particle agglomeration and sintering could be coating with a nonmagnetic shell. Such studies have been performed previously by different authors [126, 127, 128, 129]. However, this approach leads to a more complicated synthesis route, the presence of the additional nonmagnetic material reduces M_s and the shell thickness might be comparable to the exchange length and therefore unfavorable for exchange-coupled nanocomposite applications, as an example.

Accordingly, in this work the goal was to optimize the α''-$Fe_{16}N_2$ synthesis route in order to reduce the particle growth by another means. There are three parameters influencing the final particle size and the agglomeration: the state of the initial iron oxide nanoparticles, the hydrogen reduction step and the nitrogenation. The nitrogenation is normally performed at relatively low temperatures (393 K–473 K), thus the main contributor to particle growth during synthesis of α''-$Fe_{16}N_2$ is the hydrogen reduction step:

$$Fe_2O_3 + 3H_2 \xrightarrow{Heat} 2Fe + 3H_2O. \tag{3.1}$$

Only reactions where the change in Gibbs free energy $\Delta G < 0$ will take place spontaneously. In the case of Reaction 3.1, the thermodynamic data values (at 298 K) are given in Table 3.1 [130, 131].

Table 3.1: Thermodynamic data for the Reaction 3.1 (at 298 K).

Phase	$\Delta_f G^0$ (kJ/mol)	$\Delta_f H^0$ (kJ/mol)
Fe_2O_3	-725	-806
H_2	0	0
Fe	0	0
H_2O	-229	-242

Consequently, the Reaction 3.1 has $\Delta_r G^0 = 38\,\mathrm{kJ\,mol^{-1}}$, $\Delta_r H^0 = 80\,\mathrm{kJ\,mol^{-1}}$ and the reaction constant $K_r = p^3_{H_2O}/p^3_{H_2}$. This shows that the reaction is endergonic, endothermic and at ambient conditions would not occur spontaneously.

There are three possibilities for shifting the equilibrium to the right:

- Increasing the partial pressure of H_2
- Lowering the partial pressure of H_2O
- As the reaction is endothermic, by raising the reaction temperature. According to *van't Hoff's equation*:

  $$\frac{\mathrm{d}\ln K_r}{\mathrm{d}T} = -\frac{\Delta_f H^0}{RT^2}, \tag{3.2}$$

  which gives $\ln K_r = -\frac{\Delta_f H^0}{RT} + const$ after integration. This shows that increasing the temperature would rise the reaction constant.

Figure 3.2: Schematic of the two-step process route for synthesis of α''-$Fe_{16}N_2$ nanoparticles.

Solid-state sintering is a diffusion governed process and its intensity is exponentially related to the temperature. A straight-forward way then for decreasing the particle growth during the reduction of γ-Fe_2O_3 would be lowering the reaction temperature. Different studies conducted on iron oxide reduction with hydrogen have shown that at atmospheric pressures a temperature of at least 663 K is necessary for the complete reduction to α-Fe. E.g., reduction of iron oxides has been done previously by treating nano-sized γ-Fe_2O_3 at 663 K for 3 h [110], α-Fe_2O_3 at 563 K–753 K for 3 h–5 h [20], α-Fe_2O_3 at 773 K for 1 h [123], γ-Fe_2O_3 at 773 K for 8 h [124], γ-Fe_2O_3 at 773 K for 12 h [125], in flowing hydrogen. However, the reduction step at elevated temperatures, unless the particles are coated with some sintering preventing agent, inevitably leads to particle sintering and growth which then is disadvantageous for the subsequent nitrogenation step as well as for further applications.

In this work an attempt to minimize the detrimental particle coarsening during the reduction step by increasing hydrogen and reducing water vapor partial pressure in the reaction zone is presented. According to the reaction constant, it should result in shifting the chemical equilibria of the Reaction 7.4 to the right (towards products) and enabling complete reduction of iron oxides at much lower temperatures.

Phase-pure α''-$Fe_{16}N_2$ nanoparticles are synthesized via a two-step route. First, commercial γ-Fe_2O_3 nanoparticles (>98 % γ-Fe_2O_3 phase, Alfa Aesar) with an average particle size (APS) of 20 nm–40 nm, were used as a precursor and reduced to α-Fe in a hydrogen (99.999 % purity, Linde) atmosphere. In order to reduce the γ-Fe_2O_3 nanoparticles to pure α-Fe at possibly low temperatures, elevated hydrogen pressures had to be applied. For this purpose, a custom-made autoclave setup, pressure vessel (Series 4740, Parr Instrument Company) with a working volume of 75 cm^3 (shown in Figure 3.3) equipped with an external vertical tube heater assembly (Model 4921, Parr Instrument Company) was used. 0.050 g of iron oxide nanoparticles were filled into a steel crucible and mounted in the pressure vessel. After twice evacuating to $\approx 5.0 \times 10^{-2}$ mbar and purging with Ar (99.999 % purity, Air Liquide), the reactor was heated to the desired setpoint temperature under continuous pumping and pressurized with hydrogen. After the experiment, the reactor was evacuated and cooled down to room temperature under continuous pumping. Samples were always handled in an Ar filled glovebox ($p(O_2)$<0.1 ppm, MBraun) in order to avoid oxidation. Different reaction conditions (temperature, time, hydrogen pressure, presence of a water binding agent) were varied in order to optimize the process towards lower temperatures and thus reduced particle growth.

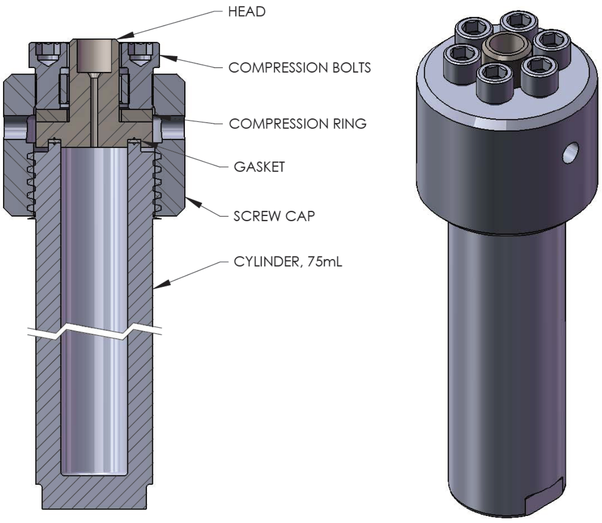

Figure 3.3: Pressure vessel used for high-pressure hydrogen experiments [132].

In the second step, the hydrogen-reduced α-Fe nanoparticles were subsequently nitrogenated in an ammonia (99.999 % purity, Linde) flow. For the nitrogenation experiments, a custom-made horizontal quartz-tube setup as illustrated schematically in Figure 3.4 was used. The samples were loaded in a glovebox under argon atmosphere and transferred to the furnace without contact to air. After assembly, all the gas connection lines were three times evacuated to 1.0×10^{-3} mbar and purged with argon prior to ammonia to ensure oxygen-free experiments. The reaction time and temperature were varied in order to tune the conditions for achieving the synthesis of phase-pure α''-$Fe_{16}N_2$ nanoparticles in the shortest possible time and at the lowest temperature. After the experiments the samples were cooled down to room temperature and under vacuum transferred into a glovebox.

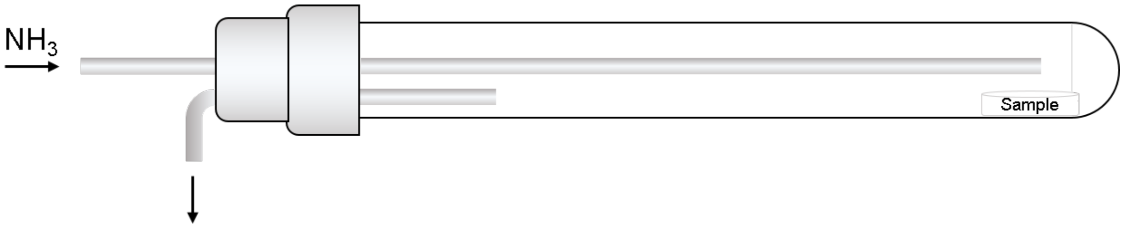

Figure 3.4: Setup used for nitrogenation in ammonia atmosphere.

3.2 Sample characterization

3.2.1 X-ray diffraction

X-ray diffraction (XRD) provides a quick and cost-effective way for phase identification and, even though it can be less straight-forward, also quantification. As such, it is a powerful experimental tool and gives a direct feedback for optimization of synthesis parameters etc. which, as will become evident in the later chapters, is crucial for studies presented in this work.

Powder XRD data were mostly collected by a powder diffractometer STOE, Stadi P, position sensitive detector using Mo K_{α_1}-radiation (Ge[111] monochromator, λ=0.70930 Å, quartz capillary), operating in transmission Debye-Scherrer geometry (illustrated in Figure 3.5a).

Thin film structural characterization ($\theta - 2\theta$ geometry), has been done by using a Rigaku SmartLab X-Ray diffractometer with Cu K_{α_1}-radiation (Ge[220] 2-bounce monochromator, λ=1.54059 Å) operating in reflection (mostly parallel beam) geometry.

Whenever other XRD measurement configurations are used (such as, texture analysis (χ-ϕ scan) or substrate-film orientation (ϕ-scan), it is explained accordingly within the main text.

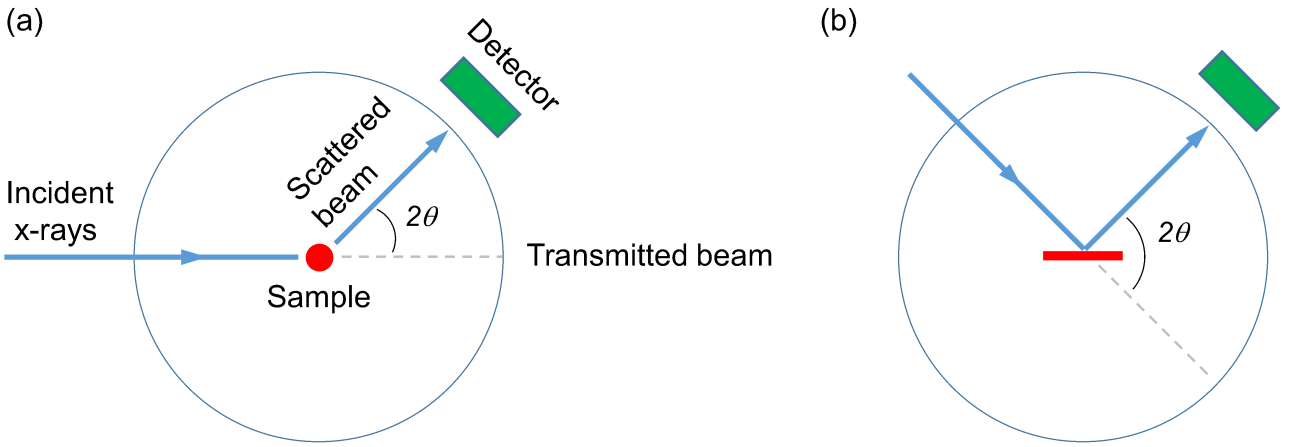

Figure 3.5: In this work most commonly used XRD geometries. (a) Transmission mode (top view). (b) Reflection mode (side view).

3.2.2 X-ray reflectivity

A critical point when it comes to measuring absolute values of magnetization in thin film samples is the film volume estimation, which, as the lateral dimensions of the substrate can be measured with high accuracy, relies on precise film thickness determination.

Cross-sectional TEM would be a method of choice, however, it is time consuming, expensive and destructive technique and therefore not really suitable for high-throughput characterization of many samples for gaining a quick feedback during the parameter optimization of the deposition process.

Another method, quartz crystal monitor (QCM), is not really optimal and might lead to errors for the materials investigated within this thesis. The interstitial light element N causes significant unit cell expansion with proportionally small increase in on the crystal deposited mass. The observed change in the oscillation frequency might not lead to an accurate correlation with the calibrated value. As a result, the film thickness will be underestimated, leading to an overestimated magnetization values.

An accurate, time and cost effective tool for film thickness determination is x-ray reflectivity (XRR). Moreover, XRR measurement also provides other parameters including layer densities, surface and interface roughness values and therefore is used for thin film analysis within this work.

In contrast to visible light, for the case of x-rays as incident electromagnetic waves, the refractive index n of a material is slightly less than 1 (for a detailed treatment of the problem the reader is referred to Chapter 4 of Ref. [134]). As a result, x-rays passing from air into a thin film sample enter optically less dense medium and undergo total internal reflection below a certain critical glancing angle $\theta < \theta_c$ (Figure 3.6a). This results in a plateau in the measured intensity as illustrated in Figure 3.6c. Above θ_c the intensity decreases rapidly as the incident x-rays penetrate into the material. The most remarkable feature in Figure 3.6c is the occurrence of intensity oscillations (called *Kiessig fringes* [135]) with maximums observed whenever the path difference between the reflected and refracted radiation is a multiple

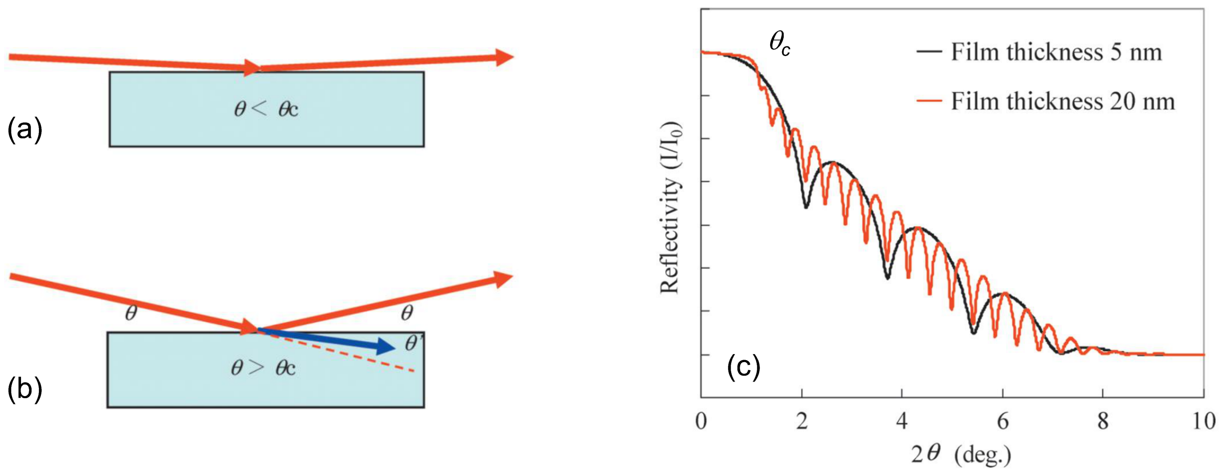

Figure 3.6: X-ray reflectometry. (a) Incident angle smaller than θ_c results in total reflection. (b) At an incident angle larger than θ_c x-rays penetrate into the material by refraction. (c) a XRR measurement example for 5 nm and 20 nm thick Au films on Si substrate. Figure adapted from [133].

of the wavelength λ. As evident from the illustration, the oscillation maxima will be more closely spaced with increasing film thickness. A quantitative treatment enables direct film (or also layer in case of multilayer structures) thickness measurements. Additionally, from the amplitude of the oscillations and the critical angle - the film density, from the decay rate of the XRR curve - the surface roughness and from the decrease in oscillation amplitude - the interface roughness values, can be extracted. A good overview including useful methods and practices in XRR measurements is provided by Rigaku technical article [133].

In this work, the XRR measurements, in the angular range from 0° to 6° were done by using a Rigaku SmartLab X-Ray diffractometer, Cu K_{α_1}-radiation (Ge[220] 2-bounce monochromator, λ=1.54059 Å) operating in parallel beam geometry.

3.2.3 X-ray photoelectron spectroscopy

X-ray photoelectron spectroscopy (XPS) is a technique for determining chemical composition of surfaces (due to the limited x-ray penetration and photoelectron escape depth) based on the photoelectric effect [136]. It is realized by irradiating a sample with monochromatic x-rays and analyzing the energy of the detected electrons. A schematic example of the photoelectron emission (a) and the corresponding XPS spectra (b) is illustrated in Figure 3.7. The kinetic energies of the emitted electrons are given by [137]:

$$KE = h\nu - BE - \phi, \tag{3.3}$$

where BE stands for the binding energy of the corresponding orbital, h is the Planck constant, ν is the frequency of the radiation and ϕ is the spectrometer work function. As each chemical element has a unique set of binding energies, XPS provides a tool for identification and quantification of the chemical

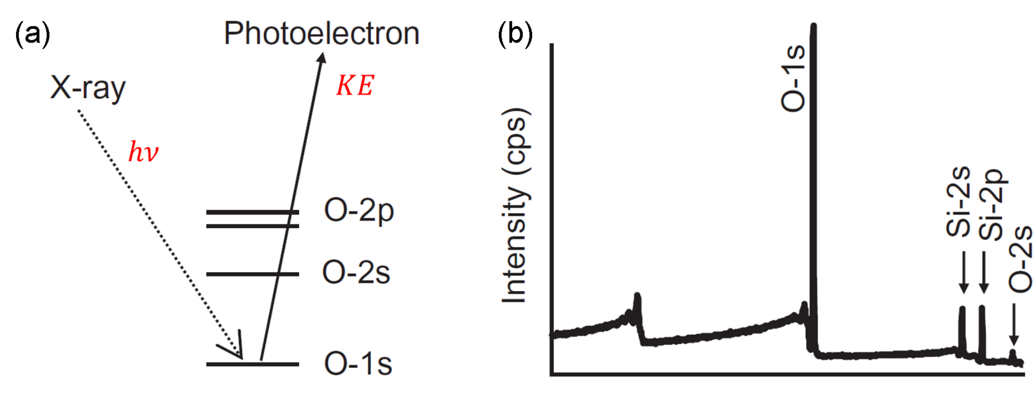

Figure 3.7: Schematic example of XPS. (a) The photoelectron process. (b) XPS spectra collected from a surface of oxide on a Si wafer. Figure adapted from [138].

elements present in the sample. Deviations from the elemental binding energies (chemical shifts) can be used to investigate the chemical state of the element in a compound material. Also depth-dependent studies are possible with using an additional ion gun for surface etching.

The XPS measurements were conducted with monochromatic Al K_α radiation using a PHI Versaprobe 5000 spectrometer. The experimental energy resolution of the spectrometer was 0.3 eV. The binding energies of the measured spectra were referenced with respect to the C 1s line. Surface charging was avoided by grounding the samples and additional neutralization where necessary. The measurements were done in collaboration with Dr. Philipp Komissinskiy at the TU Darmstadt, Materials Science department, Advanced Thin Film Technology research group.

3.2.4 Secondary ion mass spectroscopy

Secondary ion mass spectroscopy (SIMS) is a mass spectrometric-based technique for analyzing the composition of solid surfaces and thin films. A primary ion beam is focused onto a sample surface under vacuum conditions, resulting in ejection of atoms, molecules and secondary ions from the irradiated area of the material as shown in Figure 3.8. The secondary ions are then analyzed with a mass spectrometer creating the characteristic spectra. Depth-dependent measurements are possible and are very useful for multilayer studies. The elemental compositions of the thin film samples were investigated using a Cameca IMS 5f secondary ion mass spectrometer with 5.5 keV ^{133}Cs as primary ions, and positive polarity of the detected secondary ions. The measurements were done by Dr. Stefan Flege at the TU Darmstadt, Materials Science department, Materials Analysis research group.

3.2.5 Vibrating sample magnetometry

For magnetic characterization of bulk and powder samples, a vibrating sample magnetometer (VSM) [140] was used.

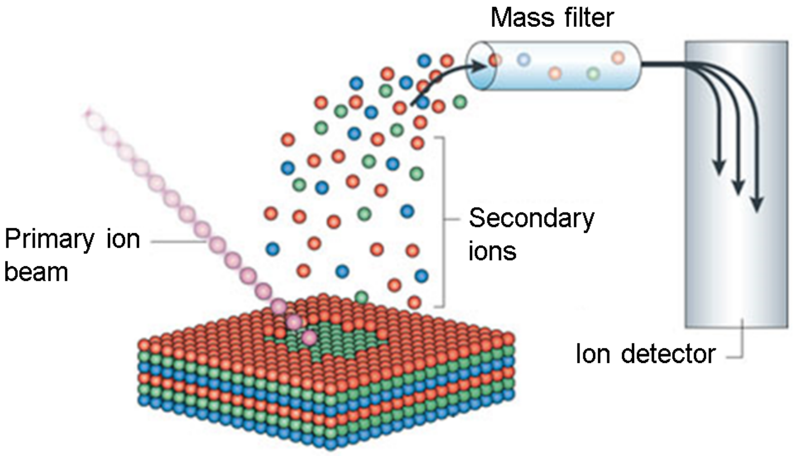

Figure 3.8: Secondary ion mass spectroscopy. Figure adapted from [139].

A sample is fixed on a vertical non-magnetic rod and vibrated vertically at a fixed frequency and amplitude in region of uniform magnetic field as illustrated by Figure 3.9. The magnetic field can be produced by a water-cooled electromagnet for low fields or using a superconducting magnet for high field options. According to *Faraday's law*, an alternating electromotive force proportional to the magnetic moment of the sample is induced in the pickup coils which is then processed and converted into the magnetic moment. Calibration with a known specimen has to be done beforehand as a reference.

The VSM measurements were performed using a 7400 Series, Lake Shore for not-air-sensitive samples. Measurement temperatures from 77 K to 1273 K can be realized and the maximum applied magnetic field is 2 T. For air-sensitive nanoparticle powders a Quantum Design Physical Property Measurement System (PPMS) device with a maximum field of 14 T and a temperature range of 1.9 K–1000 K was used.

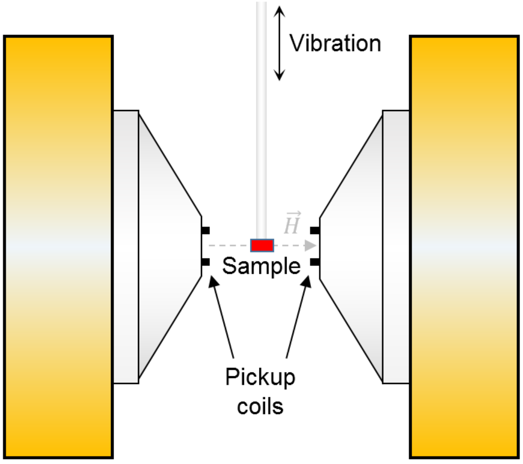

Figure 3.9: Schematic of a vibrating sample magnetometer.

3.2.6 SQUID magnetometry

A Superconducting quantum interference device (SQUID) magnetometer utilizes the Josephson effect [141]. The flux change in a superconducting circuit interrupted by an insulating layer is quantized [142]. Counting those flux quanta enables sensitive flux quantification and thus, high resolution magnetization measurements. Therefore, a SQUID magnetometer was used for the thin film characterization within this work.

The measurements were done in a Quantum Design Magnetic Property Measurement System (MPMS) SQUID with the magnetic field applied parallel and perpendicular to the film plane. The maximum applied field for the device used in this work is 7 T in a temperature range of 1.9 K–350 K.

3.2.7 Neutron diffraction

The neutron is an elementary particle with no charge, but possessing a magnetic moment of -1.91 μ_N [5], where μ_N is the nuclear magneton. As such, it can be used for investigating magnetic structures of elements and compounds. Neutrons are scattered by atomic nuclei and also by the unpaired spins of the atomic electrons. Since the magnetic scattering will depend on the magnitude and orientation of the magnetic moments, a complete magnetic unit cell structure can be determined from the positions and the intensities of the magnetic Bragg reflections, analogous to the interpretation of x-ray diffraction results.

Neutron diffraction experiments have been conducted by Prof. Olivier Isnard at the high-intensity powder diffractometer, D1B ($\lambda = 1.28\,\text{Å}$), at the Institut Laue-Langevin in Grenoble, France. The α''-$Fe_{16}N_2$ nanoparticle powders were contained in a cylindrical vanadium sample container. Diffraction patterns were collected over a 2θ angular range of 128° with steps of 0.1°. The measurements were done in a temperature range 1.5 K–305 K with wavelengths of 1.28 Å and 2.52 Å. Samples were handled without exposure to air in order to avoid oxidation. The Rietveld analysis of the data was performed using the FullProf Suite [143].

3.2.8 Electron microscopy

To gain insight into sample morphology and chemical composition on a naometer-scale, various imaging and spectroscopic methods offered by electron microscopy were used.

A scanning electron microscope (SEM) operates by rastering a fine electron beam of moderate energies (usually <30 kV) over a region of the sample. In this work a Philips XL30 FEG, 15 kV acceleration voltage, operated in secondary electron (SE) mode was used for imaging topology of large particles and nanoparticle clusters with the resolved features in a sub-micrometer range.

A transmission electron microscope (TEM) operates by irradiating a thin (<100 nm) lamella of the sample with a high-energy (up to 1 MV) electron beam and allows an order of magnitude higher resolution than SEM. Therefore for investigations of single nanoparticles and topological features on a nanometer-scale a JEOL JEM-2100F TEM was used.

A scanning transmission electron microscope (STEM) utilizes high-energy field emission gun that generates a probe size of 1 Å which is rastered across an electron transparent specimen. In this work for electron energy-loss spectroscopy (EELS), high-angle angular dark-field (HAADF) experiments in combination with STEM an aberration-corrected JEOL JEM ARM-F (scanning) transmission electron microscope was used. The microscope was operated at 120 kV to reduce beam damage.

The transmission electron microscopy investigations have been done in cooperation with Dr. Michael Duerrschnabel at the TU Darmstadt, Institute of Applied Geosciences, Geomaterial Science research group.

4 Structure and magnetic properties of γ'-Fe_4N thin films

The literature survey in Chapter 2 illustrated that a great amount of thin film studies have been conducted on the magnetic properties of the α''-$Fe_{16}N_2$ phase. However, a unified picture has not evolved yet, for example, because of problems with the phase purity, the presence of a buffer layer and the film thickness determination.

Therefore, in this work it was decided to focus on buffer-free samples, so that the magnetic properties originate exclusively from the Fe-N film and contributions from an Fe underlayer (as frequently used in literature) or interface effects are avoided. The most critical parameter for the determination of magnetic moments in thin films is an accurate estimation of the film thickness. For this reason, Fe-N samples have been prepared, whose thicknesses could be determined to a very high accuracy from the Kiessig fringes observed by x-ray reflectometry (thickness <100 nm).

To validate the reliability of the synthesis and measurements, well known and more stable phases were used as a reference. Therefore, the investigation of Fe-N system begins with pure α-Fe and γ'-Fe_4N.

For the detailed deposition parameters used here for sputtering of both α-Fe and γ'-Fe_4N thin films, the reader is referred to the experimental section.

Parts of the results presented in this chapter have been published by the author in Ref. [30].

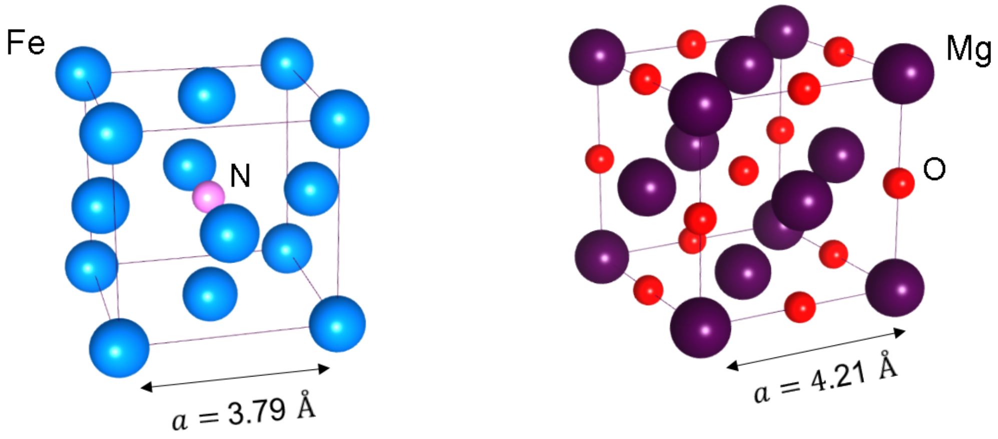

Figure 4.1: Crystal structures of γ'-Fe_4N and the MgO substrate showing the lattice misfit of ≈ 9.8 %.

4.1 Structural characterization

X-Ray diffraction $\theta - 2\theta$ scans of α-Fe and γ'-Fe_4N thin films on MgO (001) substrates are shown in Figure 4.2. For the pure Fe film, only the α-Fe (200) reflection is observed. The γ'-Fe_4N films are phase-pure and only the (100) reflection at 23.39 ° and the (200) reflection at 47.73 ° are observed, corresponding to a lattice constant of $a = 3.80$ Å. Decreasing the growth temperature below 673 K led to a decrease in film quality. Vacuum post-annealing at 673 K performed to increase the crystallinity resulted in nitrogen loss and the appearance of α-Fe reflections (not shown here). As mentioned in the introduction, a critical point for evaluating the magnetization in thin films is a reliable volume and density estimation. Here, the film thickness, the layer structure, and the density have been determined by XRR. Reflectivity data in the range from 0 ° - 5 ° was fitted with one additional interdiffusion layer at the interface to the substrate. In the case of pure iron, the interdiffusion layer was about 2 nm. The iron density obtained from the data refinement was about 98 ± 4 % of the single-crystal value of 7.875 g/cm^3. The same procedure was performed for γ'-Fe_4N thin films resulting in a thickness of about 27.4 ± 0.3 nm for the iron-nitride layer. The density was 105 ± 8 % of the single-crystal value of 7.21 g/cm^3. Assuming an interdiffusion layer at the substrate interface of about 0.85 nm gave a considerable improvement of the refinement. As can be seen in Figure 4.3, the film density and Kiessig fringes are well reproduced by the fit. The details of the modelling of the Ta cap layer including an oxidized top layer are justified by SIMS measurements (described later in the chapter), but do not affect the Fe_4N layer thickness itself.

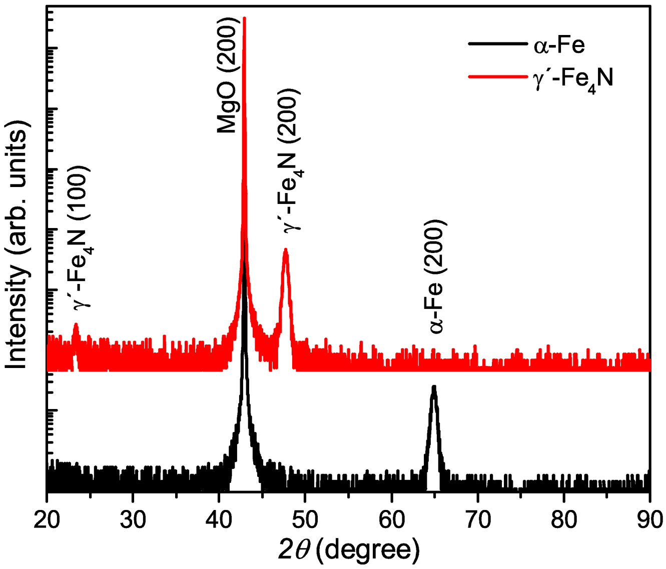

Figure 4.2: θ-2θ XRD scans for films deposited onto MgO (001) substrates. All the diffractograms presented in this chapter have been collected using Cu K_{α_1}-radiation (λ=1.54059 Å) and are presented on a logarithmic scale.

The MgO substrate has a cubic unit cell, space group Fm-$3m$ (225), with the lattice constant $a = 4.21$ Å. It consists of two face-centered-cubic sublattices - iron and oxygen, which are 45° rotated with respect to each other as illustrated by Figure 4.1. The γ'-Fe_4N unit cell is expected to grow directly on top of the MgO with an in-plane tensile strain (which would relax after several monolayers) due to the lattice

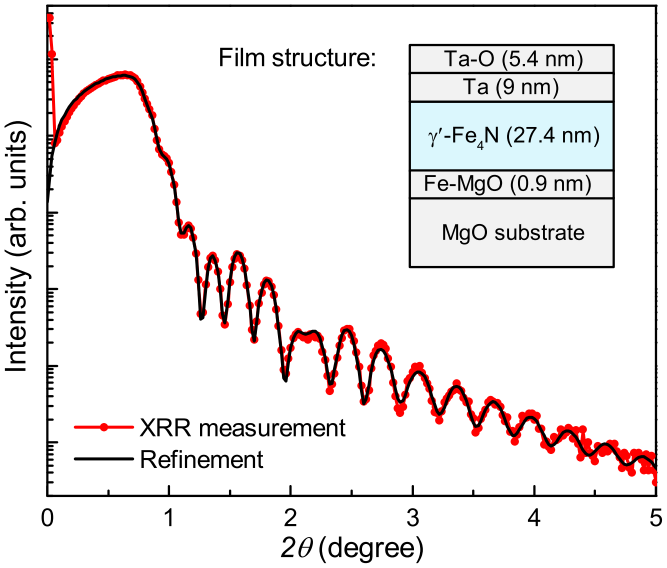

Figure 4.3: $\theta - 2\theta$ XRR measurement (red dotted curve) and the corresponding four layer fit (black line) for a γ'-Fe_4N thin film grown on MgO (100). The inset shows the simulated layer structure (not to scale).

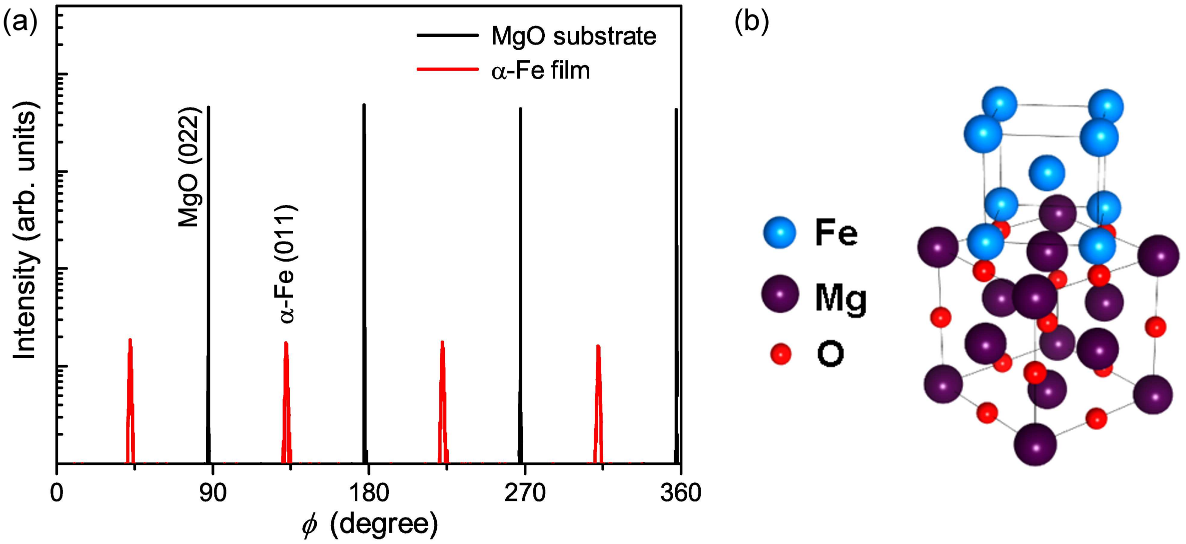

Figure 4.4: (a) ϕ-scans for MgO (022) and Fe (011) reflections. (b) A graphical illustration of the epitaxial relation.

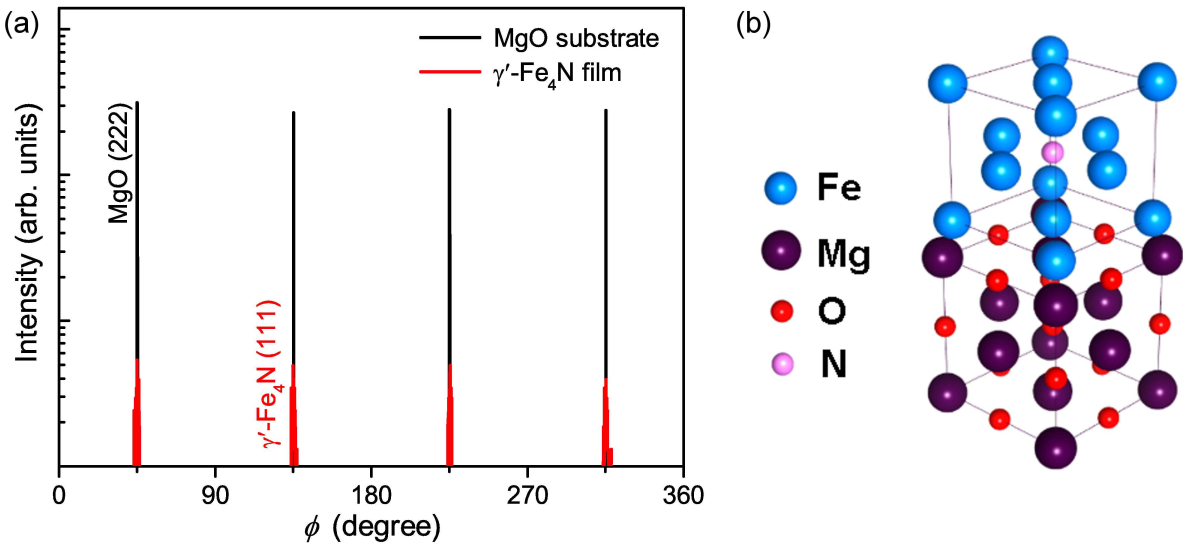

Figure 4.5: (a) ϕ-scans for MgO (222) and γ'-Fe_4N (111) reflections. (b) A graphical illustration of the epitaxial relation.

mismatch of ≈ 9.8 %. α-Fe has a lattice constant $a = 2.865$ Å and therefore is not fitting coherently onto the MgO. However, the O-O sublattice in MgO has a lattice constant of $a \approx 2.98$ Å which has a ≈ 3.8 % misfit with α-Fe and therefore iron is expected to grow 45° in-plane rotated onto the MgO substrate. In order to confirm this, standard ϕ-scans to determine the epitaxial relation between the film and substrate were performed. In the case of the α-Fe thin films, the MgO {022} and the α-Fe {011} peaks were used as shown in Figure 4.4. As expected, the cubic unit cell of bcc-Fe fits best to the substrate when it is rotated by 45° around the c-axis. The corresponding epitaxial relations are Fe (001) || MgO (001) and Fe [110] || MgO [100].

The same procedure, using MgO {222} and γ'-Fe_4N {111} reflections, was performed for the γ'-Fe_4N thin films and the results are shown in Figure 4.5. The growth mode is unambiguously cube-on-cube with the following epitaxial relations: γ'-Fe_4N (001) || MgO (001) and γ'-Fe_4N $\langle 100 \rangle$ || MgO $\langle 100 \rangle$.

4.2 Magnetic properties

In-plane and out-of-plane magnetization curves were obtained using a SQUID. The bare substrates have been measured independently for separating the thin film and substrate contributions to the magnetic signal. Pure iron films (with a Ta capping layer in order to prevent surface oxidation) were measured as a standard.

In-plane hysteresis loops at 10 K with the field aligned parallel to Fe (110) and γ'-Fe_4N (100) are shown in Figure 4.6. The volume saturation magnetization $\mu_0 M_s$ is 2.20 T ± 0.003 T for Fe and 1.96 T ± 0.002 T for γ'-Fe_4N corresponding to $2.23 \pm 0.09\,\mu_B$ and $2.30 \pm 0.09\,\mu_B$ per Fe atom, respectively. Within the measurement error the values are in agreement with the theoretically predicted [144]. As the Fe moment is close to the expected value of $2.22\,\mu_B$/Fe atom, it can be concluded that the measurement accuracy was satisfactory. The overall error in film volume calculations introduced by XRR thickness analysis and

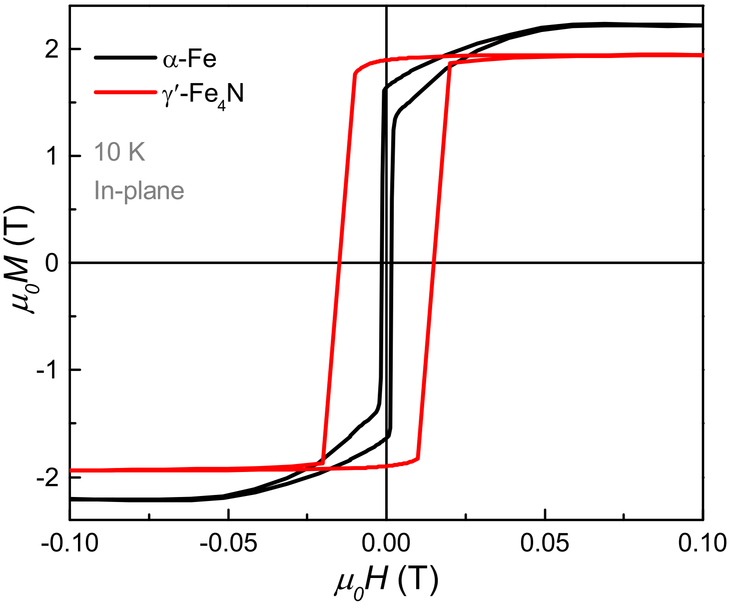

Figure 4.6: SQUID measured in-plane hysteresis loops for Fe and γ'-Fe_4N thin films. The film volume was obtained from the XRR refinement.

magnetometry is estimated to be around 4 %. The room-temperature saturation magnetization value of γ'-Fe_4N was 1.79 T ± 0.002 T which is in good agreement with previously reported values [145, 146]. In literature, an unusual increase in magnetization at temperatures below 60 K has been reported [145]. As this is observed also on bare substrates (not shown here), it can be attributed to paramagnetic substrate impurities. The coercivity of γ'-Fe_4N (150 mT) was found to be around one order of magnitude larger than for pure Fe (15 mT). As coercivity is an extrinsic material property, this increase should not be linked to the intrinsic anisotropy values of the samples, but rather interpreted as a difference in microstructural features (grain size, for example). In reality, the anisotropy constant K_1 for γ'-Fe_4N is $\approx 29\,\mathrm{kJ\,m^{-3}}$ [145], which is lower than the $\approx 50\,\mathrm{kJ\,m^{-3}}$ value for α-Fe [79]. The magnetization curves with the field parallel (in-plane) or perpendicular (out-of-plane) to the film plane for a α-Fe and γ'-Fe_4N thin films at 10 K are shown in Figure 4.7. The corresponding crystallographic directions were obtained from XRD ϕ-scans (see Figs. 4.4 and 4.5). The in-plane and out-of-plane curves intersect at around 2.4 T. Previously, this intersection has been measured for polycrystalline γ'-Fe_4N thin films to be 1.9 T [59]. Obviously, this anisotropy field is not reflecting any intrinsic magnetic anisotropy, but is due to the shape anisotropy of the thin film with a vanishing demagnetization factor, N_d, in-plane and $N_d \approx 1$ for the out-of-plane direction. For γ'-Fe_4N the $\langle 100 \rangle$ directions are the magnetic easy axes [64, 146]. Therefore, both in-plane and out-of-plane measurements, are along the easy directions.

Also for the α-Fe film, shape anisotropy is dominating the measurement. α-Fe magnetizes spontaneously along $\langle 100 \rangle$ directions and has $\langle 110 \rangle$ and $\langle 111 \rangle$ as the magnetic hard axes (opposite to the observed thin film anisotropy).

As the thermal stability in the vicinity of T_C ($\approx$ 760 K for bulk) [147] of γ'-Fe_4N is unclear, direct $M(T)$ measurements to determine the phase transition temperature are difficult. Therefore, $M(H)$ loops in the temperature range of 10 K to 800 K in intervals of 50 K with a heating rate of $12\,\mathrm{K\,min^{-1}}$ and 5 min

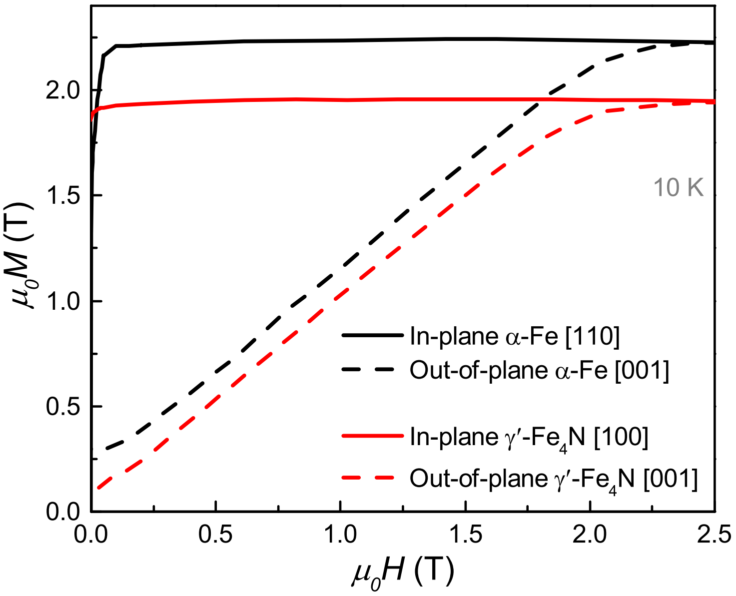

Figure 4.7: In-plane and out-of-plane magnetization curves for α-Fe and γ'-Fe$_4$N thin films ($T = 10\,\mathrm{K}$) showing the thin film shape anisotropy.

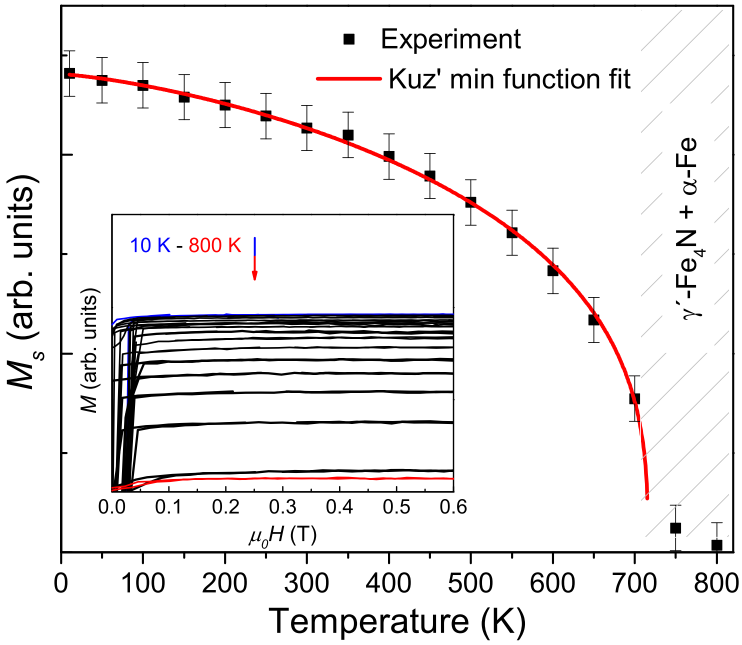

Figure 4.8: $M_s(T)$ constructed from in-plane $M(H)$ loops (shown in the inset) for a γ'-Fe$_4$N thin film.

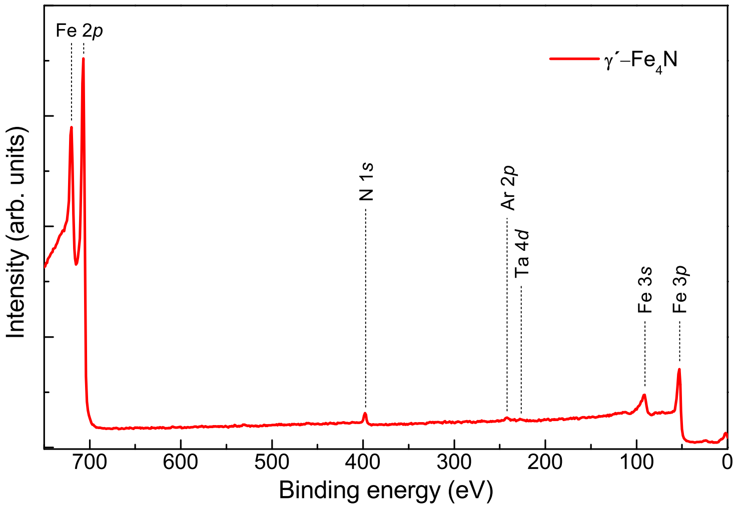

Figure 4.9: XPS survey spectra of a γ'-Fe$_4$N thin film. In addition to Fe and N, small signals from Ar as well as Ta caping layer are present.

to stabilize the corresponding temperature (see inset Figure 4.8) have been measured. The Curie temperature T_C was obtained by fitting the constructed $M_s(T)$ plot (Figure 4.8) using the Equation 2.10. The so-determined Curie temperature is 716 K using $s = 0.66$ and $p = 1.16$. Inaccuracies in the M_s determination caused by the subtraction of the substrate contribution, glue and sample holder signals are represented by error bars in the plot. Note that film decomposition is evident from the fact that a finite magnetic moment is observed even above T_C. The region of decomposition is indicated by the hatched area in Figure 4.8. The appearance of α-Fe in the XRD pattern after the $M(H)$ measurement sequence (not shown here) indicates that γ'-Fe$_4$N decomposes into α-Fe by releasing nitrogen at high temperatures.

4.3 Chemical composition and electronic structure

Chemical composition and electronic structure of γ'-Fe$_4$N as well as α-Fe thin films were studied by means of SIMS and XPS.

The survey spectra of the films including the thin Ta capping layer revealed Ta, Fe, and N emission lines as well as the lines of adventitious carbon and oxygen (not shown). After gradual Ar$^+$ ion etching, those signals were becoming weaker and after sputtering for 49 min at 1 keV no emission lines of oxygen, carbon and other impurities could be detected as shown in Figure 4.9. Prominent intensities from Fe and N are visible with very weak contributions from Ar (most likely from the ion milling) and some leftover Ta from the capping layer. Also, no shift in the positions of the Fe 2p and the N 1s peaks was observed before and after ion milling. Therefore, it is concluded that the ion milling has no detrimental effect.

Fe 2p, N 1s, and valence band (VB) XPS spectra are shown in Figure 4.10. The Fe 2p spectra in α-Fe and γ'-Fe$_4$N are identical and the positions of the Fe 2p peaks (Fe 2$p_{3/2}$ at 706.8 eV and Fe 2$p_{1/2}$ at 719.9 eV) correspond to metallic Fe. The N 1s spectrum of the γ'-Fe$_4$N film has two peaks (see bottom inset in Figure 4.10). The intensive peak at 398.0 eV corresponds to the typical N 1s peak in nitrides [137]. The

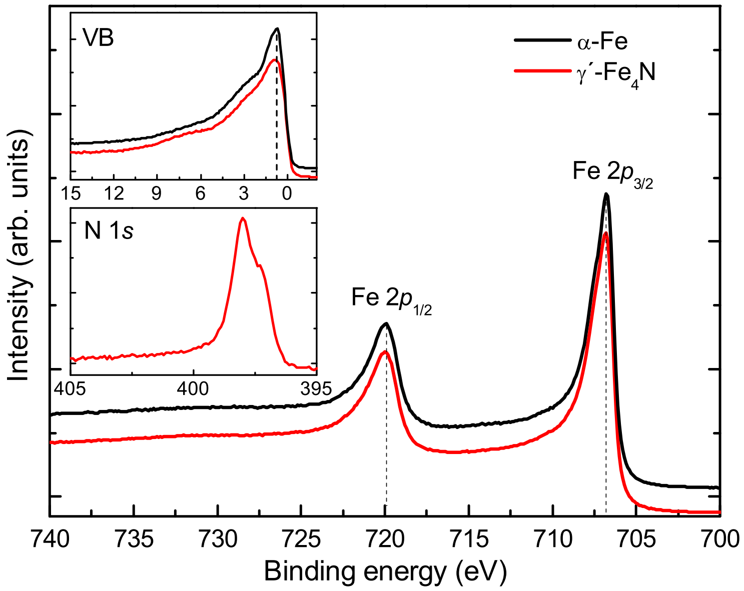

Figure 4.10: XPS spectra of Fe 2p, valence band and N 1s binding energies for corresponding α-Fe and γ'-Fe$_4$N thin films.

intensity of the weak N 1s peak at 397.3 eV decreases with longer ion milling. Thus, this peak can be associated with Ta-N bonding. The binding energies of the Fe 2p and N 1s 398.0 eV peaks observed in the γ'-Fe$_4$N films are in reasonable agreement with previously reported data and indicate weak covalent Fe-N bonding in γ'-Fe$_4$N [148, 149, 150, 151]. In contrast, a shift of the Fe 2p and N 1s peaks to higher energies was measured earlier [152, 153]. The overall shape of the valence band spectra of the Fe and γ'-Fe$_4$N thin films is similar with only slightly higher intensity of the peak at 0.9 eV for the Fe sample (top inset in Figure 4.10). A low-intensity peak between 6 eV and 9 eV for the γ'-Fe$_4$N sample is attributed to surface N 2p levels [149, 151, 117]. Thus, the valence band structure of the γ'-Fe$_4$N film is stable and affected only little by the weak covalent Fe-N bonding. A detailed analysis of the small valence band features is hampered due to the low intensity of the VB emission.

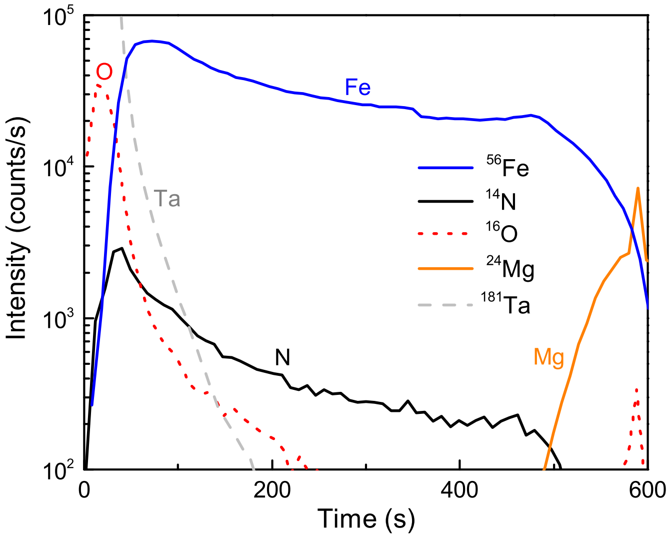

Figure 4.11: SIMS data on a γ'-Fe$_4$N film, showing iron, nitrogen, oxygen, magnesium and tantalum signals (Ta is an atomic ion, while the others are cluster ions of the type (CsX).

SIMS results are shown in Figure 4.11. As observed also in the XPS measurements, the surface is oxidized and O is present within the Ta layer. This justifies the assumption of an oxidized Ta-layer on top of the capping Ta for the XRR refinement. The gradual decrease of Ta with depth might indicate Ta diffusion into the γ'-Fe_4N film. At the film-substrate interface, the SIMS data suggests an interdiffusion layer. This is also in accordance with the interdiffusion layer assumed for the refinement of the XRR data and with literature [154]. From the observation that only Fe (not N) is diffusing into the substrate, it might be concluded that the larger kinetic energy of the Fe species during the sputtering process allows iron to penetrate the substrate. The most important point is that the SIMS data confirm the assumptions made for the XRR refinement and, thus, underpin the accuracy of the magnetization measurement.

4.4 Summary and conclusions

γ'-Fe_4N thin film samples have been successfully grown epitaxially onto a MgO (001) substrates. A comprehensive analysis of the structure, elemental composition, electronic, and magnetic properties of the samples has been conducted.

The growth mode was unambiguously cube-on-cube with the following epitaxial relations: γ'-Fe_4N (001) || MgO (001) and γ'-Fe_4N $\langle 100 \rangle$ || MgO $\langle 100 \rangle$. The sample surface is oxidized and O is present within the Ta capping layer. No other impurities could be detected in the γ'-Fe_4N films. A weak covalent Fe-N bonding is indicated by the XPS data.

The film thickness was extracted from XRR data refinement in order to obtain an accurate estimation of the magnetic moment. The assumptions made for the XRR refinement are in full agreement with SIMS measurement results obtained on the same sample. The magnetic moment per Fe atom in γ'-Fe_4N is $2.30 \pm 0.09\,\mu_B$ at 10 K which is in agreement with the theoretically predicted moment. The results exclude a giant magnetic moment, but indicate a slight increase in magnetic moment per Fe atom that could be attributed to the lattice expansion caused by the presence of interstitial nitrogen.

The Curie-temperature is estimated to be approximately 716 K by extrapolation of the $M_s(T)$ fit to experimental data. Since γ'-Fe_4N decomposes into α-Fe by releasing nitrogen at elevated temperatures, the direct measurement of T_C was not possible.

As the next step, the deposition parameters ought to be adjusted for moving towards α'-Fe_8N_x and α''-$Fe_{16}N_2$ phases.

5 Structure, and magnetic properties of α'-Fe_8N_x thin films

In this chapter, the structure and magnetic properties of body-centered tetragonal Fe as a function of volume expansion driven by nitrogen incorporation is studied. The reader is referred to Chapter 2 for more details on the α'-Fe_8N_x phase).

One way to investigate the effect of a lattice expansion in α-Fe would be the use of strained thin films [155, 156, 157]. The drawback of such experiments is, first, that the strain can only be maintained in ultra-thin films of a few unit cells and second, that large strains beyond a few percent cannot be achieved.

Another way of stabilizing a tensile strain in iron is the use of interstitial nitrogen atoms. Therefore, in this work the increase of the unit cell volume is realized in Fe_8N_x buffer-free and epitaxial thin films grown onto MgO (001) single-crystal substrates. The observed unit cell deformation has been correlated with the magnetic moment as well as increased magnetic anisotropy by systematically changing the amount of added nitrogen, allowing a comparison to the theoretical predictions.

An important questions is, whether the high magnetic moment in the iron-nitrogen martensite is caused by the lattice expansion, or whether the ordering of nitrogen atoms plays the key role as suggested by Ji et al. [158]. Also, the concurrent changes in the magnetocrystalline anisotropy and critical behavior are of practical interest. For this reason, an attempt to induce the N atom ordering by an additional heat treatment step is presented at the end of the chapter.

The results presented in this chapter have been published in References [31] and [32].

5.1 Film growth: moving from Fe_4N to Fe_8N

For the growth of α'-Fe_8N_x and possibly also the α''-$Fe_{16}N_2$ phases the conditions used for the deposition of γ'-Fe_4N (see Chapter 4) were used as the initial state. Detailed thin film deposition parameters are described in Chapter 3.

The formation enthalpy of the α''-$Fe_{16}N_2$ is reported to be slightly positive with $\Delta_f H^0 = 85.2 \pm 46.8\,\mathrm{kJ\,mol^{-1}}$ [159] which reflects the metastability of the phase. Therefore, finding the right growth conditions is the key for synthesis of phase-pure samples. According to the phase diagram (Figure 2.1) and in literature reported temperature stability [116, 160], in order to move from γ'-Fe_4N to the α'-Fe_8N_x/α''-$Fe_{16}N_2$ region, one needs to reduce the nitrogen concentration in the plasma gas and use lower deposition temperatures. This is demonstrated in Figure 5.1. All the XRD data is presented in logarithmic scale in order to emphasize the possible low-intensity superstructure reflections. The bottom

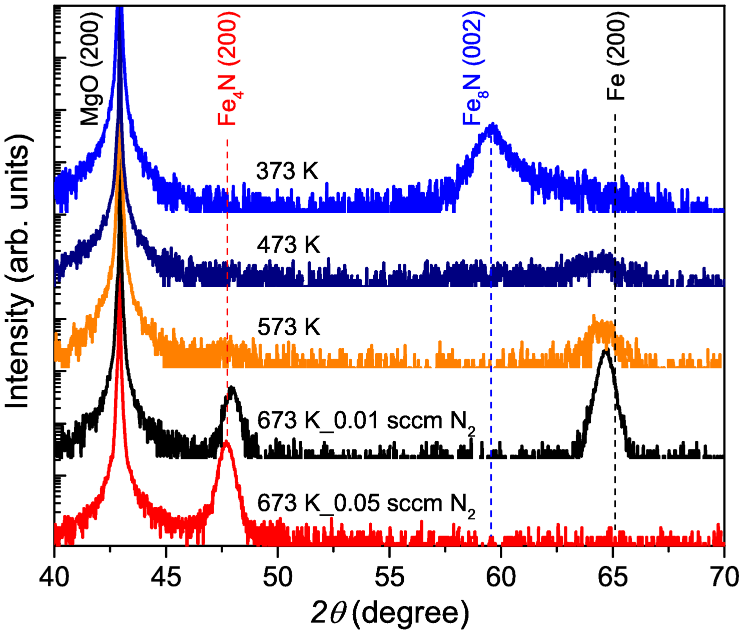

Figure 5.1: $\theta - 2\theta$ XRD scans for transition from γ'-Fe$_4$N (red bottom curve) to α'-Fe$_8$N$_x$ (blue top curve). Thin films deposited onto MgO (001) substrates. Nitrogen content has been kept constant for the lower temperatures. All the diffractograms presented in this chapter have been collected using Cu K_{α_1}-radiation (λ=1.54059 Å) and are presented on a logarithmic scale.

(red) curve represents the γ'-Fe$_4$N deposited at 673 K. Firstly, all the other deposition parameters (RF power, chamber pressure, gas flow, argon flow, temperature) have been kept the same as for the γ'-Fe$_4$N, but the nitrogen flow reduced from 0.05 sccm to 0.01 sccm. As expected from the phase diagram due to the scarcity of nitrogen the sample consists of a mixture of γ'-Fe$_4$N and α-Fe (the black XRD pattern). Keeping the nitrogen concentration in plasma constant, the deposition temperature was gradually reduced to 573 K, 473 K and 373 K respectively. As a result, the reflections from γ'-Fe$_4$N and α-Fe fade and (002) reflection of α'-Fe$_8$N$_x$ appear. A low intensity disordered background signal is still visible in the angular range of $\approx$ 60°–65°. It can also be seen that the γ'-Fe$_4$N (200) reflection shifts to slightly higher angles with lower N content, corresponding to decrease in the lattice constant. This can be understood by the fact that the unit cell dimensions of nitrogen austenite shrink roughly linearly with decreasing nitrogen content as shown by Jack [41].

5.2 Structural characterization

In order to investigate the development of the magnetic properties with unit cell expansion in α-Fe, a series of α'-Fe$_8$N$_x$ thin films in the full range of $0 \leq x \leq 1$ were deposited by varying the nitrogen concentration in the plasma gas. The corresponding XRD $\theta - 2\theta$ scans of α-Fe (only Ar as the sputtering gas) and α'-Fe$_8$N$_x$ thin films grown onto MgO (001) substrates at a temperature of 373 K are shown in Figure 5.2. In the case of pure argon, only reflections from the substrate and α-Fe were observed. As only the Fe (200) reflection is present, likewise to the previous study on γ'-Fe$_4$N (see Chapter 4), also in this case, the iron grows epitaxially onto the MgO (100) (see Figure 4.4 for substrate-film orientation). On the other hand, in contrast to the case for γ'-Fe$_4$N, here the (200) reflection is observed at a slightly lower angle, 64.28° instead of the theoretical 65.05°. This indicates a slight unit cell expansion along the out-of-plane direction. Two mechanisms could be responsible for this. First, as mentioned in the previous chapter, bcc Fe has a $\approx 3.8\,\%$ lattice mismatch with MgO which should result in an in-plane tensile strain at the interface. However, as the unit cell volume would tend to remain constant, actually a decrease in the out-of-plane lattice constant could be expected. The second possibility is the incorporation of Ar atoms during the sputtering process. As these samples are deposited at relatively low temperatures (373 K instead of 673 K as in the case for γ'-Fe_4N), the atom mobility due to the thermal motion is much lower. The latter hypothesis could be partially supported by the XPS results described later in the chapter.

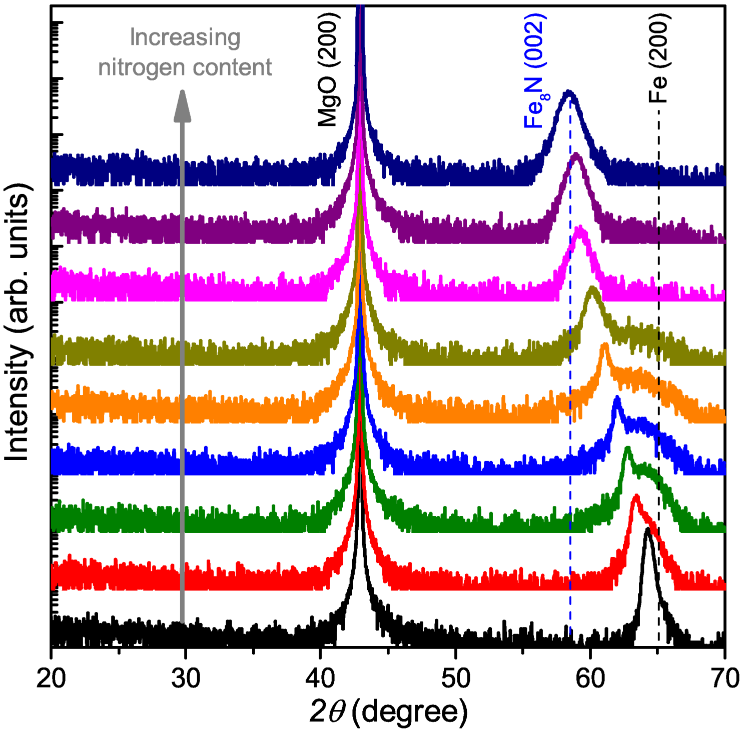

Figure 5.2: $\theta - 2\theta$ XRD scans for α-Fe (black bottom curve) and α'-Fe_8N_x thin films deposited onto MgO (001) substrates at different argon/nitrogen mixtures as the plasma gas. The spectra are offset from each other with the nitrogen content increasing from bottom to top. The slightly increased background signal in the range of 20°–40° is caused by the reflection of the glass plate used as sample holder.

When nitrogen is added to the plasma gas, two things happen. The first observation is that the sharp α-Fe (200) reflection starts to shift to lower angles corresponding to an expansion of the out-of-plane lattice constant. In other words, the bcc unit cell of Fe is expanded along the [001] direction. The second observation is that a rather broad background peak develops at the position of the original α-Fe (200) reflection. This indicates that a part of the Fe atoms form nanocrystalline clusters that prevail until the phase transition to α'-Fe_8N is almost completed. When adding the right amount of nitrogen to the plasma, one obtains a reflection at $\approx 58.5°$ corresponding to a lattice constant of ≈ 3.15 Å. This is very close to the expected c lattice constant of the α'-Fe_8N martensite (about 3.145 Å at 58.66°).

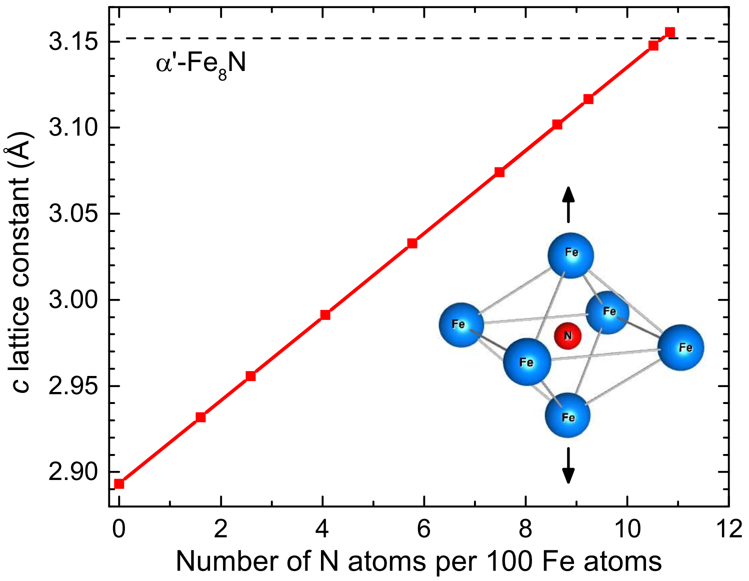

Figure 5.3: Out-of-plane c-axis lattice parameters of α'-Fe_8N_x as a function of the number of dissolved nitrogen atoms per 100 iron atoms.

As the ordered α''-$Fe_{16}N_2$ phase has its (004) reflection at the same 2θ position where the (002) reflection of α'-Fe_8N martensite is situated and therefore cannot be distinguished, measurements specifically at low angles have been performed to visualize possible superlattice reflections related to α''-$Fe_{16}N_2$. Since no superstructure reflections indicating nitrogen ordering are visible, it is concluded that the samples do not have substantial amount of the secondary martensite α''-$Fe_{16}N_2$ phase.

The key observation is that there is a gradual transition from the α-Fe (200) reflection into the α'-Fe_8N (002) reflection accompanied by a gradual increase in lattice constant or volume expansion of the unit cell due to the increased incorporation of interstitial nitrogen. The α'-Fe_8N_x can be continuously formed as thin films in the full range from $x = 0$ to $x = 1$.

The c-axis lattice parameter values for the films deposited at different nitrogen concentrations have been calculated from the $\theta - 2\theta$ scans shown in Figure 5.2 according to *Bragg's law*. The results are plotted in Figure 5.3 as a function of the dissolved nitrogen atoms per 100 iron atoms, X_N. X_N was calculated using the Relation 2.2 as reported by Cheng et al. [66], reflecting the nitrogen content in α'-Fe_8N_x. At the endpoint of the series, the nitrogen concentration was such that the unit cell expansion along the c-axis reached a lattice spacing of 3.15 Å which corresponds to the formation of α'-Fe_8N_1 with a c/a ratio of approximately 1.1. The increase of the c-axis is consistently observed in two independent experimental series to be a linear function of the nitrogen content in the plasma which is consistent with *Vegard's law* [161].

Hence the α'-Fe_8N_x samples are epitaxial, only the out-of-plane lattice parameters could be evaluated from the standard $\theta - 2\theta$ scans. Therefore, in order to measure the evolution of the in-plane lattice spacing values, the films were tilted in $\chi = 45°$ angle and the Fe (011) reflection was used. Consequently, as the c-axis lattice parameters are known, the a and b can be calculated from the respective (011)

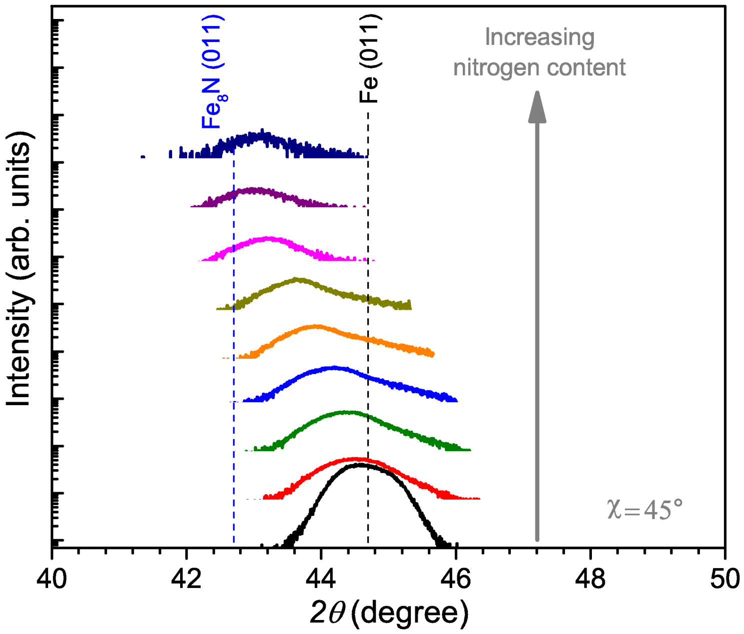

Figure 5.4: $\theta - 2\theta$ XRD scans for (011) reflection ($\chi = 45°$) in α-Fe and α'-Fe_8N_x thin film series. The colour code matches the Figure 5.2.

distances by applying basic geometry relationships, as $b = \sqrt{(2 \cdot d_{011})^2 - c^2}$. This approach unfortunately leads to a significant loss in the diffraction intensity.

Figure 5.4 shows the results for all the samples in the α'-Fe_8N_x series. A clear shift to lower angles with nitrogen content is observed indicating an increase in the (011) lattice plane spacing. This is due to the previously mentioned expansion along the [001] direction. A slightly decreasing trend in agreement with reported values for iron-nitride powders [41] (see Figure 2.5) is actually occurring, however, due to the weak intensity for the in-plane XRD measurements the exact values could not be obtained (the results are presented in Table 5.1). Therefore, the a and b values for the determination of the unit cell volume have been calculated from the linear relationship as reported for bulk material [66] according to Equation 2.1.

Thin films with sufficiently high smoothness on the atomic scale possessing minor surface and interface roughness offer the advantage of an accurate thickness determination by XRR as illustrated in Ref. [133]. This is required for a precise calculation of magnetization. In the previous chapter XRR proved to give reliable results for α-Fe and γ'-Fe_4N thin films and therefore has also been applied here for the α'-Fe_8N samples.

The reflectivity data of a α'-Fe_8N thin film that was fitted in the range from 0°–5°, assuming an additional interdiffusion layer at the interface to the substrate (Figure 5.5). This interdiffusion layer has a reasonable thickness of about 1 nm. The α'-Fe_8N layer itself has a thickness of 66.6 nm ± 0.3 nm. The Ta capping layer was approximately 5 nm, as intended. The fit could be improved by assuming a sub-nanometer Ta oxide surface layer due the exposure to the ambient atmosphere prior to the XRR measurement. However, the introduction of this layer into the refinement does not alter the refined thickness of the α'-Fe_8N layer. The density of the α'-Fe_8N layer is about 97 % ± 8 % of the α-Fe value (7.875 g cm^{-3}). As can be

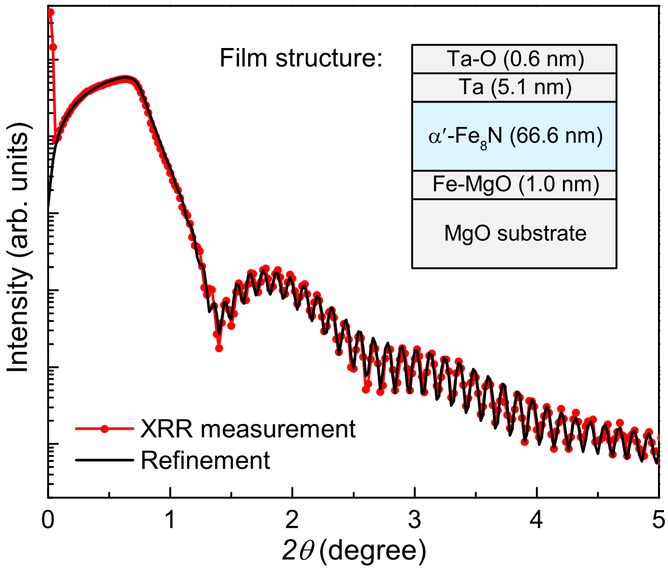

Figure 5.5: XRR measurement (red dotted curve) and the corresponding four layer fit (black line) for a α'-Fe_8N thin film grown on MgO (100). The inset shows the simulated layer structure (not to scale).

seen in Figure 5.5, the film density and Kiessig fringes are well reproduced by the fit. The measured α'-Fe_8N layer thickness was used for the magnetic moment calculations. Unfortunately, this approach introduces errors in the film volume calculations due to the presence of Fe in the interdifussion zone. Even more, the above mentioned nanocrystalline clusters of Fe atoms, as evident in the XRD data, lower the accuracy further.

A summary of the structural characterization results data is given in Table 5.1. The first row corresponds to theoretical values for pure, strain-free bcc α-Fe. The values marked with a star are calculated using the linear relations from Ref. [66] as described in the text above.

Table 5.1: Structural characterization summary for the α'-Fe_8N_x thin film series.

X_N *	(002) (°)	(011) (°)	a^* (Å)	a (Å)	c (Å)	c/a	Thickness (nm)
α-Fe theor.	65.05	44.69	2.865	2.865	2.865	1.00	-
0.00	64.35	44.57	2.87	2.85	2.89	1.01	65.64
1.60	63.40	44.55	2.86	2.81	2.93	1.02	62.29
2.59	62.83	44.40	2.86	2.81	2.96	1.03	64.96
4.05	62.00	44.19	2.86	2.80	2.99	1.05	61.19
5.77	61.06	43.93	2.86	2.79	3.03	1.06	64.01
7.48	60.15	43.70	2.85	2.77	3.07	1.08	65.99
9.24	59.25	43.23	2.85	2.79	3.12	1.09	67.60
10.51	58.61	43.06	2.85	2.78	3.15	1.10	70.90
10.84	58.45	43.06	2.85	2.77	3.16	1.11	90.80

* calculated according to Ref. [66]

5.3 Magnetic properties

5.3.1 Magnetic moment

In-plane and out-of-plane magnetization curves were obtained using a SQUID. The bare substrates were measured independently for separating the thin film and substrate contributions from the magnetic signal. Pure iron films (with a Ta capping layer in order to prevent surface oxidation) were measured as a standard.

The in-plane hysteresis loops for the samples with different nitrogen content and thus unit cell expansion, measured at 10 K with the field aligned parallel to the Fe (110) direction, are shown in Figure 5.6. The magnetization of the pure Fe film was close to 2.2 T, thus akin to the case of γ'-Fe$_4$N, the measurements can be considered as reliable. By obtaining the Fe-N film volume according to substrate lateral dimensions and from XRR extracted layer thickness, the volume magnetization values have been calculated. The volume saturation magnetization reaches approx. 2.39 T ± 0.12 T for a film with a lattice constant of $c =$ 3.12 Å. This clearly indicates the increased average magnetic moment per Fe atom compared to α-Fe.

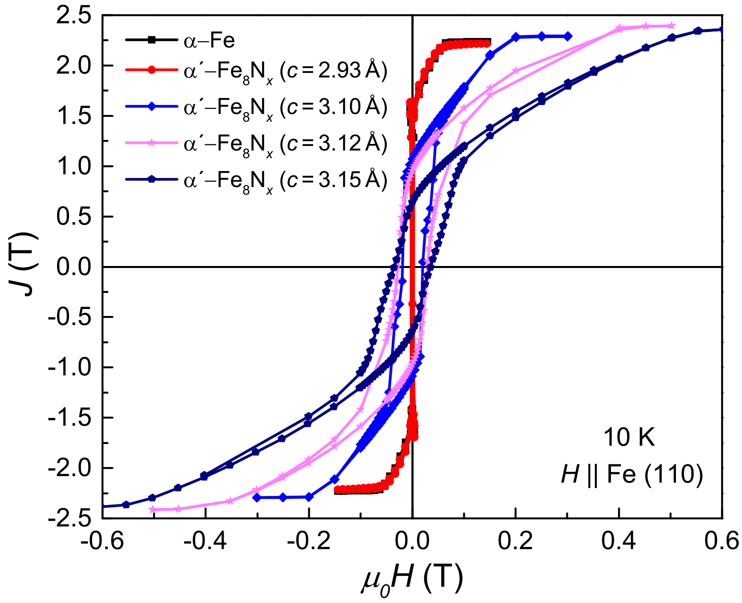

Figure 5.6: In-plane hysteresis loops for α-Fe and α'-Fe$_8$N$_x$ thin films. The film volume was calculated according to the film thickness obtained from XRR refinements.

It has to be mentioned that SEM investigations show that some material is also being deposited onto the sides of the substrate, thus, in reality the volume of the magnetic material is higher than considered in the above calculation of the magnetic moment. This would lead to a lower magnetic moment and magnetization values, respectively. Unfortunately, due to the problematic quantification of the amount of this 'extra' material, it has not been taken into account, but the resultant deviation should be kept in mind.

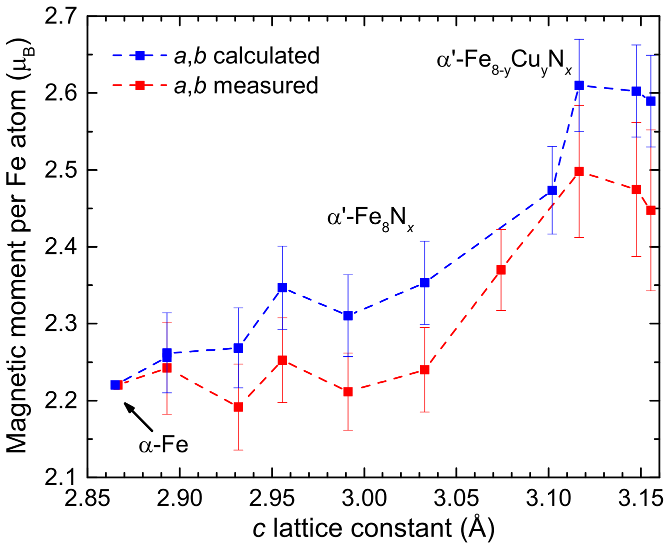

Figure 5.7: Magnetic moment per Fe atom in α'-Fe$_8$N$_x$ in dependence of the lattice parameter for the calculated (blue) and experimentally from the in-plane XRD measurements estimated (red) a and b values. A small amount of Cu onto which the Fe target was bonded, was co-sputtered into the last films in the series as indicated by the label.

Another important feature in Figure 5.6 is the shape of the hysteresis loops. It reflects a two-phase behavior for the α'-Fe$_8$N$_x$ thin film samples as evident from the heterogeneous demagnetization process. This affirms the XRD out-of-plane $\theta - 2\theta$ scan results, which suggested the presence of residual α-Fe clusters from the non-vanishing shoulder around the Fe (200) angle.

Subsequently, the correlation between the magnetic moment and the unit cell expansion in α'-Fe$_8$N$_x$ was investigated. The average magnetic moments per Fe atom (assuming that N carries no moment) in α'-Fe$_8$N$_x$ series were obtained by calculating the unit cell volume from the lattice parameters summarized in Table 5.1 and using the measured magnetic moment. From a structural point of view, the α'-Fe$_8$N$_x$ was treated as a bct expanded α-Fe, thus possessing two Fe atoms per unit cell.

The results are shown in Figure 5.7. The magnetic moment per Fe atom in α'-Fe$_8$N$_x$ is plotted as a function of the c-axis lattice parameter. Both cases are presented, with the calculated and experimentally from the in-plane XRD measurements derived a, b lattice parameters. Despite the large amount of work on the Fe-N system, a consistent correlation between lattice expansion and magnetization is elusive. Takahashi et al. [93] have shown a slight increase of the saturation magnetization as a function of unit cell volume as compared to bulk iron ($\approx 4\,\%$), with a further increase in magnetization (about 7 %) being attributed to the phase formation of α''-Fe$_{16}$N$_2$ [27]. In the present data, there is a clear increase in magnetic moment per Fe following the lattice expansion. The maximal obtained value is $2.61\,\mu_B \pm 0.06\,\mu_B$ and $2.50\,\mu_B \pm 0.09\,\mu_B$ per Fe atom in the case of calculated and measured a, b, respectively. Compared to α-Fe, this corresponds to an increase of about 17.5 % or 12.6 %. The findings are in good agreement with experimental results in iron nitrides [94, 162, 163, 153, 86, 164], and also in good agreement with theoretical predictions [74, 75, 53, 99, 165].

Table 5.2: Increased inter-atomic separation r_{ab} in α'-Fe$_8$N$_x$ due to the interstitial nitrogen.

Phase	a, b (Å)	c (Å)	r_{ab} (Å)	r_{ab}/r_d
α-Fe	2.865	2.865	2.48	3.26
α'-Fe$_8$N$_{0.5}$	2.86	3.03	2.53	3.32
α'-Fe$_8$N$_1$	2.85	3.15	2.56	3.37

The key point here is that the increased magnetic moment cannot be attributed to a specific stoichiometry, but it increases proportional to the lattice expansion following the nitrogen incorporation in α'-Fe$_8$N$_x$. The saturation in magnetization for the three largest lattice constants might be an artifact of the thin film fabrication by magnetron sputtering. Due to the thinning down of the target during sputtering, a small amount of Cu onto which the Fe target was bonded, was co-sputtered into these films (which could also be detected by XPS).

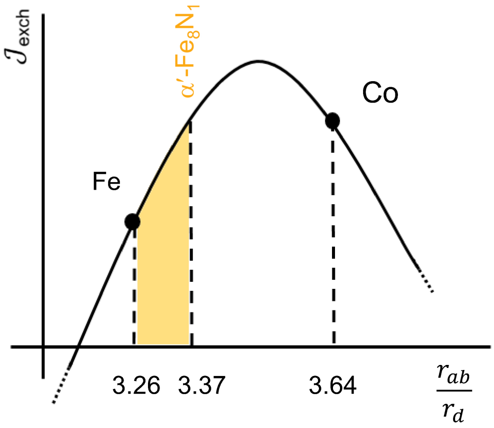

Figure 5.8: A section of the Bethe-Slater curve (Figure 2.7), showing the increase in $\mathcal{J}_{exch}$ when moving upwards from α-Fe to α'-Fe$_8$N due to the increased inter-atomic separation r_{ab}. The shaded area represents the α'-Fe$_8$N$_x$ region.

The increase in magnetic moment is related to the increase of the mean volume of Fe atom in a solid, which is a continuous function of the amount of nitrogen interstitials as described in Chapter 2. The nitrogen interstials increase the inter-atomic separation r_{ab} decreasing the degree of the d-orbital overlap and thus move the Fe up along the left shoulder in the Bethe-Slater curve (Figure 2.7). This is illustrated schematically in Figure 5.8. The shaded area represents the α'-Fe$_8$N$_x$ series from the present work. By using the experimentally determined c lattice parameter and the calculated a, b lattice parameters and assuming that the d-orbital radius r_d remains unchanged at 0.76 Å calculated r_{ab}/r_d are summarized in Table 5.2. Three cases are distinguished, the initial α-Fe, the intermediate Fe$_8$N$_{0.5}$ and the final Fe$_8$N$_1$, where r_{ab}/r_d reaches ≈ 3.37 for α'-Fe$_8$N$_1$ composition. The exchange integral $\mathcal{J}_{exch}$ increases continuously with x, which results in an enhanced magnetic moment.

5.3.2 Magnetic anisotropy

In this section the correlation between crystalline and magnetocrystalline anisotropy is studied. It is visible from the shape of the hysteresis in Figure 5.6 that the magnetic field (applied in-plane) it takes to fully saturate the different samples within the α'-Fe_8N_x series increases with the c-axis lattice parameter and the tetragonal unit cell expansion (nitrogen content), respectively. The pure α-Fe films already display an increased anisotropy. This is due to the large number of growth defects during the low-temperature synthesis and the large lattice mismatch to MgO.

Figure 5.9 shows the increase in the in-plane saturation field with increasing c/a ratio (the inset illustrates the relevant parts of the hysteresis loops). It could also be presented with the c-axis lattice parameter or the nitrogen content on the abscissa. This increase of the in-plane saturation field is associated with an increase in the intrinsic magnetocrystalline anisotropy, since all other factors contributing to magnetic anisotropy are constant for the thin films under consideration. The nitrogen incorporation thus leads to a strong enhancement of the magnetic moment per Fe atom due to the lattice expansion effect as shown above and also to an increase in magnetocrystalline anisotropy. The highest value of the in-plane saturation field is about 0.615 T for the film with the largest lattice constant and less than 5 % Cu impurities. This leads to the conclusion that the magnetic easy axis shifts to the tetragonally distorted c direction. The observations are in agreement with previous theoretical [101] as well as experimental [86] results on Fe-N. It has however been predicted that in bct Fe an easy axis reorientation from [001] to [100] occurs at a ratio $c/a \approx 1.07$ [84]. Although the opposite trend is observed experimentally, the experiments and the theoretical calculation seem to indicate an instability towards a magnetic reorientation that might be affected by the addition of dopants.

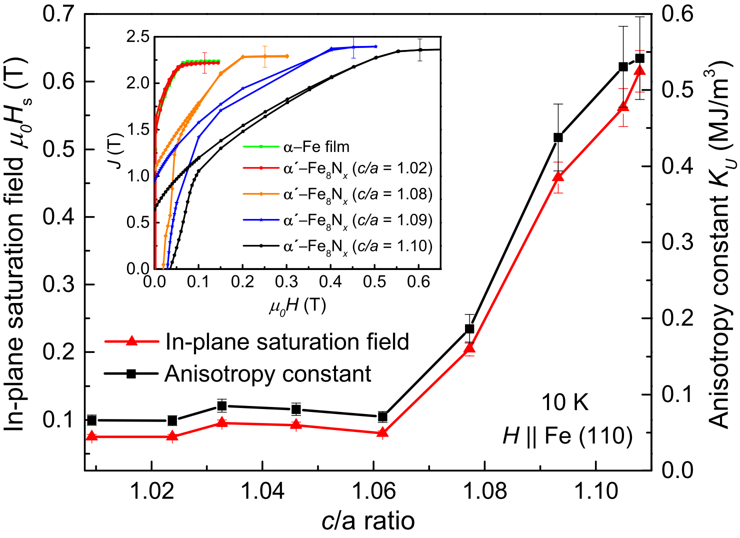

Figure 5.9: Magnetic properties of α'-Fe_8N_x thin films. In-plane saturation field, H_s, and anisotropy constant, K_u, in dependence of the c/a ratio. The inset shows the relevant part of the hysteresis loops.

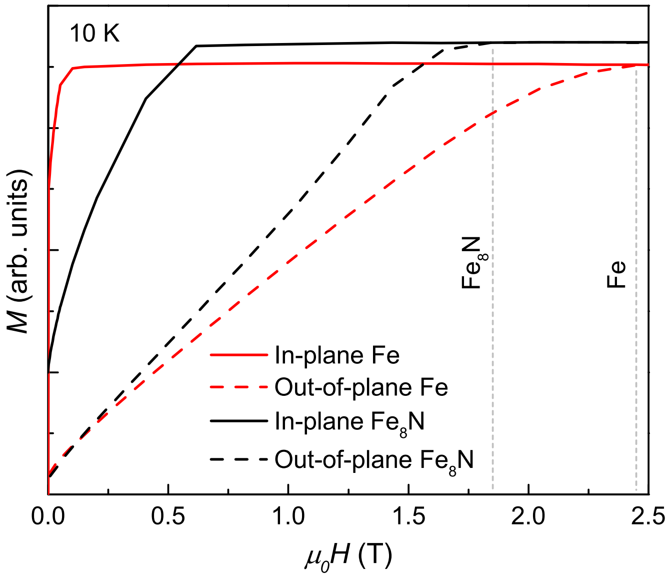

Figure 5.10: In-plane and out-of-plane demagnetization curves for both, α-Fe and α'-Fe_8N thin films.

The uniaxial anisotropy constant was calculated according to Equation 2.7. The measured saturation magnetization, M_s, and the in-plane saturation field, H_s at 10 K, were used in the calculations. As plotted in the inset of Figure 5.9, a continuous enhancement of the in-plane saturation field was observed. This indicates the progressive development of a uniaxial anisotropy component along the out-of-plane (c-axis) direction. The uniaxial anisotropy constant increases with increasing c/a (or resp. nitrogen content) reaching a value of $0.54\,\mathrm{MJ\,m^{-3}}$ for the sample with an in-plane saturation field of $\approx 0.6\,\mathrm{T}$ (see Figure 5.9), in reasonable agreement with previous results [153, 86].

In order to further study the enhanced uniaxial anisotropy contribution resulting from the alloying of the interstitial nitrogen atoms, also out-of-plane $M(H)$ measurements were conducted. The in-plane and out-of-plane demagnetization curves for both, α-Fe and the α'-Fe_8N thin films are shown in Figure 5.10. The results confirm the physical picture previously derived from the analysis of the in-plane saturation field. Even though the H_a seems to be larger for the Fe film (which is due to the deceitful demagnetizing field contribution to the in-plane aniosotropy in thin films), a significant enhancement in perpendicular magnetic anisotropy is manifested by the offset in the intersection of the respective in-plane and out-of-plane demagnetization curves. In comparison to the Fe film, the α'-Fe_8N shows lower out-of-plane and higher in-plane saturation field values, which implies an additional anisotropy contribution perpendicular to the film plane.

The coercivity H_c increases from approximately 2.3 mT for the pure Fe film to 35 mT for α'-Fe_8N (see Figure 5.6). H_c is an extrinsic property governed by microstructure and does not necessarily reflect the intrinsic magnetic anisotropy of the material.

5.3.3 Magnetic domains

Another way for investigating the appearance of perpendicular magnetic anisotropy (PMA) in α'-Fe$_8$N$_x$ thin films is by means of magnetic force microscopy (MFM). MFM is a scanning probe technique, analogical to atomic force microscopy, but operated with a magnetic tip [166]. It is sensitive to the second derivative of the magnetic stray-field gradient or the force gradient $\partial F/\partial z$ and therefore very useful for studying the out-of-plane component of the magnetization. The MFM experiments were conducted by Tim Helbig at TU Darmstadt, Materials Science department, Functional Materials research group.

Magnetic force microscopy images for the α'-Fe$_8$N$_x$ thin film series are shown in Figure 5.11. The measurements have been done in a demagnetized state and zero field, at room temperature. The results confirm the physical picture presented in the previous section. The samples with small c/a values, $c/a < 1.05$, and low K_u (according to Figure 5.9) show no distinguishable magnetic signal (left side of the Figure 5.11), indicating that the magnetization direction lies fully in-plane. The modulation of the signal simply reflects the topology of the surface having a roughness of about 2.3 nm. Whereas samples with large c/a ratio ($c/a \geq 1.06$) and thus enhanced K_u show a clear, stripe-like domain pattern (right side in the Figure 5.11) signaling a strong out-of-plane component of the magnetization vector. The pattern is typical to uniaxial thin films [167].

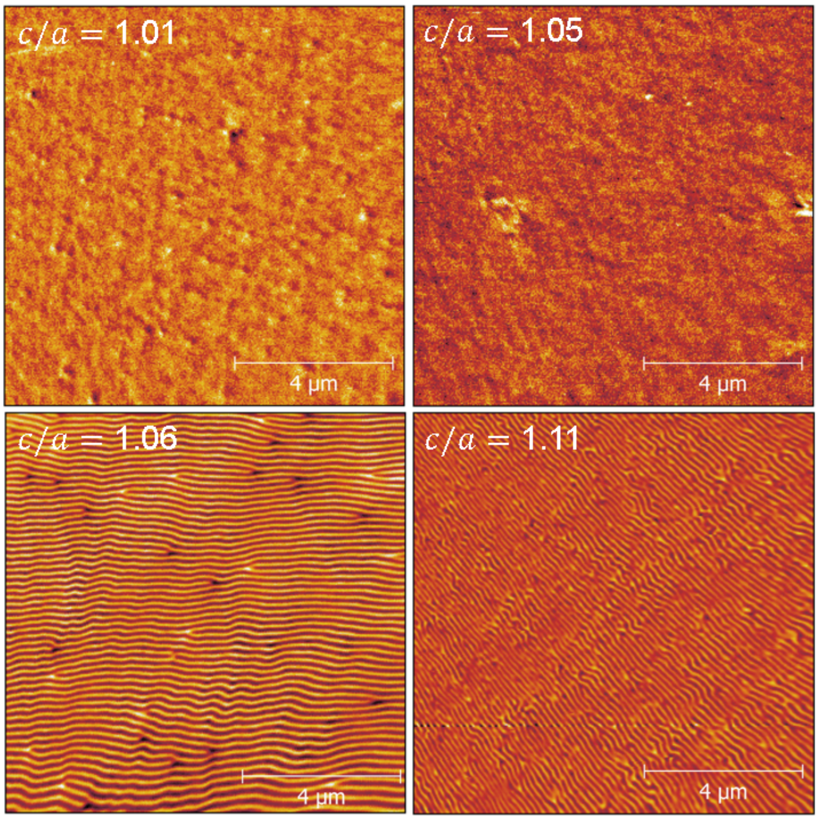

Figure 5.11: MFM results of the α'-Fe$_8$N$_x$ thin films with different degree of tetragonality. Above $c/a \approx 1.05$ stripe domain pattern develops, indicating an out-of-plane component of the magnetization.

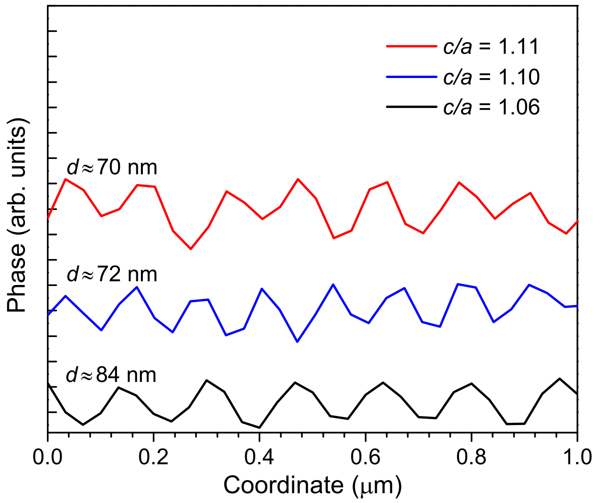

Figure 5.12: MFM line scans taken perpendicular to the stripe domain walls for α'-Fe$_8$N$_x$ thin film samples with three different c/a.

As already mentioned, due to the demagnetizing factor $N_d = 1$ and the resultant demagnetizing field $H_d = -M$ in thin films, the magnetization would prefer to lie within the film plane. However, in case of a material with uniaxial magnetocrystalline anisotropy with the easy axis oriented out-of-plane a perpendicular magnetization (normal to the film plane) can be stabilized if [73]

$$K_u > \frac{\mu_0 M_s^2}{2}. \tag{5.1}$$

This corresponds to a single-domain state with the respective magnetostatic energy density

$$E_{ms} = \frac{\mu_0 M_s^2}{2}. \tag{5.2}$$

Considering the first sample in the α'-Fe$_8$N$_x$ thin film series which shows magnetic domain pattern ($c/a \approx 1.06$ in Figure 5.11), Equation 5.1 gives a $K_u = 1.95\,\mathrm{MJ\,m^{-3}}$. According to Figure 5.9, the actual uniaxial anisotropy constant for the sample is much smaller. In reality, the MFM measurements have been done on samples in a demagnetized state and therefore the magnetostatic energy is reduced due to the formation of the domains. Stripe domains is a nature's solution for minimizing both, the anisotropy and magnetostatic energy. The total energy in this case is given by the sum of the magnetostatic, anisotropy and exchange energies which results in the following condition for the appearance of stripe domains [168]:

$$K_u > \frac{3M_s}{2}\sqrt[3]{\frac{AM_s}{8\pi^2\mu_0^2 t}} \tag{5.3}$$

with t being the film thickness, A the exchange stiffness constant and M_s the saturation magnetization. For the same sample under consideration, this would lead to $K_u \approx 0.1\,\mathrm{MJ\,m^{-3}}$. The K_u value for this sample measured as described in the previous section is $0.07\,\mathrm{MJ\,m^{-3}}$. As the exchange stiffness parameter for the specific α'-Fe_8N_x samples is not known, the initial α-Fe value of $8.3\,\mathrm{pJ\,m^{-1}}$ [169] has been used in the calculations. Considering this as well as the error bar for the K_u measurements, both values are in a good agreement. By comparing the values obtained from Equations 5.1 and 5.3 it is obvious that the formation of domains has significantly reduced the magnetostatic energy of the thin film.

Line profiles taken along the direction normal to the stripe domain walls on the MFM images in Figure 5.11 for three diferent c/a ratios are shown in Figure 5.12. In principle one would expect the domain wall width δ_w to decrease with the enhanced anisotropy K_u (proportional to $\sqrt{A/K_u}$) and the domain width δ to increase (proportional to $\sqrt{AK_u}$). However a slightly decreasing wavelength trend is observed in the experiments. The statistical error in the domain width estimation is close to 7 %. The MFM resolution available here was not enough to accurately measure the domain wall width. The extracted wavelength shown in Figure 5.12 is a sum of the domain and domain wall widths, therefore a deviation could also be caused by the corresponding changes in the domain wall width accounting for the observed decreasing trend. Also the differences in film thickness as well as the changes in the exchange stiffness A values make a proper physical interpretation of these results difficult.

5.4 Chemical composition and electronic structure

In order to study the chemical composition (for example oxidation or any impurities which could influence the observed magnetic properties) as well as the possible hybridization effects originating from the presence of N, XPS measurements have been performed on the series of the α-Fe and α'-Fe_8N_x thin films.

Initially, all of the XPS survey spectra show signals from Fe, N, O, Ta and C. The last samples in the α'-Fe_8N_x series (with high c/a values) also show small presence of Cu, as already mentioned before. C and O intensities mainly come from the surface contamination due to the exposure to ambient atmosphere. This is proven by a rapid intensity drop after Ar ion etching. A survey spectra of an α' sample with $c/a = 1.11$ after 15 min of Ar^+ ion sputtering at 1 keV is shown in Figure 5.13. In addition to Fe and N, also weak signals from Ar, O and Cu were detected.

Ar is most probably incorporated during the ion etching. Ar incorporation during the initial film deposition process can not be completely ruled out, as a minor shift in the Fe (200) reflection was observed already without adding nitrogen to the plasma (see Figure 5.2). Cu signal is caused by thinning down of the target during the deposition, thus exposing the surface of the sputtering gun (made of copper) slightly. Consequently, a small amount of Cu onto which the Fe target was bonded, was incorporated into these last samples. In principle, Cu and Fe are immiscible and do not form binary compounds [170]. One could expect that Cu atoms are not being incorporated in α'-Fe_8N_x, but form Cu precipitates and therefore do not alter the magnetic properties of the α' (apart from a reduction in magnetization due to the additional nonmagnetic phase). However, as sputtering is a non-equilibrium process, also alloying

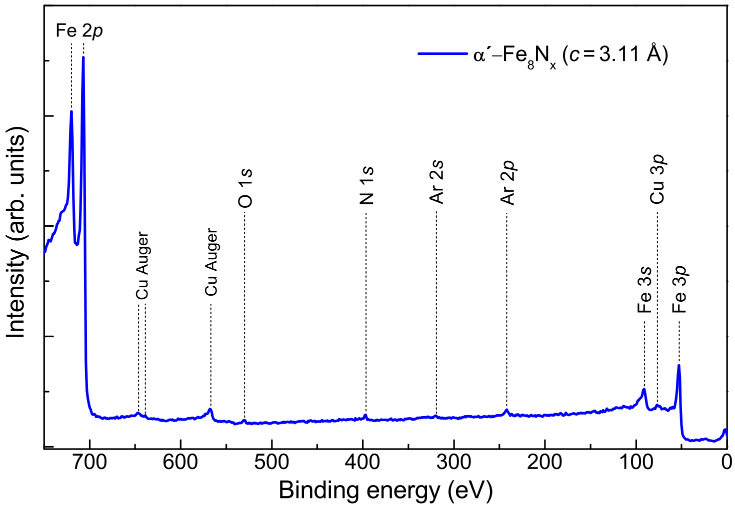

Figure 5.13: XPS survey spectra on an α'-Fe$_8$N sample after Ar$^+$ ion sputtering for 15 min. In addition to Fe and N, small traces from O, Ar, Cu are detected.

of Cu in Fe is possible [171]. High-resolution TEM investigations would be necessary in order to clarify this.

The increased magnetic moment can be interpreted within a Stoner analysis as a result of the changes in band structure solely due to the lattice expansion [75]. Chemical effects due to hybridization originating from the presence of the interstitial N atoms could be competing with the magnetovolume effect [172]. In order to approach this issue, XPS has been performed on a series of α-Fe and α'-Fe$_8$N$_x$ thin films at the Fe 2p energy.

The results are shown in Figure 5.14. XPS is very sensitive to different types of bonding and changes in the electronic structure. For example, a change in the oxidation state of Fe, as for iron oxides, would be immediately recognizable in the corresponding shifts in the binding energies [137]. In the case of the α'-Fe$_8$N$_x$ series, the Fe 2p spectra of all the samples cannot be distinguished from each other and always show a text-book like Fe 2p spectrum. This indicates that the bonding and hybridization only weakly change during nitrogen incorporation. Only the bond lengths are changed, which is not expected to lead to a measurable shift of the XPS positions. The inset of Figure 5.14 compares the valence band spectra for a pure α-Fe thin film and an α'-Fe$_8$N$_x$ thin film. Again, there is no substantial difference, indicating that there is no significant change in the spin-integrated electronic structure. A low-intensity feature around 6.5 eV–9.5 eV can probably be attributed to N 2p states, following the interpretation of γ'-Fe$_4$N presented in the foregoing chapter. These observations support the claim that the increased magnetic moment per Fe atom in α'-Fe$_8$N$_x$ is a magnetovolume effect where nitrogen interstitial atoms play the role of stabilizing the expanded α-Fe crystal lattice.

The findings are consistent with the poor thermal stability in α'-Fe$_8$N$_x$. No significant charge transfer, i.e. chemical bonding between Fe and N occurs. The α'-Fe$_8$N$_x$ structure is existing in a metastable, local energy minima.

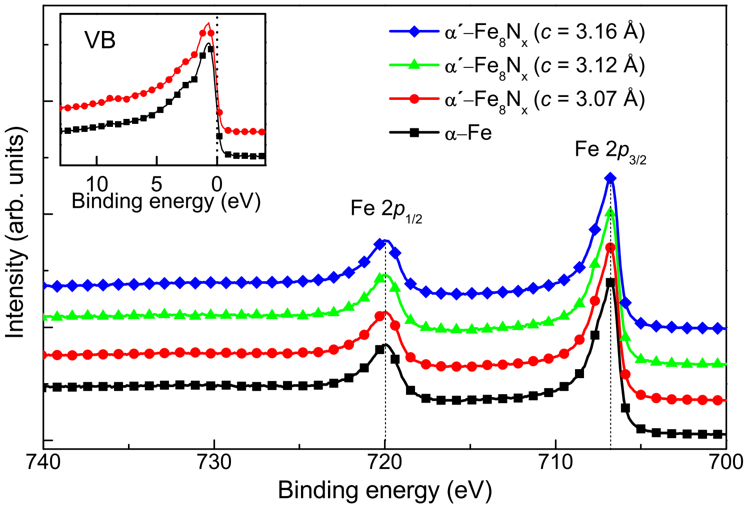

Figure 5.14: XPS spectra at the Fe $2p$ position of α-Fe and α'-Fe$_8$N$_x$ thin films (every 9th data point shown). The inset shows the corresponding valence band spectra (every 7th data point shown).

5.5 A theoretical model for the development of magnetic anisotropy

Two main features observed in the magnetic properties of α'-Fe$_8$N$_x$ are that the magnetic moment scales with the bct unit cell expansion which is also accompanied by an enhanced uniaxial magnetocrystalline anisotropy. To shed light on the physical origins of the experimentally observed phenomena, detailed theoretical models should be provided. As already mentioned in Chapter 2, there are several fundamental questions concerning the magnetic properties of the α'-Fe$_8$N$_x$ which still require clarification. They are:

- Is the tetragonal unit cell expansion present in α'-Fe$_8$N$_x$ also leading to the same enhanced magnetic moment phenomena as an isotropic magnetovolume effect in α-Fe?
- Do the N atoms in α'-Fe$_8$N$_x$ only serve to stabilize the strain in bct Fe or also contribute to the magnetic moment?
- Are the interstitial N atoms crucial for stabilizing uniaxial magnetocrystalline anisotropy in α'-Fe$_8$N$_x$ or is it solely an effect of the lowering of the symmetry?

In order to explore these questions in more detail, density functional theory (DFT) calculations are required. This section presents the results from the DFT calculations done in collaboration with Jun. Prof. H. Zhang, Theory of Magnetic Materials research group at TU Darmstadt. The calculations have been performed for the in previous sections described α'-Fe$_8$N$_x$ sample series, i.e. using the experimental lattice parameters as an input in order to have the best comparison with the experimental results.

The results presented in this section have been published in Ref. [32]. All the details about the calculation procedure can be found there.

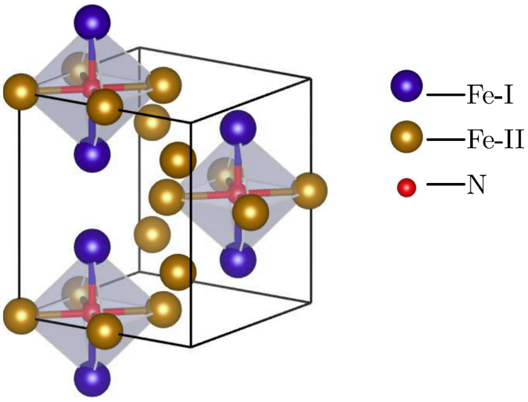

Figure 5.15: Schematic illustration of the unit cell geometry configuration used for the calculations (adapted from Ref. [32]).

A schematic illustration of the unit cell geometry configuration showing the Fe octahedra is given in Figure 5.15. Here the N atoms occupy specific interstitial sites, according to the lattice relaxation calculations.

The results are summarized in Figure 5.16. In agreement with the experimental findings, the average magnetic moment per Fe atom obtained from DFT calculations is also increasing with the unit cell expansion (the red curve) and reaches $\approx 2.44\,\mu_B$. The above result for virtually tetragonalized α-Fe was compared to α'-Fe_8N_x taking into account the presence of interstitial N atoms and a similar trend was observed (not shown here) with the average magnetic moment per Fe atom reaching $\approx 2.40\,\mu_B$. This shows that the nitrogen atoms in α'-Fe_8N_x serve to stabilize the strain in bct Fe, but do not significantly contribute to the magnetic moment. The marginally reduced moment in the latter case could be attributed to a hybridization of Fe 3d states with N valence states [173, 117] or interaction between N 2p and Fe 4s orbitals [174]. The calculated magnetic moment is slightly lower than the experimentally measured one, but, as already discussed earlier, there are many aspects which could introduce errors in the experimental data. The values obtained from the actually measured, instead of calculated a, b lattice parameters (see Figure 5.7) are in a very good agreement with the DFT predictions.

More complex picture is evolves when it comes to the magnetic anisotropy. As already mentioned in Chapter 2, calculations for tetragonally (bct) distorted Fe done by Burkert et al. [84] have shown that an easy axis reorientation from [001] to [100] occurs at a ratio $c/a \approx 1.07$. Based on these results, α'-Fe_8N_x should exhibit a strongly negative anisotropy energy corresponding to the easy direction of the magnetization within the basal plane at large c/a. Thus, the PMA observed experimentally in the α'-Fe_8N_x samples can no longer be explained by the tetragonal distortions only.

The calculated MAE values for α'-Fe_8N_x and virtually tetragonalized α-Fe (with identical lattice constants, but without interstitial N), are shown in Figure 5.16. Indeed there is a spin re-orientation transition occurring in bct strained Fe (the blue curve) and all the α'-Fe_8N_x samples which showed a development of PMA from the magnetic measurements, actually would lie in the planar anisotropy c/a region here. This shows that the tetragonal distortions alone are not sufficient for stabilizing the PMA in bct Fe.

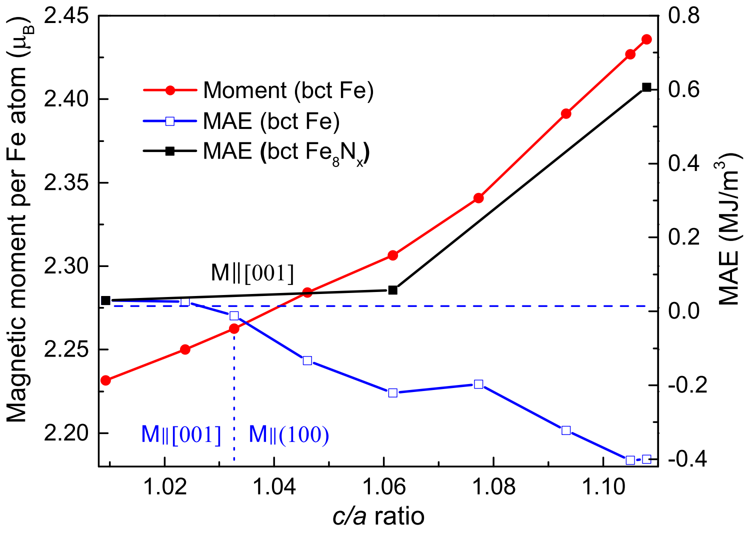

Figure 5.16: Calculated magnetic moments par Fe atom as well as MAE for virtually tetragonalized Fe, Fe_8N_0, $Fe_8N_{0.5}$, and Fe_8N_1. Negative MAE corresponds to easy-plane anisotropy. The straight lines are guides for the eyes (adapted from Ref. [32]).

The situation changes remarkably when interstitial N atoms are introduced into the system (the black curve). A sample in the middle of the α'-Fe_8N_x series, namely a $Fe_8N_{0.5}$ shows a slightly enhanced (to about 0.057 MJ m^{-3}) easy-axis (along the [001] direction) anisotropy. At the end of the series, for Fe_8N_1 composition, a significant MAE develops with about 0.6 MJ m^{-3} which is very close to the experimental value of 0.54 MJ m^{-3}. Thus the interstital N atoms play a crucial role in stabilizing and enhancing the uniaxial magnetocrystalline anisotropy in α'-Fe_8N_x.

According to Bruno [175], the MAE is proportional to the variation in orbital moments along the different magnetization directions, $\Delta\mu_L$, and the strength of atomic spin-orbit coupling ξ:

$$MAE = \frac{\xi}{4}\Delta\mu_L. \tag{5.4}$$

Moreover, the spontaneous magnetization would be oriented along the direction with the largest orbital moments. In order to apply this to the present problem, the orbital moments on both Fe atomic sites as shown in Figure 5.15 for $Fe_8N_{0.5}$ and Fe_8N_1 cases were calculated and are summarized in Table 5.3. The results show that in the case for α'-Fe_8N_x the difference of total orbital moments of Fe atoms for magnetization along [001] and [100] directions is indeed significant, about 0.108 μ_B. For $Fe_8N_{0.5}$, the difference of the total orbital moments of Fe atoms for magnetization along [001] and [100] directions is one order of magnitude smaller, about 0.012 μ_B. This clearly explains the greatly enhanced MAE in Fe_8N.

Very interesting findings can also be seen in the atom-resolved contributions. The type-I Fe atoms clearly dominate the MAE enhancement whereas the type-II Fe atoms turn out to be even detrimental to the perpendicular anisotropy. This is in agreement with the results from Ke et al. [101] for the ordered α''-$Fe_{16}N_2$ phase (see Chapter 2). Authors show that the largest (and positive) contribution to the MAE

Table 5.3: Orbital moments (in μ_B) for Fe-I and Fe-II atoms (according to Figure 5.15) in α'-Fe_8N_x. The numbers in parenthesis stand for the multiplicity of the respective Fe atoms and superscripts for the magnetization direction (from Ref. [32]).

	Fe-I$^{[001]}$	Fe-I$^{[100]}$	Fe-I $\Delta\mu_L$	Fe-II$^{[001]}$	Fe-II$^{[100]}$	Fe-II $\Delta\mu_L$	total $\Delta\mu_L$
$Fe_8N_{0.5}$	0.05455	0.03875	0.0158 (×2)	0.05548	0.05688	-0.0014 (×14)	0.00075 (×16)
Fe_8N	0.07254	0.04296	0.02958 (×4)	0.05719	0.05806	-0.0009 (×14)	0.00675 (×16)

with the energy minimum corresponding to the [001] crystallographic direction comes from the Fe $4e$ crystallographic site, which is equivalent to the type-I Fe atoms in the α'-Fe_8N_x model described here.

5.6 Annealing studies

So far, only the primary, disordered α'-Fe_8N_x martensite was considered. The secondary, ordered α''-$Fe_{16}N_2$ phase possibly shows magnetic properties (M_s and K_u) superior to those of the α' martensite, as already mentioned in Chapter 2. Originally, the α'' was produced by a low temperature (393 K) heat treatment of the martensite powders [47]. Also, more recent works in thin films show that the secondary, ordered α''-$Fe_{16}N_2$ phase can be formed by a low temperature annealing of the α' martensite [89, 102, 90].

The same works report a significant increase in M_s after the tempering, which is attributed to an N atom ordering effect. If this is indeed the case, an additional external magnetic field during the heat treatment step should lower the free energy for the α'' and thus be beneficial. Also considering the uniaxial MAE, an external magnetic field parallel to the c-axis during the heat treatment should provide an additional driving force for the orientational precipitation.

The effect of an external magnetic field on the formation of α''-$Fe_{16}N_2$ has been investigated by many researchers [176, 177, 178, 179]. It should enhance the transformation from α' to α'' and favor c-axis alignment parallel to the magnetic field direction. Therefore, this approach was chosen in the present work. In case of the previously described α'-Fe_8N_x thin film samples, the magnetic field has to be applied normal to the film plane in order to form α''-$Fe_{16}N_2$ with c-axis out of the film plane. Hence, two approaches were chosen for the annealing studies:

- A low-temperature post-annealing with heating the samples under vacuum conditions
- Post-annealing in an external magnetic field perpendicular to the film plane (parallel to the crystallographic c-axis).

The results are summarized in Figure 5.17. Annealing at 373 K for 10 h does not alter the XRD pattern significantly. As next, annealing with magnetic field of 5 T parallel to the c-axis direction for 30 h was done in order to see if there are any changes detectable in the XRD. The α' (002) (overlaps with α'' (004)) reflection seems to become slightly more pronounced and positioned according to the theoretical Bragg angle of 58.66°. However, no superlattice reflections appear. In the case of formation of a detectable amount of α'', a peak at 28.36° corresponding to α'' (002) reflection should appear. As this is not the case,

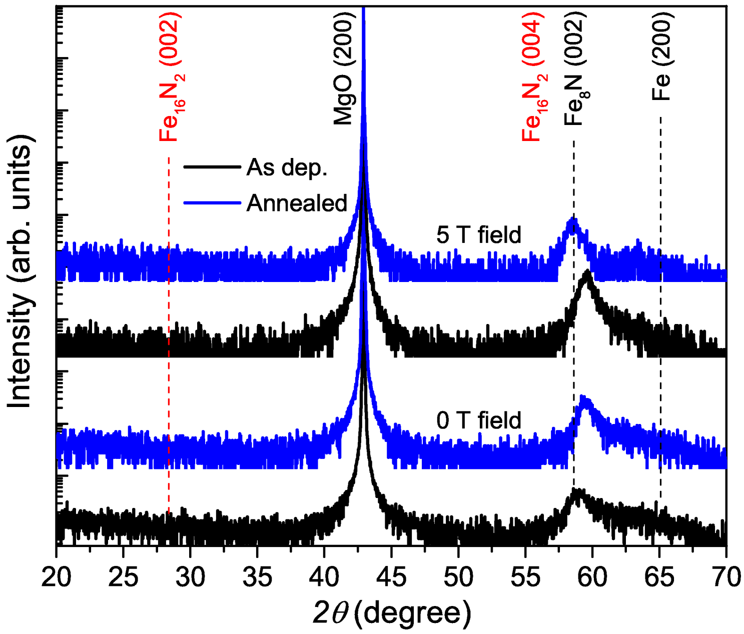

Figure 5.17: Annealing studies on α'-Fe$_8$N$_x$ samples with and without external magnetic field.

it is concluded that the post-annealing of the current α' films, both without and with external magnetic field, does not lead to discernible precipitation of the ordered α'' phase. Consequently, no investigations of the N site ordering influence on the magnetic properties of α'-Fe$_8$N$_x$/α''-Fe$_{16}$N$_2$ could be conducted. The reason could be the substrate-film lattice mismatch. In literature, a Fe (001) underlayer on GaAs [102] and MgO [180] substrates as well as InGaAs [89, 90] substrates have been used, providing more exact fitting on the atomic scale for coherent formation of α''-Fe$_{16}$N$_2$ than the buffer-free MgO (001) used in this work. In addition, the overall low XRD intensities evident in Figure 5.17 show that, considering the theoretical $I^{cal}(002)/I^{cal}(004)$ ratio, even if a partial ordering was present in the samples, the low-intensity α'' (004) reflection is not likely to exceed the background signal.

5.7 Summary and conclusions

α'-Fe$_8$N$_x$ thin films in the full range of $0 \leq x \leq 1$ have been sucesfully fabricated by RF magnetron sputtering onto MgO (001) substrates. The nitrogen incorporation led to a gradually increased c-axis lattice parameter and tetragonality of the compounds.

The average magnetic moment per iron was found to scale with the lattice expansion. This result demonstrates that the origin of the increased magnetic moment is solely the lattice expansion, which is in agreement with several theoretical calculations.

Along with the increase in magnetization comes an increase in magnetocrystalline anisotropy.

The occurrence of the enhanced uniaxial magnetic anisotropy with increasing concentration of N atoms in α'-Fe$_8$N$_x$ was explained, by combining experimental and theoretical studies. The results show that the tetragonal unit cell expansion in α-Fe results in an increased magnetic moment, but is not sufficient to stabilize the PMA. Here the interstitial N atoms play a decisive role. A significant uniaxial anisotropy develops due to the anisotropy in orbital moments along different crystallographic directions in the Fe atoms directly above and below N.

Post-annealing of the α' thin films without and with external magnetic field did not lead to discernible formation of the ordered α'' phase. This stands in contrast to reports in the literature.

6 Synthesis and characterization of α''-Fe$_{16}$N$_2$ nanoparticles

For multiple possible α''-Fe$_{16}$N$_2$ applications phase-pure and well dispersed nanoparticles are beneficial. For example, in hard magnetic materials the coercivity (nucleation field) is maximum for single-domain particles [181]. Hence, realizing a fine microstructure is crucial for translating the intrinsic anisotropy field H_a into the extrinsic coercivity H_c. Furthermore, magnetic hyperthermia requires superparamagnetic particles in order to avoid agglomeration due to the magnetic interactions [182]. Therefore, this chapter is dedicated to synthesis and characterization of α''-Fe$_{16}$N$_2$ nanoparticles.

Phase-pure α''-Fe$_{16}$N$_2$ nanoparticles are synthesized via a two-step route. Commercial γ-Fe$_2$O$_3$ nanoparticles are used as a precursor and reduced to α-Fe in a hydrogen atmosphere. In the second step, hydrogen-reduced α-Fe nanoparticles are subsequently nitrogenated in an ammonia flow. An attempt to minimize the detrimental particle coarsening during the reduction step by increasing hydrogen and reducing water vapor partial pressure in the reaction zone is presented. For detailed synthesis procedure the reader is referred to Chapter 3.

Crystal structure, particle morphology, phase stability, chemical composition and magnetic properties are investigated. Majority of the results presented in this chapter have been published in Ref. [33].

6.1 Reduction of Fe$_2$O$_3$ nanoparticles by hydrogen

The initial γ-Fe$_2$O$_3$ nanoparticles is a typical brown rust-like powder. The average particle size (APS) is 20 nm–40 nm (manufacturers data sheet). In order to validate it, both microscopy and XRD were performed. The corresponding SEM and TEM images are presented in Figure 6.1. Visually, particles show a broad size distribution from barely distinguishable fine nanoparticles to particles in the range of hundreds of nanometers. The average crystallite size obtained from XRD peak brodening was 55 nm ± 5 nm. This shows that there is a discrepancy with the manufacturer's data.

In the first step, the γ-Fe$_2$O$_3$ nanoparticles were reduced to α-Fe in a hydrogen atmosphere. Different reaction conditions (temperature, time, hydrogen pressure, presence of a water binding agent) were varied. As already stated in the introduction, the aim was to avoid particle growth as much as possible, therefore the hydrogen reduction step was optimized towards lowering the reaction time and temperature.

Widenmeyer et al. [116] were able to reduce the reduction temperature to 663 K (for 3 h), therefore this was chosen as a starting point. Then, the hydrogen pressure was gradually increased with lowering the reaction temperature. Figure 6.2 shows the XRD patterns of the initial γ-Fe$_2$O$_3$ and the same

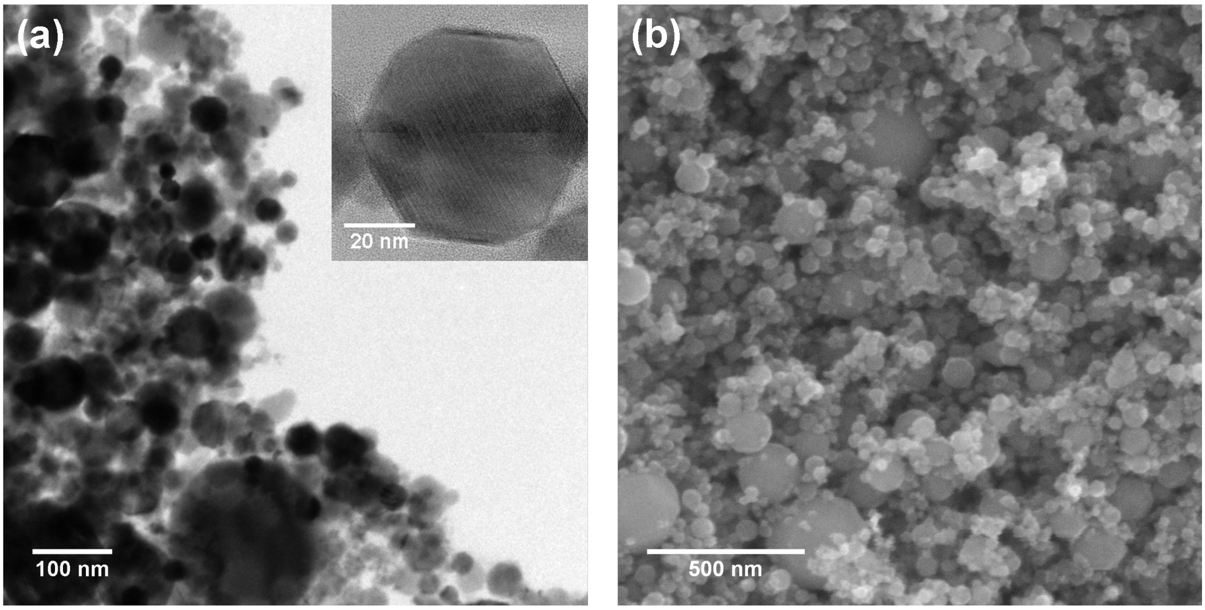

Figure 6.1: TEM (a) and SEM (b) images of the initial γ-Fe_2O_3 nanoparticles.

nanoparticles reduced at a hydrogen pressure of 10 MPa for 3 h at various temperatures. Down to 543 K the reaction could be completed within 3 h, whereas further lowering of the temperature lead to only partial reduction and residual γ-Fe_2O_3 in the sample.

In order to lower the temperature even more, the hydrogen pressure was further raised. The corresponding XRD results are presented in Figure 6.3. At a pressure of 30 MPa the γ-Fe_2O_3 nanoparticles were fully reduced; only reflections from α-Fe are visible in the corresponding diffractogram. At 503 K-30 MPa, at 493 K-40 MPa and at 483 K a hydrogen pressure of 53 MPa had to be applied for a complete reduction within 3 h. Otherwise a mixture of γ-Fe_2O_3 and α-Fe was evident in the XRD data. The pressure of 53 MPa was the limit for the experimental autoclave, but a further decrease in the reduction temperature for even higher pressures can be expected.

The pressure-temperature graph for a complete reduction within 3 h is shown in Figure 6.4. Starting from 663 K at ambient pressure, the temperature is continuously lowered down to 483 K at 53 MPa. Even though slightly saturating, the curve is not flat at the end of the series, which indicates that an extrapolation to higher pressures would indeed enable a further temperature reduction.

As mentioned earlier, the second option for shifting the chemical equilibria of Reaction 3.1 to the right is by reducing the partial pressure of water vapor. This has been realized by adding various water binding agents into the reaction zone. Three different compounds with highly exergonic reactions with water were chosen according to the thermochemical data: Ca, $CaCl_2$ and CaO (pure Ca metal showed the best results). As shown in Figure 6.5 the time necessary for a complete reaction could be shortened significantly (roughly from 3 h to 1 h) with the additional Ca. However, no further lowering of the temperature could be achieved, only facilitating the reaction kinetics. Catalysts enhance the rate at which the chemical equilibrium is established but do not affect its position.

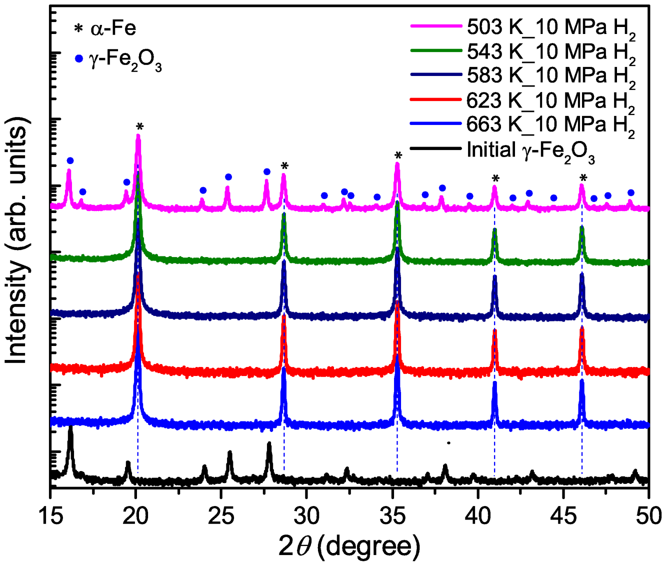

Figure 6.2: XRD patterns for initial γ-Fe$_2$O$_3$ and at different temperatures, for $3\,\mathrm{h}$ hydrogen reduced nanoparticles. At a hydrogen pressure of $10\,\mathrm{MPa}$ the γ-Fe$_2$O$_3$ nanoparticles could be completely reduced to α-Fe at temperatures as low as $543\,\mathrm{K}$. All the diffractograms presented in this chapter have been collected using Mo K_{α_1}-radiation (λ=0.70930 Å) and are presented on a logarithmic scale.

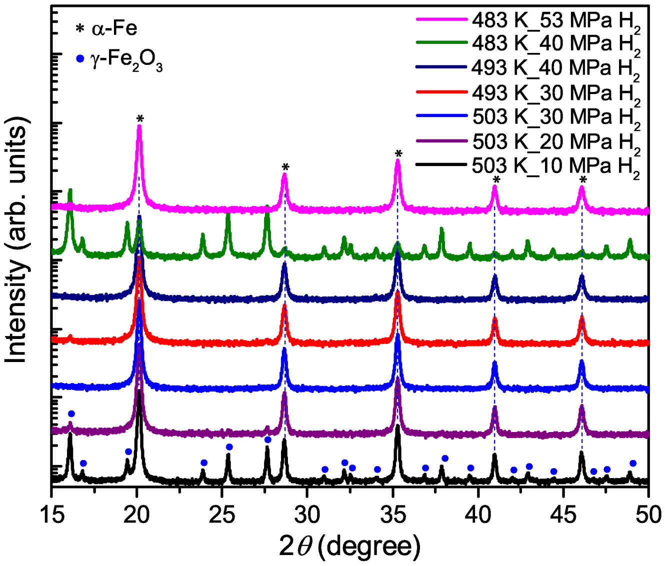

Figure 6.3: XRD patterns for at different temperatures and pressures for 3 hours hydrogen reduced γ-Fe$_2$O$_3$ nanoparticles. Gradual increase in hydrogen pressure enables reducing the reaction temperature. At a hydrogen pressure of $53\,\mathrm{MPa}$ the γ-Fe$_2$O$_3$ nanoparticles could be completely reduced to α-Fe at temperatures as low as $483\,\mathrm{K}$.

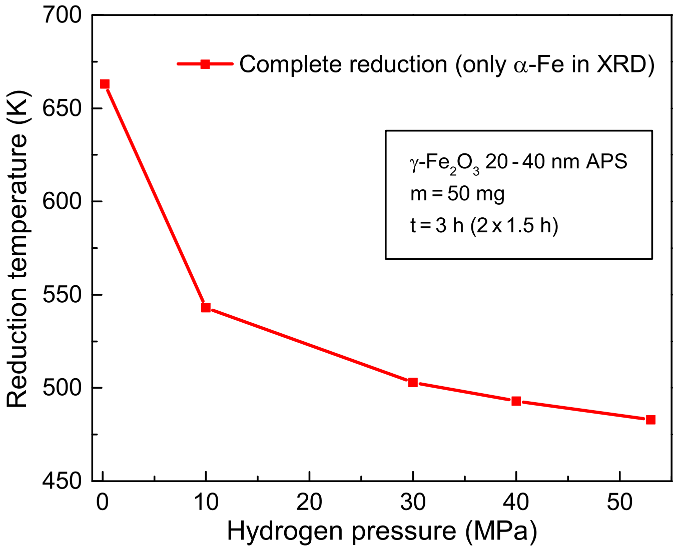

Figure 6.4: Gradual increase in hydrogen pressure enables lowering of the reaction temperature. At a hydrogen pressure of 53 MPa the γ-Fe_2O_3 nanoparticles could be completely reduced to α-Fe at temperatures as low as 483 K.

To summarize, the above presented results demonstrate that by increasing the hydrogen pressure from atmospheric to 53 MPa, it was possible to reduce the temperature necessary for a complete reduction of γ-Fe_2O_3 nanoparticles to α-Fe within 3 h from 663 K down to 483 K.

At this point of the study the principal question to answer is whether or not the above described lowering of the hydrogen reduction step temperature is also beneficial for avoiding particle sintering and growth. In order to address this, SEM investigations on free-standing nanoparticle samples reduced at different temperatures (and hydrogen pressures respectively) were carried out. The results are presented in Figure 6.6. The initial 663 K temperature (Figure 6.6a) leads to severe bonding of the nanoparticles into

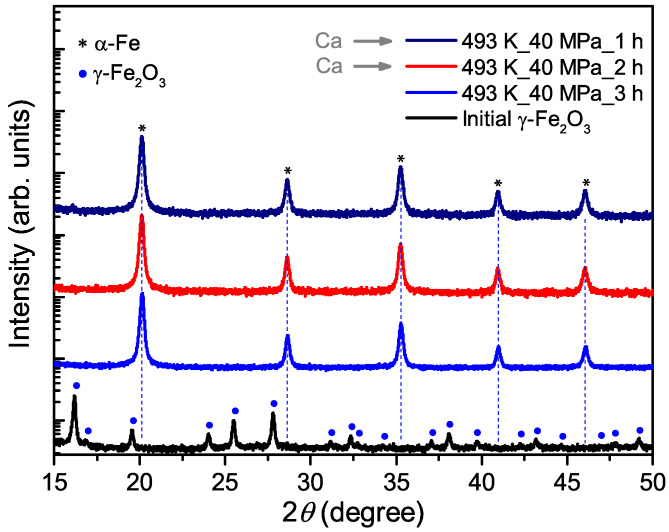

Figure 6.5: By adding pure Ca metal as a water binding agent into the reaction zone, a shortening of the time needed for a complete reduction of γ-Fe_2O_3 could be achieved.

solid structures and surface area loss. Visible neck formation and coalescence are apparent also for the sample reduced at 583 K (Figure 6.6b) and even though much less pronounced, particles are still growing at 543 K (Figure 6.6c). After reduction at 483 K (Figure 6.6d) the individual nanoparticles can be well distinguished. In their size as well as aggregation the resultant phase-pure α-Fe particles look almost similar to the starting material. A particle size analysis was conducted by a line interception method. It

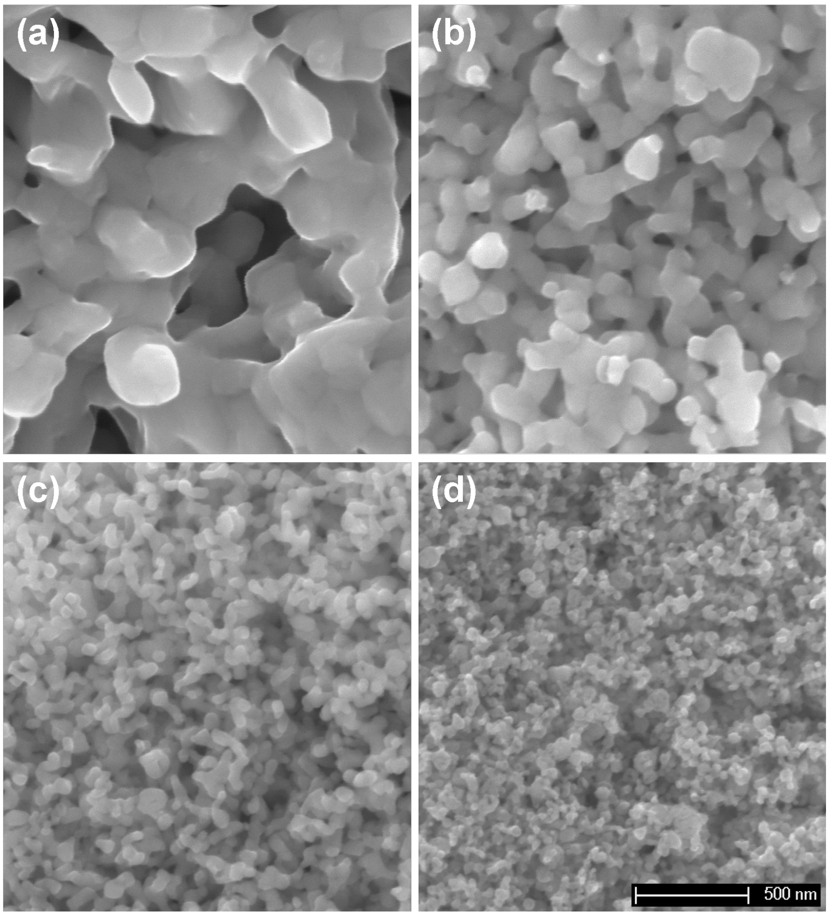

Figure 6.6: SEM images of the hydrogen reduced nanoparticles. (a) 663 K, (b) 583 K, (c) 543 K, (d) 483 K). Lowering of the reduction temperature clearly hinders the particle growth and as a result much finer nanoparticles can be obtained.

Table 6.1: From SEM (XRD) obtained particle (crystallite) size for at different temperatures and hydrogen pressures reduced nanoparticles as shown in Figure 6.6.

Temperature (K)	Particle size (nm)	Crystallite size (nm)
663	215 ± 37	263 ± 46
583	96 ± 47	133 ± 12
543	67 ± 2	79 ± 1
483	47 ± 5	41 ± 1

is a technique used for quantification of grain (particle) size in a given micrograph image, counting the number of times it intersects a grain boundary and then taking the ratio, i.e.

$$\mathrm{APS} = \frac{\text{number of intercepts}}{\text{line length}}. \tag{6.1}$$

Here it was chosen to use four such lines (horizontal, vertical and both diagonals) [183] and then taking the average in order to have reasonable statistics. The results as well as comparison with the data obtained by XRD peak broadening are summarized in Table 6.1. Clearly, lowering of the reduction step temperature results in much finer α-Fe particles. Error in the SEM data is caused mainly by insufficient statistics, especially for the case of coarse particles as well as difficulties to actually define a particle for the high temperature samples as evident from the Figure 6.6. In the case of XRD, the crystallite size results are mainly influenced by Lorentzian vs Gaussian peak shape as well as effects from the microstrain.

It can be concluded that reduction of iron oxide nanoparticles at elevated hydrogen pressures and consequently lower temperatures can indeed be used for production of high quality α-Fe nanoparticles without detrimental particle coarsening.

6.2 Synthesis of α''-$Fe_{16}N_2$: nitrogenation of the α-Fe nanoparticles

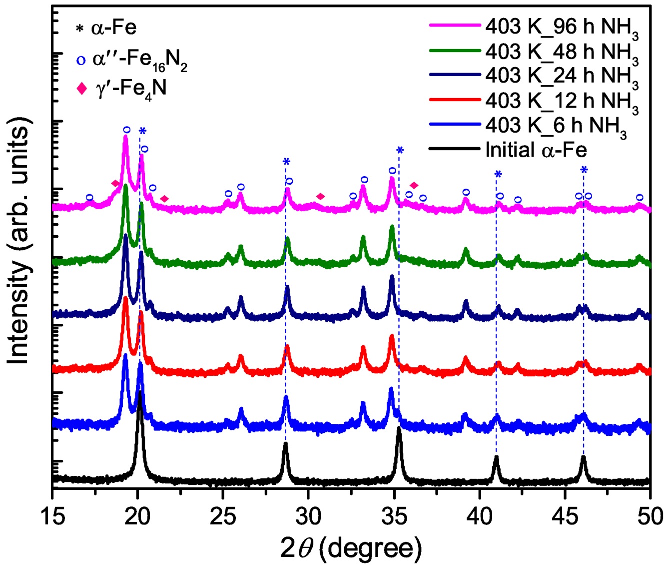

Figure 6.7: XRD patterns for initial α-Fe nanoparticles and those nitrogenated with ammonia at 403 K for different times. Already after 6 h a significant amount of α''-$Fe_{16}N_2$ is formed. Prolonged nitrogenation leads to formation of γ'-Fe_4N.

After the previously described reduction at 53 MPa hydrogen pressure and 483 K for 3 h, the α-Fe nanoparticles were nitrogenated in an ammonia flow. The reaction time and temperature were varied in order to optimize the synthesis of phase-pure α''-$Fe_{16}N_2$ nanoparticles in the shortest possible time and at the lowest temperature, consequently minimizing particle growth.

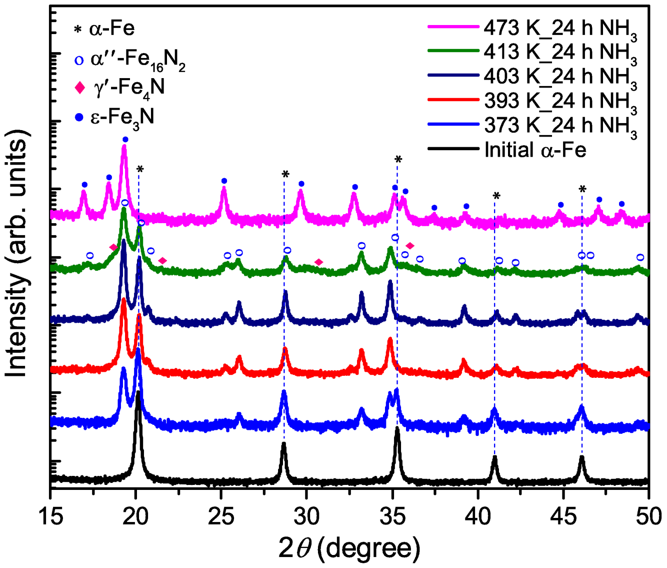

Figure 6.8: XRD patterns for initial α-Fe nanoparticles and those nitrogenated with ammonia at different temperatures for 24 h. At 403 K single-phase α''-$Fe_{16}N_2$ nanoparticles could be successfully synthesized. Lower temperatures result in residual α-Fe, whereas higher temperatures favor the formation of ϵ-Fe_3N.

Reaction times in a range of 6 h–100 h and temperatures in a range of 373 K–473 K were investigated. First, the temperature was kept constant at 403 K and the reaction time was varied. The results are shown in Figure 6.7. The sample consists initially of pure α-Fe and already after 6 h a significant amount of α''-$Fe_{16}N_2$ is formed. Roughly between 12 h–24 h high-purity α''-$Fe_{16}N_2$ was obtained. Extended nitrogenation times lead to formation of γ'-Fe_4N. Based on these findings, 24 h was chosen as the most favorable time and used in further temperature optimization studies.

XRD results of the temperature-dependent experiments are displayed in Figure 6.8. Low nitrogenation temperatures, such as 373 K–393 K, resulted in residual α-Fe. At temperatures above 413 K small signatures of γ'-Fe_4N could be identified, whereas even further temperature increase to 473 K leads to formation of ϵ-Fe_3N. The best results were obtained for samples nitrogenated for 24 h at temperatures around 403 K where phase-pure α''-$Fe_{16}N_2$ samples could be successfully synthesized. The respective XRD measurement as well as the structural analysis (Rietveld method, done using FullProf Suite [143]) results presented in Figure 6.9, show that the nanoparticles contain $\approx 99\,\%$ tetragonal α''-$Fe_{16}N_2$ phase (space group $I4/mmm$) with the corresponding lattice parameters of $c = 6.29\,\text{Å}$ and $a,b = 5.71\,\text{Å}$. This is in good agreement with the reported data for α''-$Fe_{16}N_2$ [47]. A very small presence of γ'-Fe_4N and α-Fe cannot be ruled out, but, if formed, is within the detection limit ($\approx 2\,\%$). The crystallite size extracted from the width of reflections is about 43 nm ± 6 nm. Hence, XRD results suggest that high phase purity, fine α''-$Fe_{16}N_2$ nanoparticles have been successfully synthesized. Due to the overlapping reflections, a contribution from the α'-Fe_8N phase is possible, but as the intensities of the superlattice reflections are reproduced reasonably well by the fit, it should not be in significant amount.

The samples shown in Figure 6.6 were subjected to the above described optimized nitrogenation treatment in order to see if the various morphologies perform differently. Considering the relatively sluggish

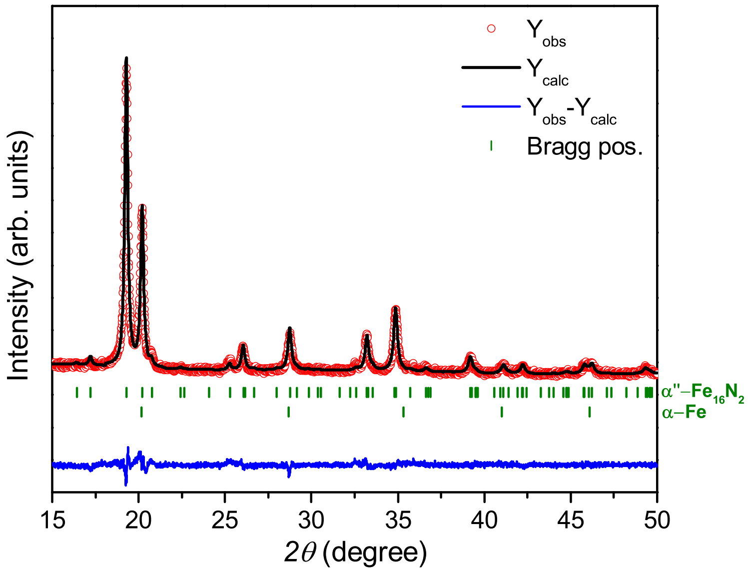

Figure 6.9: Refinement of the XRD pattern of α''-$Fe_{16}N_2$ nanoparticles synthesized at 403 K for 24 h in pure NH_3 flow. The top row of the Bragg markers is for the α''-$Fe_{16}N_2$ majority phase, with a second row shown for α-Fe.

diffusion of N in bcc Fe at such a low temperatures, it is to be expected that for larger particles, core-shell structures (residual Fe core and nitrogenated Fe-N shell) will form.

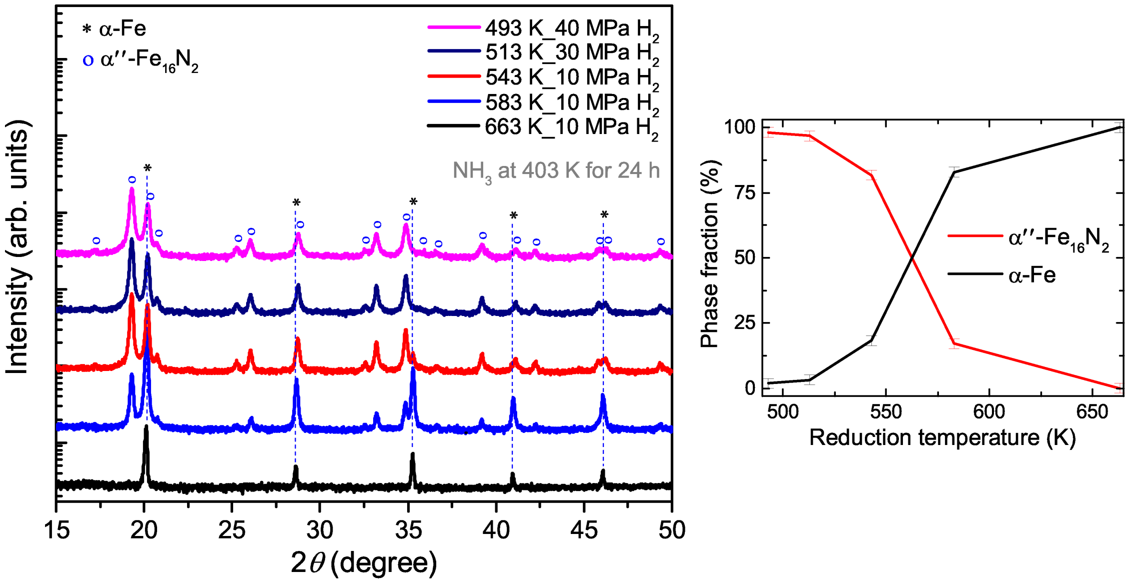

Figure 6.10: XRD patterns for at different temperatures by hydrogen reduced and subsequently nitrogenated nanoparticles. α''-$Fe_{16}N_2$ fraction increases with lowering the reduction temperature (and the resp. particle size).

The hydrogen reduction temperature and the respective particle size indeed has a remarkable impact on the nitrogenation treatment of α-Fe particles. XRD results from experiments performed at different temperatures and pressures, respectively, are summarized in Figure 6.10. As can be seen, only α-Fe peaks are present in the sample reduced at 663 K, where the relatively high temperature causes severe particle sintering and growth (see Figure 6.6a). With lowering the reduction temperature and the particle size (according to Table 6.1), respectively, the residual α-Fe amount decreases whereas the α''-$Fe_{16}N_2$ reflection intensities increase. The corresponding phase fractions are presented in Figure 6.10. Only below 513 K high phase purity α''-$Fe_{16}N_2$ nanoparticles could be synthesized.

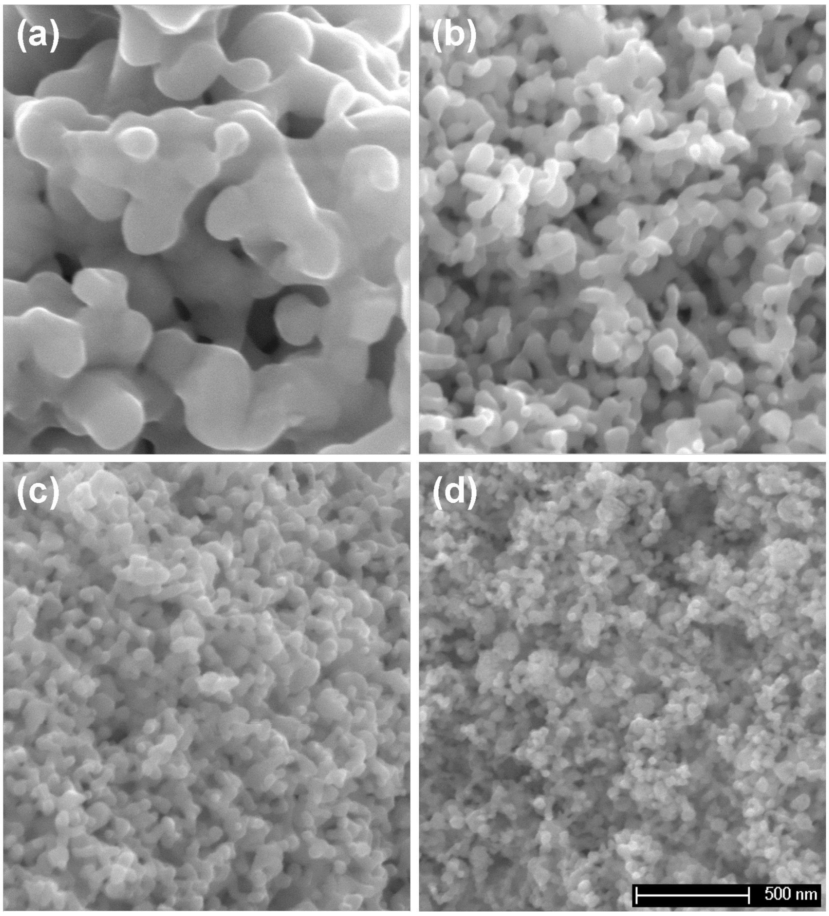

Figure 6.11: SEM images of the hydrogen reduced and subsequently nitrogenated nanoparticles. The resultant particle size and aggregation is comparable to the α-Fe precursor (see Figure 6.6).

SEM images of the nanoparticles reduced at different temperatures, pressures and subsequently nitrogenated are shown in Figure 6.11 (the very same samples shown in Figure 6.6 after subsequent nitrogenation). By comparing to the nanoparticles directly after hydrogen reduction, no significant particle growth during the low temperature nitrogenation step can be observed. The particle size and aggregation are comparable to the α-Fe precursor. The final α''-$Fe_{16}N_2$ nanoparticles (Figure 6.11d) look almost similar to the initial γ-Fe_2O_3. The average particle size is about 47 nm ± 5 nm from SEM image analysis and 41 nm ± 1 nm from XRD peak broadening. The nanoparticles are forming micrometer-range sponge-like agglomerates analogous to what has been reported previously [110].

6.3 Thermal stability of the α''-$Fe_{16}N_2$ nanoparticles

Considering, for example, conventional sintering routes or permanent magnet operating temperatures, it becomes clear that thermal stability is a crucial component when it comes to processing and practical

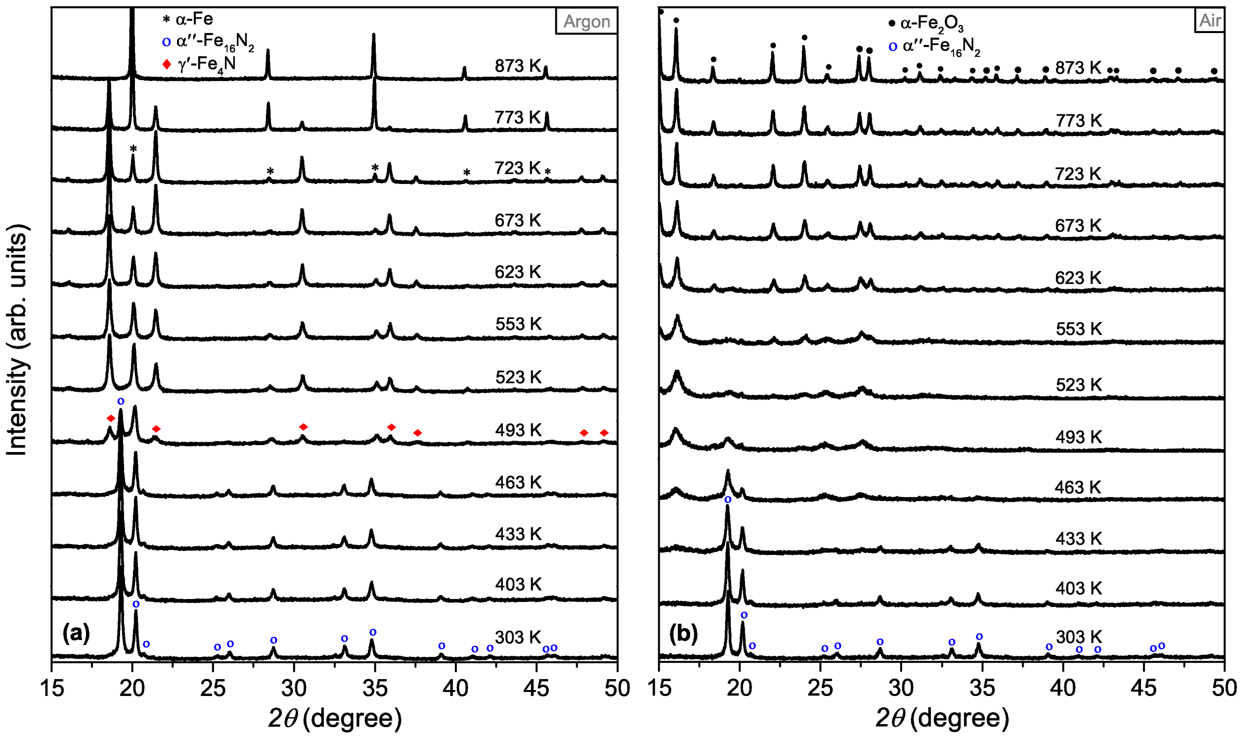

Figure 6.12: Temperature-dependent XRD studies on α''-$Fe_{16}N_2$ nanoparticles in (a) argon and (b) air. In argon atmosphere α''-$Fe_{16}N_2$ phase is stable up to roughly 463 K, whereas in air decomposition begins already at around 433 K.

applications of α''-$Fe_{16}N_2$ nanoparticles. As the phase is metastable and iron oxides are thermodynamically much more stable, the decomposition of α''-$Fe_{16}N_2$ in oxidizing as well as inert gas conditions is investigated. Therefore here temperature-dependent XRD studies, with samples filled into quartz-capillaries, one sealed under argon, and another one left open to allow contact with air, were performed in a temperature range from 303 K to 873 K.

The results are illustrated in Figure 6.12a. α''-$Fe_{16}N_2$ nanoparticles are stable up to roughly 463 K and in the temperature range of 463 K–493 K they start decomposing into α-Fe and γ'-Fe_4N. Further increase in temperature favors formation of γ'-Fe_4N followed by the complete release of nitrogen and transformation into α-Fe at temperatures above 673 K, which is in agreement with previous reports on thin films [30]. The results were also confirmed by DSC measurements (not shown here). After cooling to room temperature, only α-Fe reflections were visible thus confirming the good measurement quality without any indications of sample oxidation.

The same measurement sequence was repeated for the open capillary (Figure 6.12b), thus exposing the sample to air. In this case the α''-$Fe_{16}N_2$ nanoparticles began to oxidize already at around 433 K and gradually completely transformed into α-Fe_2O_3 with further increase in temperature. No intermediate Fe-N or Fe-O phases were observed in the XRD data.

These results reveal the potential difficulties related to practical applications of α''-$Fe_{16}N_2$ nanoparticles, especially if used in reactive atmospheres. For example, Takagi et al. [21] report an attempt to sinter α''-$Fe_{16}N_2$ nanopowder in order to produce a bulk magnet. They show that increasing the sintering temperature enhances densification. However, a temperature of 495 K (222 °C) already lead to decomposition into α-Fe and ϵ-Fe_3N, which was accompanied by reduction in M_s. This confirms the complications regarding production of high quality, fully dense α''-$Fe_{16}N_2$ bulk samples and implies that applications for loose nanoparticles, such as magnetic hyperthermia, are more realistic. Although, if rapidly exposed to ambient atmosphere the nanoparticles burned immediately. A slow, gradual exposure or dispersion in a solvent prohibited this and particles could be further handled in air. This indicates a formation of a Fe-O shell around the particles, protecting them from complete oxidation.

6.4 Magnetic properties of the α''-$Fe_{16}N_2$ nanoparticles

6.4.1 Magnetization

$M(H)$ measurements were carried out using a VSM, operating at ambient atmosphere conditions. Nanoparticles at different process stages were investigated in order to correlate the magnetic properties with structural and morphological features. Samples were prepared in a glovebox as well as ambient conditions for phase stability information, due to the observations made in the previous section. A thin oxidation layer might be left unnoticed in XRD, but because of the much lower saturation magnetization of iron oxides, should be immediately evident in the magnetization measurements.

Hysteresis loops for the initial γ-Fe_2O_3 particles, the, via hydrogen reduction obtained α-Fe and the final, nitrogenated α''-$Fe_{16}N_2$ nanoparticles are shown in Figure 6.13 with the respective magnetic properties summarized in Table 6.2.

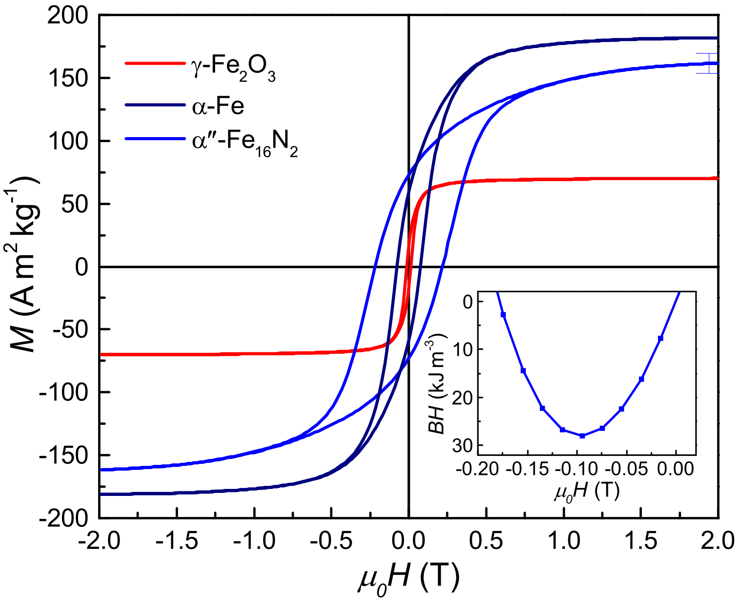

Figure 6.13: Hysteresis loops of initial γ-Fe_2O_3, intermediate α-Fe and subsequently nitrogenated α''-$Fe_{16}N_2$ nanoparticles at room temperature. Inset shows the corresponding energy product for α''-$Fe_{16}N_2$.

Table 6.2: Magnetic properties of the initial γ-Fe$_2$O$_3$, intermediate α-Fe and the final α''-Fe$_{16}$N$_2$ nanoparticles.

Phase	M_s (Am^2/kg)	M_r (Am^2/kg)	$\mu_0 H_c$ (T)
γ-Fe$_2$O$_3$	70	18	0.015
α-Fe	182	60	0.077
α''-Fe$_{16}$N$_2$	162	73	0.22

α''-Fe$_{16}$N$_2$ nanoparticles possess a saturation magnetization M_s of 162 Am^{2}kg^{-1}, a remanence M_r of 73 Am^{2}kg^{-1}, a coercivity $\mu_0 H_c$ of 0.22 T and maximum energy product $(BH)_{max}$ of 28 kJm^{-3}. This is an enhancement with respect to the α-Fe precursor and shows that α''-Fe$_{16}$N$_2$ can be considered as a semi-hard magnetic material in agreement with analysis done by other authors [184].

The saturation magnetization of α-Fe nanoparticles is slightly higher than of α''-Fe$_{16}$N$_2$, which according to reports in the literature (see Chapter 2) was not expected. This implies a partial particle oxidation or formation of other non-magnetic Fe-N phases during the nitrogenation step. As the XRD data confirms high-purity α''-Fe$_{16}$N$_2$, such secondary phases are either amorphous or in very low amount, in which case would not cause a reduction in magnetization that large. Superparamagnetism as a possible reason can be excluded due to still relatively large particle size and no evidence of a blocking temperature in the $M(T)$ data (see next section). Another possibility is the variation of the exchange coupling at the surface due to its semi-infinite nature, but that is also the case for the precursor α-Fe nanoparticles and therefore cannot be the reason for the comparably lower M_s in α''-Fe$_{16}$N$_2$. A non-collinear spin arrangement at the nanoparticle surface [185] is a phenomena observed in ultrafine particles and should be insignificant in this case. The magnetization at room temperature could also be lower, in case the Curie temperature of the α'' phase is much lower than for α-Fe. This is explored in more detail in the next section. It has to be noted that there is no consensus on the magnetization of α''-Fe$_{16}$N$_2$ in literature. For example, M_s of 226 Am^{2}kg^{-1} at room temperature was reported in [20] whereas much lower values, such as 165 Am^{2}kg^{-1}, 162 Am^{2}kg^{-1} have been measured in Refs. [110, 126, 122] (limited to works on nanoparticles only). Based on this work here, the reason for this could be particle oxidation.

As the literature values for magnetization of α''-Fe$_{16}$N$_2$ are so scattered (see Table 2.4), it was decided to investigate the possible reasons in more detail. In order to see if the measured saturation magnetization for α''-Fe$_{16}$N$_2$ (also α-Fe) nanoparticles is influenced by partial particle oxidation, series of $M(H)$ measurements gradually exposing samples to ambient conditions were conducted. To test the statistical error induced by sample preparation, handling and VSM operations, a series of experiments with the same sample, prepared and measured several times were conducted. The corresponding results are shown in Figure 6.14a and Figure 6.14b respectively. Initial M_s (before contact to air) for α''-Fe$_{16}$N$_2$ and α-Fe at room temperature are 202 Am^{2}kg^{-1} and 207 Am^{2}kg^{-1} respectively. M_s values are slightly lower than in bulk which could be caused by a number of additional reasons, as discussed above. An important observation is that the magnetization gradually decreases with exposure to ambient atmosphere. Even the initial $M(H)$ loop (blue curve in Figure 6.14a) is not closed. The nanoparticles are already oxidizing during the VSM measurement (takes $\approx$ 13 min) which results in a lowered magnetization at the end of

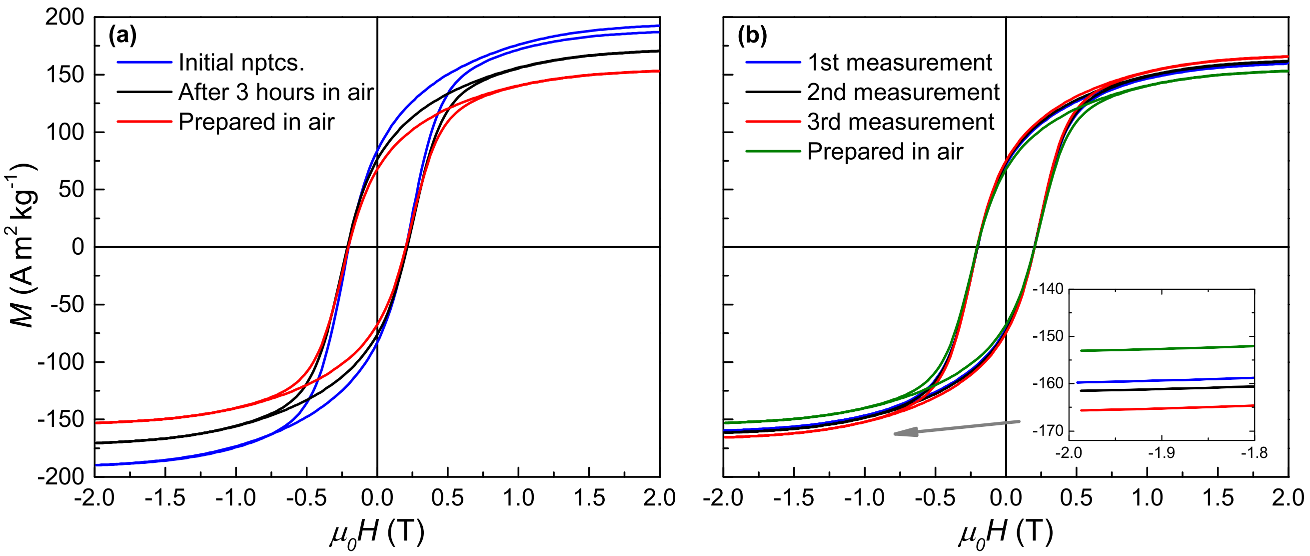

Figure 6.14: Hysteresis loops of α''-$Fe_{16}N_2$ samples showing the error in magnetization caused by the oxidation (a) and sample preparation (b).

the sequence back in the first quadrant. The same sample left in air for 3 h and re-measured has further decreased M_s as shown by the black curve.

There is also a slight statistical sample preparation and measurement error as evident from Figure 6.14b. The main contribution comes from the sample mass determination as the amount of nanoparticles used was only a few mg The estimated statistical error is about 1 %.

It is interesting to note that magnetic properties of the precursor, hydrogen reduced α-Fe nanoparticles show a pronounced dependence on the particle size. $M(H)$ loops for pure α-Fe, reduced at 663 K, 583 K, 543 K and 493 K are shown in Figure 6.15 with the corresponding M_s and H_c values in dependence of the respective particle size summarized in Figure 6.16a. The results indicate a decrease in M_s and increase in H_c with declining particle size. Similar findings have been reported by Hsu et al. [186], where the lower saturation magnetization was explained by the semi-infinite nature of fine particles, i.e., the atoms on the free surface of nanoparticles possess a lower magnetization than the bulk material. For this reason, finer particles lead to reduced M_s due to the large surface area. A possible explanation for the reduced magnetization as a function of the reciprocal particle size could also be surface oxidation. In order to address this, the change in M_s with particle size for a 5 nm (see Section 6.5 for the explanation) Fe_2O_3 shell has been calculated and plotted as the blue dotted line in Figure 6.16a. Such an oxide layer would lead to a significantly lower M_s values than observed experimentally.

The increased coercivity for smaller particles (lower reduction temperatures) is consistent with the expectation that the nucleation field is maximum for single-domain particles [181]. A spherical particle with a cubic symmetry (e.g. α-Fe) would favor single-domain state below a critical radius given by [5]:

$$R_{sd} \approx \frac{9\sqrt{AK_{1c}}}{\mu_0 M_s^2}. \tag{6.2}$$

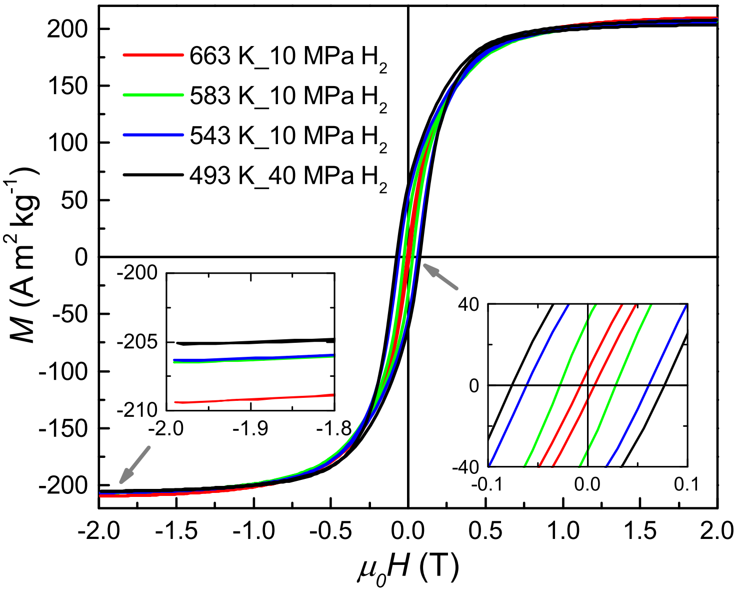

Figure 6.15: Hysteresis loops for the pure α-Fe particles, reduced at 663 K, 583 K, 543 K and 493 K. The insets show the corresponding changes in M_s and H_c.

For iron this would result in a diameter of about 10 nm–20 nm, which is still smaller than the experimental particle size, thus, a further H_c enhancement for even smaller particles can be expected.

According to the Stoner-Wohlfarth model [187], the maximum coercivity is defined by the anisotropy field $H_a = 2K_1/\mu_0 M_s$ (see Chapter 2). For iron ($K_1 \approx 50\,\mathrm{kJ\,m^{-3}}$ and $\mu_0 M_s \approx 2.15\,\mathrm{T}$), the Equation 6.2 results in $\mu_0 H_a = 0.06\,\mathrm{T}$. In reality however, the measured coercivities reach only small fraction of the theoretical H_a which is known as the *Brown's paradox* [188]. The coercivity (nucleation field) is expressed by the relationship [189]:

$$H_N = \alpha \frac{2K_1}{\mu_0 M_s} - N_{eff} M_s, \tag{6.3}$$

where α is a microstructure-related parameter (<1) and N_{eff} is the demagnetization factor respectively. Interestingly, the coercivity values shown in Figure 6.16 for the hydrogen reduced α-Fe samples reach $\mu_0 H_c = 0.076\,\mathrm{T}$, which actually exceeds the calculated anisotropy field. Moreover, as the particles are still much larger than $2{\cdot}R_{sd}$, even further enhancement in H_c can be expected. This is consistent with the work by Hsu et. al [186], where coercivity of nanophase iron increases to $\approx 0.106\,\mathrm{T}$ for the mean particle size of $\approx 30\,\mathrm{nm}$. An increase in the anisotropy constant up to $300\,\mathrm{kJ\,m^{-3}}$ (bulk α-Fe has $K_1 \approx 50\,\mathrm{kJ\,m^{-3}}$) with the reciprocal particle diameter was also reported for 2 nm α-Fe nanoparticles [190]. This increase in the anisotropy, coercivity by decreasing the particle size (increasing the surface to volume ratio) could be attributed to surface anisotropy.

Hysteresis loops for at 663 K, 583 K, 543 K and 493 K hydrogen reduced and subsequently at 403 K for 24 h nitrogenated particles (see Figure 6.10 for the structural information) are shown in Figure 6.17. The corresponding M_s and H_c values in dependence of the respective particle size are summarized in Figure 6.16b. A significant enhancement in coercivity with lowering the reduction temperature (increased

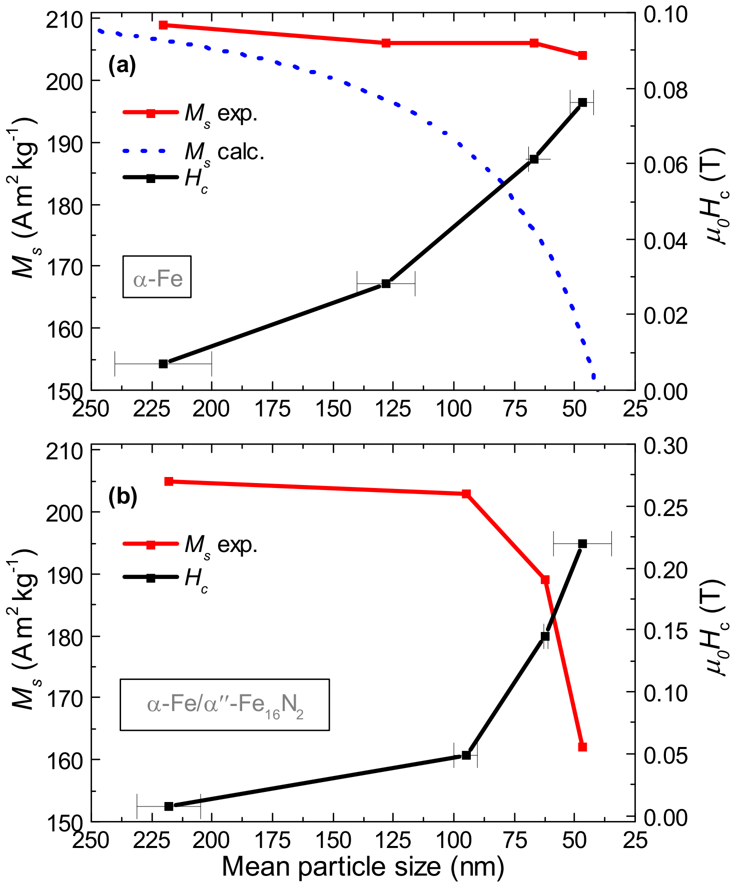

Figure 6.16: M_s and H_c as a function of the particle size for the hydrogen reduced α-Fe (a) and subsequently nitrogenated α-Fe/α''-$Fe_{16}N_2$ (b) nanoparticles.

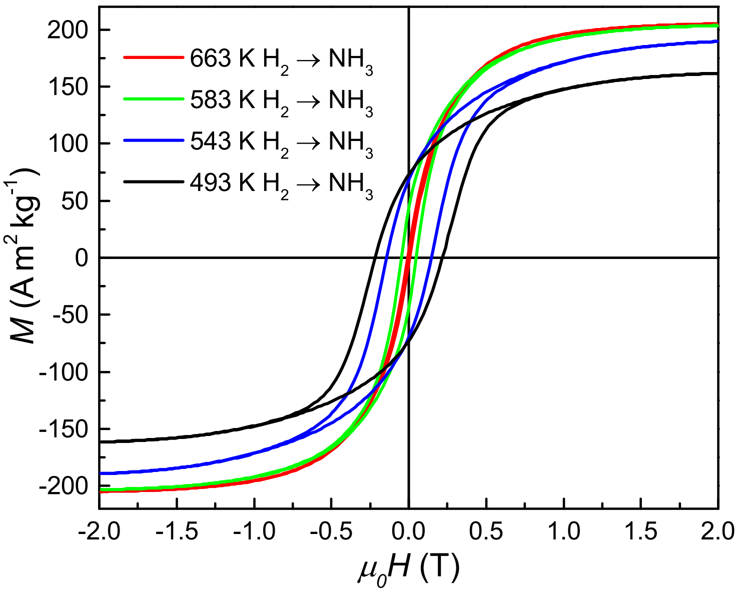

Figure 6.17: Hysteresis loops of the at different temperatures hydrogen reduced and subsequently nitrogenated α-Fe/α''-$Fe_{16}N_2$ particles.

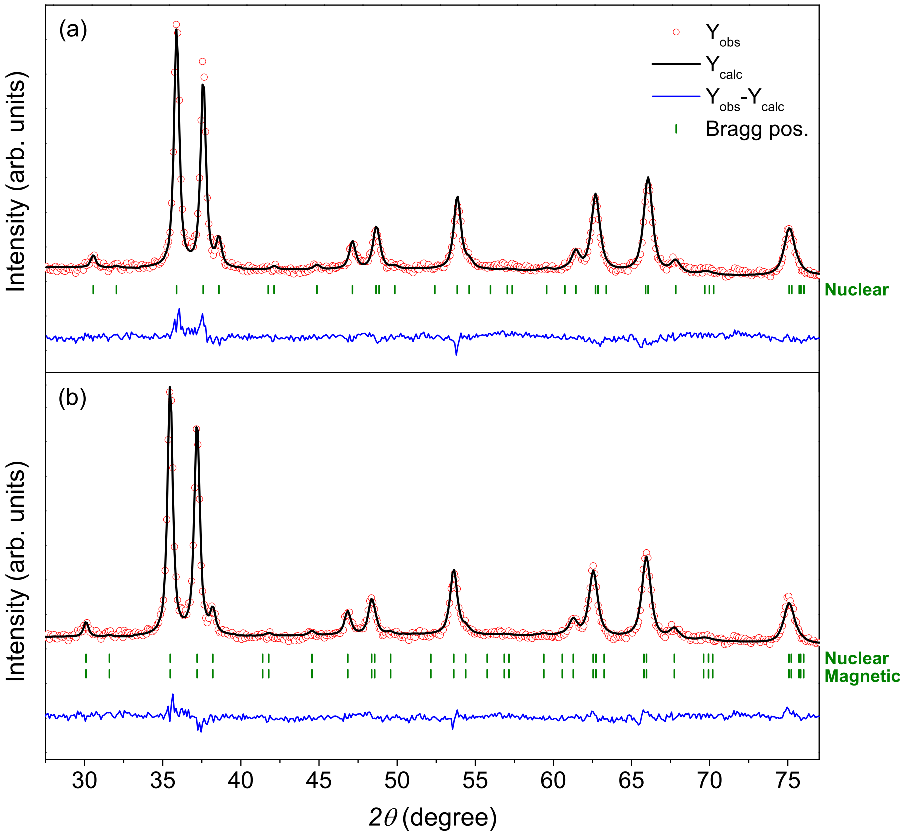

Figure 6.18: Refinements of the neutron ($\lambda = 1.28\,\text{Å}$) diffraction pattern for α''-$Fe_{16}N_2$ nanoparticles taken at 300 K. In figure (a) the row of Bragg markers corresponds to the nuclear contribution. In figure (b) the top and second rows of Bragg markers refer to the nuclear and magnetic contributions of the α''-$Fe_{16}N_2$ phase.

α''-$Fe_{16}N_2$ yield) is evident. As the particle size after nitrogenation remains almost unchanged (see Figure 6.11), the above discussed particle size effects should be roughly similar to both, hydrogen reduced α-Fe and nitrogenated α''-$Fe_{16}N_2$ samples. Therefore, the enhanced H_c here is clearly attributed to the formation of the magnetically semi-hard α''-$Fe_{16}N_2$ phase.

For a deeper insight into the physical properties of α''-$Fe_{16}N_2$ system, a precise knowledge of both, crystallographic and magnetic structure is required. With that aim, neutron diffraction experiments have been performed.

Rietveld refinements of the neutron diffraction pattern recorded at 300 K are illustrated in Figure 6.18. Only reflections from α''-$Fe_{16}N_2$ structure are present, thus confirming the phase-purity of the samples. Refinement of the nuclear part only (Figure 6.18a) gives a reasonably good fit, except for the (202) and (220) reflections (at 35.5° and 37.2° respectively) where the magnetic contribution results in an intensity difference. By adding the magnetic contribution in the refinement (Figure 6.18b), the fit can be further improved, all the intensities are well represented by the calculated curve. Unfortunately, no reliable atomic magnetic moment values could be extracted. As indicated by the markers, the magnetic contribution of α''-$Fe_{16}N_2$ is entirely overlapping with the nuclear one. Furthermore, due to the poor thermal stability, the samples could not be measured in the paramagnetic state (α''-$Fe_{16}N_2$ decomposes already before reaching the Curie temperature), therefore separation of the nuclear and magnetic contributions was not possible. This is in agreement with attempts done by other researchers [116, 110]. In [110] authors report that noticeable magnetic scattering was observed only for (202) and (220) reflections, and the resulting magnetic moments are highly erroneous due to the small magnetic contribution to the pattern.

6.4.2 Anisotropy

A very important property, especially for hard magnetic materials, is magnetic anisotropy. In the case of the present α''-$Fe_{16}N_2$ nanoparticles, they are polycrystalline and therefore typical easy/hard direction measurements for determination of the anisotropy field could not be applied. For this reason, here the *Singular point detection* (SPD) method which was first proposed and described by Asti and Rinaldi [191, 192] was used. The core idea of the SPD method is that, for polycrystalline materials, a sharp peak can be observed in the second derivative of the magnetization with respect to the magnetic field, d^2M/dH^2, at $H = H_a$. The measurements have been done in cooperation with Prof. Franca Albertini at the Institute of Materials for Electronics and Magnetism (IMEM) of the National Research Council (CNR), Magnetic Materials Group.

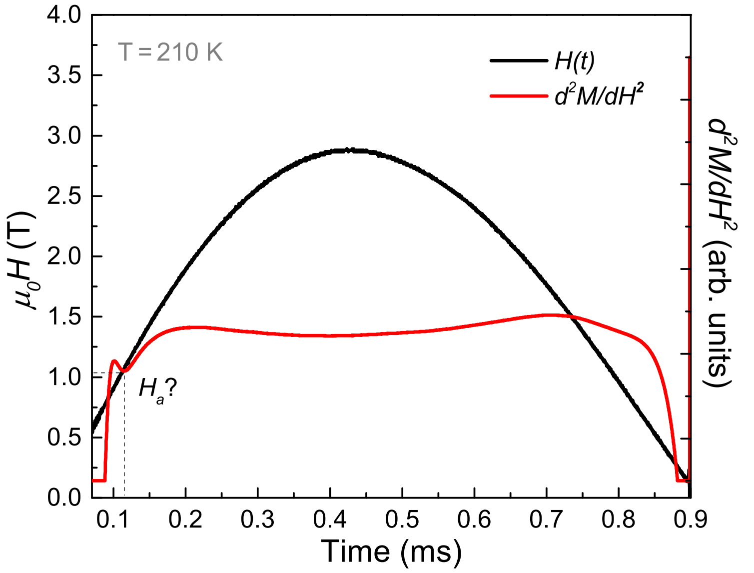

Figure 6.19: Singular point detection method for measuring anisotropy field in polycrystalline sample applied to α''-$Fe_{16}N_2$ nanoparticles. The peak around 1 T in the d^2M/dH^2 could correspond to the anisotropy field H_a.

In order to roughly estimate the range where the peak should lie, the expected H_a value was calculated. By using the experimentally measured M_s for the present α''-$Fe_{16}N_2$ nanoparticles and in the literature reported $K_u = 0.96\,\mathrm{MJ\,m^{-3}}$ [20], Equation 2.7 gives $\mu_0 H_a \approx 1.2\,\mathrm{T}$. The SPD measurement results are shown in Figure 6.19. A sinusoidal magnetic field pulse with a duration of roughly 1 s and amplitude of about 3 T was used. A peak in the d^2M/dH^2 data at a magnetic field of about 1.05 T is observed. This is indeed not far from the calculated value. It has to be noted that problems experienced with the measurement setup unfortunately do not allow this value to be considered as fully reliable (hence the question mark). The peak position was varying with the different hardware parameters of the SPD device. Therefore other, more stable methods should be used for a confirmation of this H_a value. Easy/hard axis $M(H)$ measurements as well as ferromagnetic resonance experiments on field-aligned α''-$Fe_{16}N_2$ nanoparticle samples were tried, but did not lead to a reliable H_a estimation.

6.4.3 Curie temperature and exchange stiffness

The thermal behavior of the magnetic properties is important for both, the possible α''-$Fe_{16}N_2$ applications as well as fundamental understanding. For example, if the Curie temperature T_C for the α''-$Fe_{16}N_2$ nanoparticles is much lower than that of α-Fe, it could provide a plausible explanation for the slightly reduced M_s at room temperature.

Considering the in previous sections described poor thermal and chemical stability of the α''-$Fe_{16}N_2$ nanoparticles, special care needs to be exercised for sample handling. In case of particle oxidation during the measurement, the accompanied reduction in M_s will lead to underestimated T_C. Therefore, the samples were sealed into quartz capillaries in Ar filled glovebox and the measurements were performed in vacuum conditions. As pure iron naonoparticles are very reactive, they were measured by the same procedure and used as a reference. $M(T)$ measurement results in a temperature range from room temperature to 850 K for the precursor α-Fe nanoparticles are plotted in Figure 6.20a. As expected, no phase transitions are present for the α-Fe nanoparticles in the whole studied temperature range. Small offset in the heating/cooling curves is caused by a lag in the temperature acquisition of the VSM setup. $M(H)$ loops before and after the $M(T)$ experiment (inset in Figure 6.20a) show no difference in magnetization (in case of oxidation, a significant reduction in M_s should occur). Narrowing of the loops, reduction in H_c is caused by particle growth at elevated temperatures during the measurement, in accordance to the

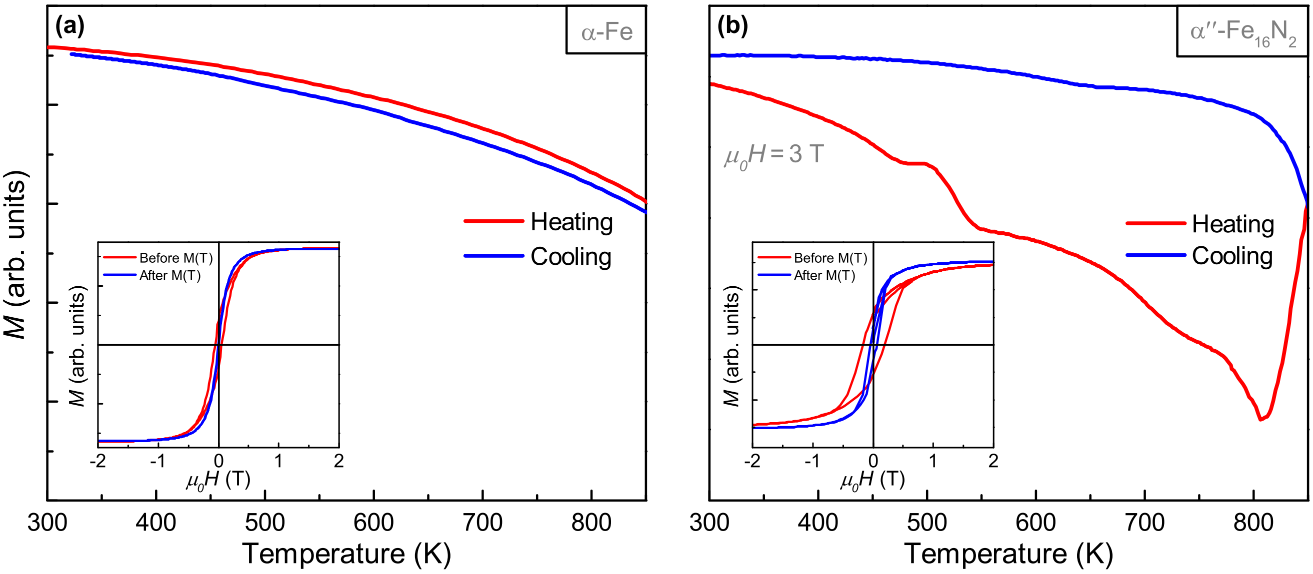

Figure 6.20: VSM $M(T)$ measurement results representing thermal stability of (a) α-Fe and (b) α''-$Fe_{16}N_2$ nanoparticles. The insets show the corresponding $M(H)$ plots before and after $M(T)$.

results presented in the previous section. Normally, the iron nanoparticles burn when exposed to atmosphere even at room temperature and thus would be completely oxidized during the $M(T)$ measurement sequence. The absence of this confirms that the measurement quality is good and sample oxidation is avoided.

$M(T)$ measurement results for α''-$Fe_{16}N_2$ nanoparticles are shown in Figure 6.20b. The decomposition behavior that became evident from XRD is observed here also. At first, around 460 K α''-$Fe_{16}N_2$ decomposes into α-Fe and γ'-Fe_4N. Then, the γ'-Fe_4N fraction increases with respect to α-Fe, which results in a further reduction in magnetization. Around 700 K the amount of α-Fe is rising and thus lowering the slope with which γ'-Fe_4N approaches its Curie temperature ($\approx$ 716 K–761 K [30, 147]), and finally a rapid decomposition in α-Fe accompanied by a steep enhancement in magnetization is apparent. $M(H)$ measurements before and after the $M(T)$ (inset Figure 6.20b) confirm the transformation into α-Fe. The magnetic hardness is lost and the saturation magnetization slightly increases, similarly to the $M(H)$ results shown in the foregoing section.

In order to estimate the Curie temperature T_C the magnetization versus temperature data in the range were α''-$Fe_{16}N_2$ is still stable (from 0 K up to about 463 K) as shown in Figure 6.21 was considered. Equation 2.10 proposed by Kuz'min [119] was used for fitting the experimental $M(T)$ data. The corresponding results are represented by the red dashed curves in Figure 6.21.

Also here, the α-Fe nanoparticles were used as a reference as shown in Figure 6.21a. The obtained T_C was 1055 K with $s = 0.41$ and $p = 3.2$. Considering the measurement and fitting errors, this is in a very good agreement with the literature value of 1044 K ± 2 K [193].

For the α''-$Fe_{16}N_2$ nanoparticles, the best fit was achieved with $s = 0.42$ and $p = 3.8$ resulting in $T_C \approx$ 634 K as shown in Figure 6.21b. Previously a T_C value of 813 K (540 °C) has been reported for thin films [89]. A part of the reason for lower T_C estimated in the present work could be related to surface effects of the nanoparticles. On the other hand, authors of Ref. 89 have used the Langevin function for fitting their experimental data and it is well-known that mean-field models tend to overestimate the Curie temperature. As an illustration, also the solutions for the Langevin function have been plotted in Figure 6.21b (the grey dashed line) and it is obvious that fitting the experimental data with it would result in a much higher T_C value.

In summary, the reduced M_s in comparison to α-Fe observed at room temperature is a direct consequence of the much lower Curie temperature. The $M_s(0)$ for α''-$Fe_{16}N_2$ nanoparticles of 215 Am^2kg^{-1} is actually slightly higher than $M_s(0)$ of the corresponding precursor α-Fe nanoparticles (210 Am^2kg^{-1}).

Another important parameter for different possible α''-$Fe_{16}N_2$ applications is the exchange stiffness A. The calculation of typical length scales in nano-magnetism, such as the critical single- domain radius ($R_{sd} = 36\sqrt{K_1 A/\mu_0 M_s^2}$) or the exchange length ($l_{ex} = \sqrt{A/\mu_0 M_s^2}$) require knowledge of A. The exchange stiffness parameter A for α''-$Fe_{16}N_2$ nanoparticles has not been reported in literature so far.

Here the exchange stiffness parameter A was estimated by two different methods - from low temperature magnetization measurements and from the Curie temperature. The relation of saturation magnetization

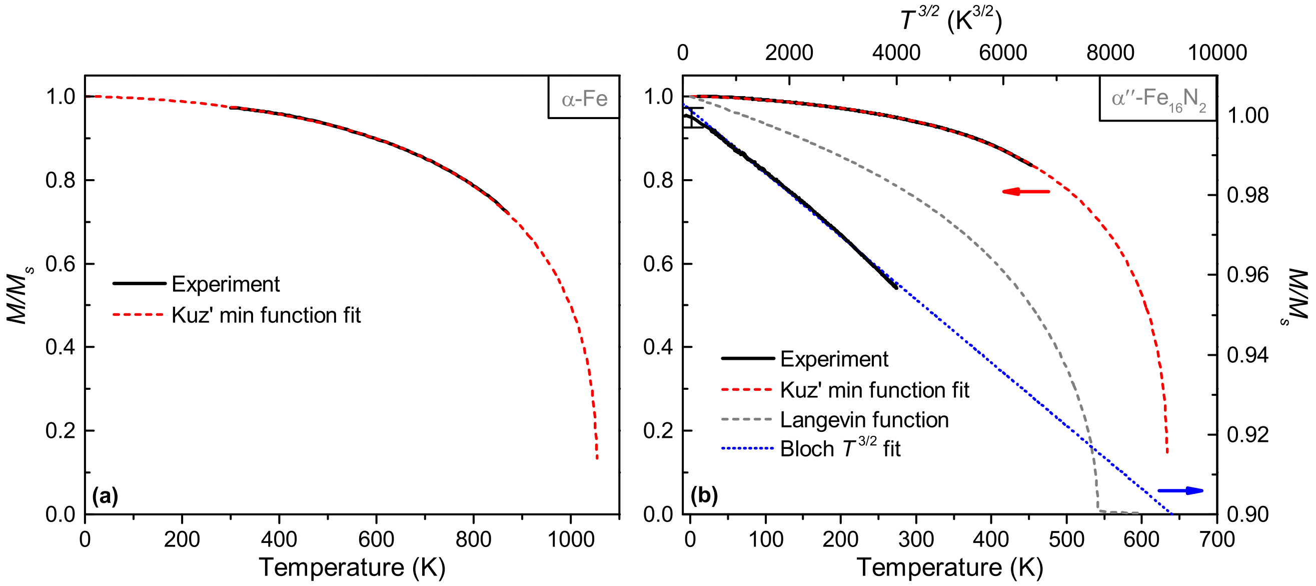

Figure 6.21: (a) VSM $M(T)$ measurement results and the corresponding fit for pure α-Fe nanoparticles as a reference. (b) Experimental $M(T)$ and calculated data for extracting T_c and A values in the temperature range where α''-$Fe_{16}N_2$ nanoparticles are still stable.

at a given temperature $M_s(T)$ to the extrapolated saturation magnetization at 0 K $M_s(0)$ can be described by the Bloch $T^{3/2}$ law as follows [194]:

$$\frac{M_S(T)}{M_S(0)} = 1 - 0.0587\,(Qu)^{1/2}\left(\frac{k_B T}{2Aa}\right)^{3/2}, \tag{6.4}$$

where Q is the number of atoms per unit cell, $u = M_s(0)a^3/\ Qg\mu_B$, k_B is Boltzmann constant, a is the lattice constant, g is Landé factor and A is the exchange stiffness constant. By fitting the experimental data in a temperature range from 2 K to 250 K with $M_s(T)/M_s(0) = 1 - \alpha T^{3/2}$ (Figure 6.21b), inserting the obtained α value into Equation 6.4 and solving for A (using the experimental a, c lattice constants and $g = 2.0$ [104]) the values $A_c = 6.84\,\mathrm{pJ\,m^{-1}}$ and $A_{a,b} = 7.53\,\mathrm{pJ\,m^{-1}}$ (as α''-$Fe_{16}N_2$ is uniaxial, A has two, in-plane $A_{a,b}$ and out-of-plane A_c components) were obtained. The exchange stiffness parameter is related to T_C via $A \approx k_B T_C/2a$ [5]. Solving this for the previously from $M(T)$ measurements obtained $T_C = 634\,\mathrm{K}$ and from XRD Rietveld refinement extracted lattice constants, results in $A_c = 6.95\,\mathrm{pJ\,m^{-1}}$ and $A_{a,b} = 7.66\,\mathrm{pJ\,m^{-1}}$ which are in very good agreement with the above from Bloch $T^{3/2}$ calculated values.

6.5 Chemical analysis

In order to clarify the possible reasons for the reduced magnetization, chemical composition on both macro- and nano-scale, and electronic structure were investigated.

XPS acquisitions were performed on the material at all three process steps - initial γ-Fe_2O_3, hydrogen reduced α-Fe and nitrogenated α''-$Fe_{16}N_2$ nanoparticles. The binding energies were calibrated using C

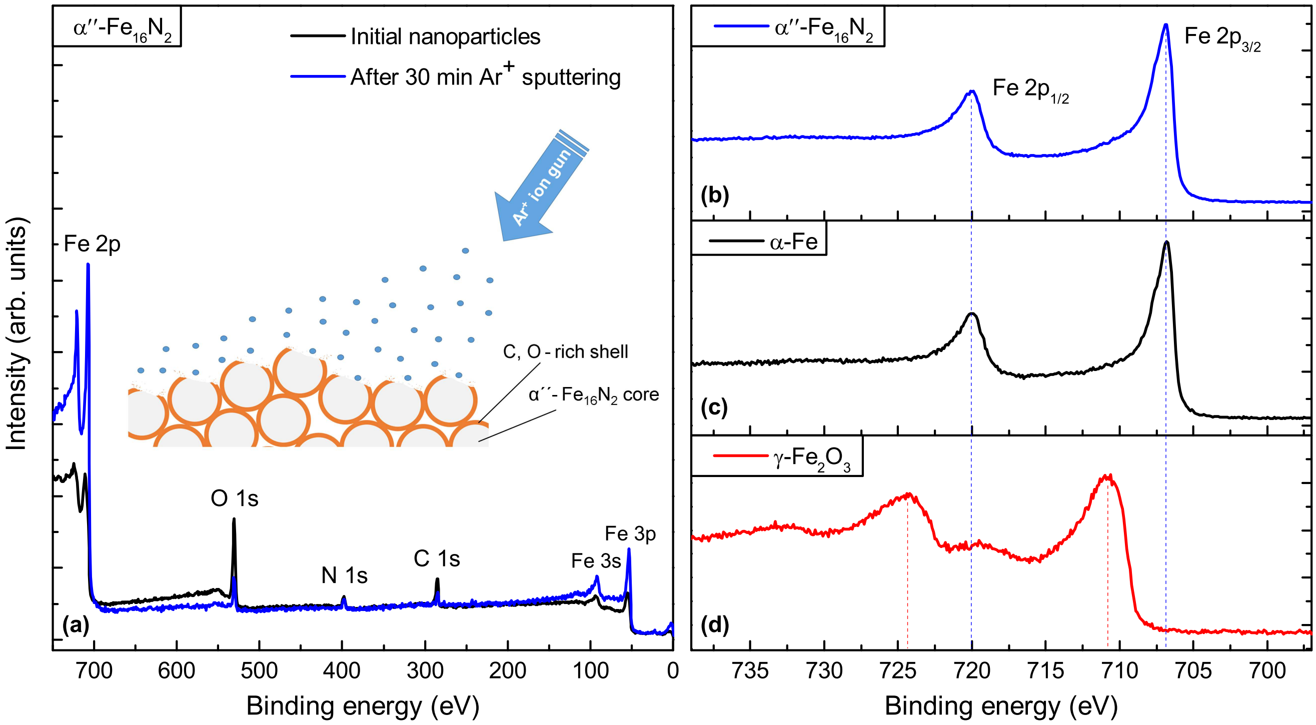

Figure 6.22: XPS results on γ-Fe_2O_3, α-Fe and α''-$Fe_{16}N_2$ samples. (a) Survey measurements and (b)-(d) the respective Fe 2p spectra after Ar^+ sputtering.

1s at 284.8 eV as a reference. Even though the samples were always handled in a protective atmosphere, the measured survey spectra shows large amount of oxygen and carbon on the surface of the samples (Figure 6.22a), no other impurities were detected. After 10 minutes of Ar^+ ion (2 kV, 45°) sputtering the amount of O, C is reduced significantly, but still not vanishing and further etching up to 1 h does not change the spectra anymore. This can be explained with the surface roughness of the sample. That is, as the sample is not flat, but consists of nanoparticles with dimensions of about 50 nm and the measurement area is roughly 200 μm^2, once the oxide shell segment frontal to the Ar^+ beam has been removed from the particle surface, there will still remain parts of oxide layer emitting photoelectrons due to the particle curvature (see inset Figure 6.22a). After Ar^+ sputtering measured Fe 2p XPS spectra for α''-$Fe_{16}N_2$, α-Fe and γ-Fe_2O_3 nanoparticles are presented in Figure 6.22 (b), (c) and (d) respectively. In case of the initial γ-Fe_2O_3 nanoparticles, the binding energies for Fe $2p_{1/2}$ and Fe $2p_{3/2}$ are 710.8 eV and 724.5 eV respectively, which considering the measurement accuracy are in good agreement with literature values [195, 196]. α-Fe and α''-$Fe_{16}N_2$ nanoparticles show a text-book like Fe 2p spectrum with Fe $2p_{1/2}$ and Fe $2p_{3/2}$ at 706.8 eV and 719.9 eV which are in agreement with earlier reports on iron nitrides [30, 31]. As no traces from iron oxide could be observed in Fe 2p spectra it is concluded that the iron oxide content in the α''-$Fe_{16}N_2$ nanoparticles is very low. Small shoulders observed in 1s spectra of C, N, O indicate possible presence of C-O, C-N binding which suggests that the surface contamination layer is probably a mixture of iron oxide and some organics.

In order to study the possible oxidation in more detail, TEM investigations were performed. Figure 6.23 shows a HAADF image of a nanoparticle cluster. The rightmost particle was selected for STEM-EELS mapping as indicated by the green square. Elemental maps extracted from the EELS data for Fe-L (red),

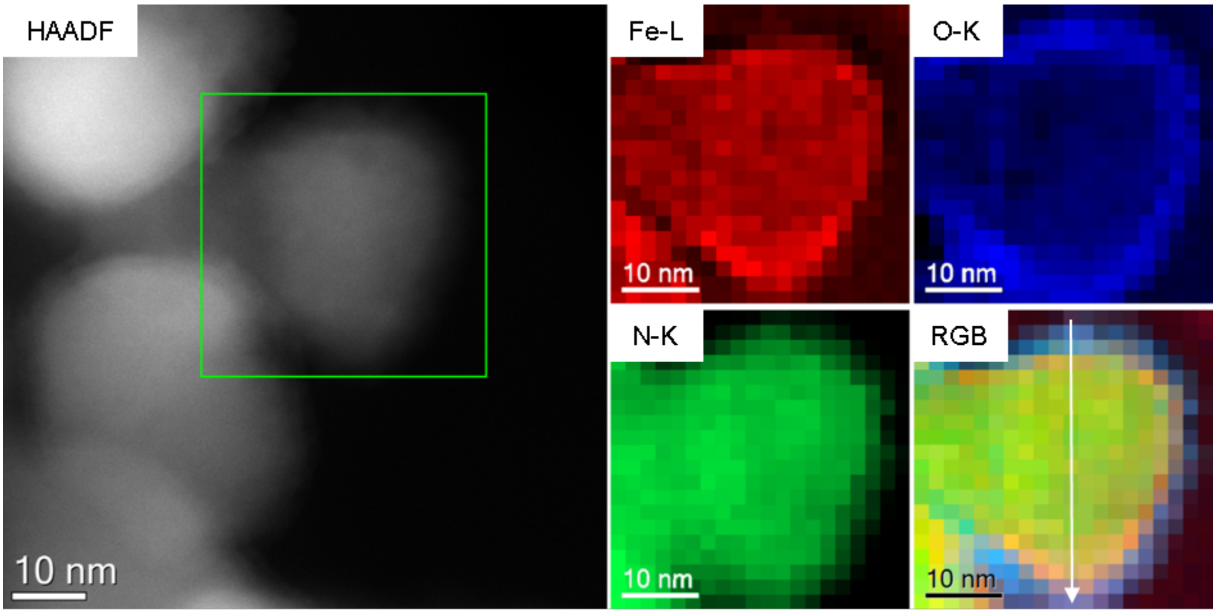

Figure 6.23: HAADF image and the corresponding STEM-EELS elemental maps using the Fe-L (red), O-K (blue) and N-K (green) ionization edges (the mapped area is indicated by the green square).

N-K (green)and O-K (blue) as well as an RGB map created from the single elemental maps are presented. The oxide shell is directly visible by the blue-colored shell surrounding the nanoparticle.

A line profile was extracted from the maps along the white arrow shown in Figure 6.23. The line profile is shown in logarithmic intensity scale in Figure 6.24a. The shell is identified by the two grey squares on each side of the extracted line profile. The width of the oxide shell was determined to be around 5 nm–7 nm ± 2 nm. Figure 6.23b shows single EELS spectra extracted from the core (black curve) and the shell (red curve). Both were compared to a reference spectrum of Fe_2O_3 (blue curve) [197]. The spectrum corresponding to the shell and the Fe_2O_3 reference spectrum are almost identical when using the O-K and the Fe-$L_{2,3}$ ionization edges for the analysis. There are only minor differences, indicating

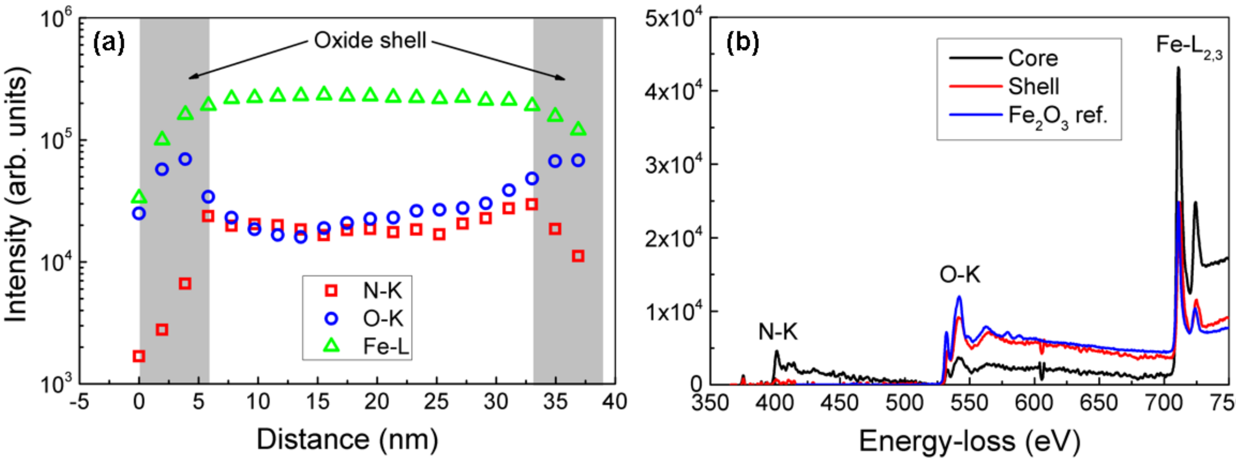

Figure 6.24: STEM-EELS line profiles along the direction indicated in Figure 6.23 (a). Comparison of the extracted EELS spectra from the core and shell area with respect to a Fe_2O_3 reference spectrum [197] (b).

that the shell consists of Fe_2O_3. Nitrogen was not observed in the shell, but only within the particle core, as evident from the extracted EELS spectra.

6.6 Summary

This chapter demonstrated that by increasing hydrogen pressure from atmospheric to 53 MPa, it is possible to reduce the temperature necessary for complete reduction of γ-Fe_2O_3 from 663 K down to 483 K, which resulted in phase-pure α-Fe nanoparticles without detrimental particle coarsening. The hydrogen reduction step temperature and the respective particle size have a significant impact on the subsequent nitrogenation behavior of the α-Fe. Subsequent nitrogenation in NH_3 flow for 12 h–24 h at temperatures around 403 K yields high purity α''-$Fe_{16}N_2$ nanoparticle samples, without further particle growth.

Under inert atmosphere α''-$Fe_{16}N_2$ nanoparticles are stable up to roughly 463 K. In air already at around 433 K oxidation takes place, which needs to be considered in possible applications.

α''-$Fe_{16}N_2$ nanoparticles show semi-hard magnetic properties with magnetization at 0 K of $M_s(0) = 215\,\mathrm{Am^2kg^{-1}}$ and coercivity $\mu_0 H_c = 0.22\,\mathrm{T}$. $T_C = 634\,\mathrm{K}$, $A_c = 6.84\,\mathrm{pJ\,m^{-1}}$ and $A_{a,b} = 7.53\,\mathrm{pJ\,m^{-1}}$.

XPS and STEM-EELS results suggest that the reduced magnetization for α''-$Fe_{16}N_2$ nanoparticles is caused by the surface oxidation. The TEM specimens were prepared under atmospheric air conditions, whereas the XPS samples were handled without exposure to air. The results show that even when working under glovebox conditions surface oxidation of the nanoparticles could not be completely avoided.

7 Evaluation of potential Fe_8N_x applications

In this chapter the previously presented results are discussed in terms of the potential Fe_8N_x applications (which here refers to both α'-Fe_8N_x and α''-$Fe_{16}N_2$ phases). As already mentioned in the introduction, α'-Fe_8N/α''-$Fe_{16}N_2$ has been suggested as a possible rare-earth-free permanent magnet candidate, as a semi-hard phase in hard-soft composite magnets as well as a potentially interesting material for biomedical purposes and high density magnetic recording. Therefore, these topics are addressed here, considering the physical and chemical characteristics observed in the foregoing chapters of this work.

7.1 Permanent magnets

After the rare-earth crisis in 2011 [8], the search for alternatives to Nd-Fe-B, meaning rare-earth-lean or rare-earth-free hard magnetic materials regained a lot of attention [9]. As chances for realizing a competitive performance (mainly in terms of the anisotropy and consequently the coercivity) without rare-earth elements are uncertain due to the much lower spin-orbit coupling as well as the quenched orbital moment in $3d$ metals [82], the proposed approach is to investigate materials with moderate performance that could operate in the performance gap, considering $(BH)_{max}$ versus temperature, between hard ferrites and rare-earth permanent magnets [10].

The α''-$Fe_{16}N_2$ phase has been suggested by a number of authors as one possible rare-earth-free permanent magnet candidate [20, 21, 22, 23]. Also several patent applications have been filed describing the process of making α''-$Fe_{16}N_2$ magnets [198, 199, 200].

The purpose of this section is to evaluate its suitability for permanent magnet applications, by critically considering the magnetic properties as well as the stability of α''-$Fe_{16}N_2$.

The following intrinsic and the resultant extrinsic material properties are crucial for permanent magnet applications:

- High intrinsic saturation magnetization M_s and extrinsic remanent magnetization M_r
- High intrinsic anisotropy field H_a and extrinsic coercivity H_c
- High Curie temperature T_C
- High maximum energy product $(BH)_{max}$
- Good thermal and chemical stability
- The possibility of full densification and high degree of texture (alignment of individual grains).

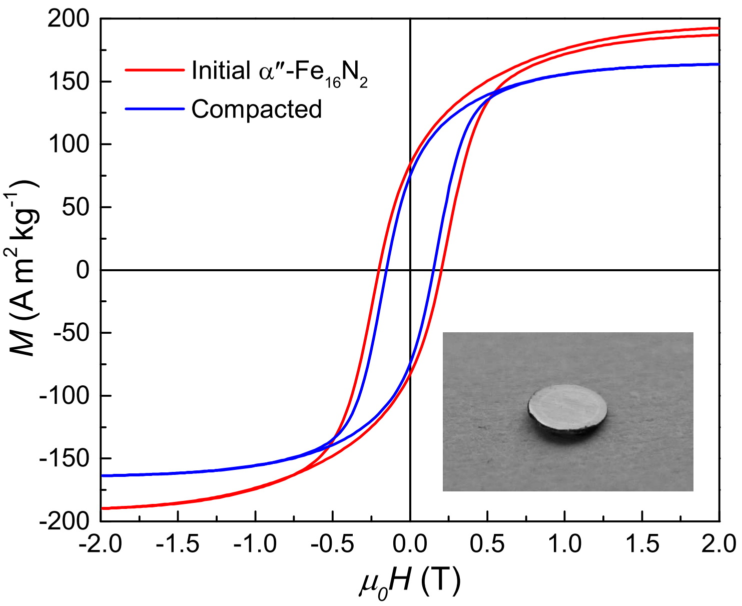

Figure 7.1: Hysteresis loops of the initial α''-Fe$_{16}$N$_2$ nanoparticles and after consolidation (at room temperature).

Let us address them one by one in the context of α''-Fe$_{16}$N$_2$ phase.

The initial (before contact to air) M_s for α''-Fe$_{16}$N$_2$ nanoparticles at room temperature was 202 Am^{2}kg^{-1} (see Chapter 6). This value is much higher than M_s of ferrites or Nd-Fe-B magnets [5]. However, the remanent magnetization M_r is more important for applications. So far a good squareness in bulk α''-Fe$_{16}$N$_2$ is hard to realize, resulting in a rather low M_r.

The anisotropy field H_a calculated according to $H_a = 2K_1/\mu_0 M_s$ by using the experimentally measured M_s for the present α''-Fe$_{16}$N$_2$ nanoparticles and in the literature reported $K_u = 0.96\,\mathrm{MJ\,m^{-3}}$ [20] gives $\mu_0 H_a \approx 1.2\,\mathrm{T}$. The SPD method used in the present work lead to a comparable result (1.05 T). This value is smaller than for ferrites and Nd-Fe-B magnets. The maximum coercivity is defined by the anisotropy field and in reality the achieved coercivities reach only small fraction of the theoretical H_a (Brown's paradox). For example, the anisotropy field of Nd$_2$Fe$_{14}$B is 7.5 T, whereas coercivities of Nd-Fe-B magnets reach only about 25 %. The present α''-Fe$_{16}$N$_2$ samples possess a coercivity $\mu_0 H_c$ of 0.22 T which is already close to the 25 % of H_a and therefore a significant further enhancement will be difficult to achieve. A slight increase could still be realized by moving closer to the single-domain particle size as well as magnetically decoupling the domains. Moreover, the H_c further decreases after consolidation of the powder (Figure 7.1). The same phenomena was observed by Takagi et al. [21] in high-pressure sintering experiments of α''-Fe$_{16}$N$_2$ nanopowders.

This reveals the difficulties concerning α''-Fe$_{16}$N$_2$ as a potential permanent magnet material - the anisotropy is simply not enough to be able to resist self-demagnetization, especially if the claimed high magnetization value could be realized. In principle the anisotropy field H_a should exceed the demagnetization field H_d:

$$\frac{2K_1}{\mu_0 M_s} > N_d M_s, \tag{7.1}$$

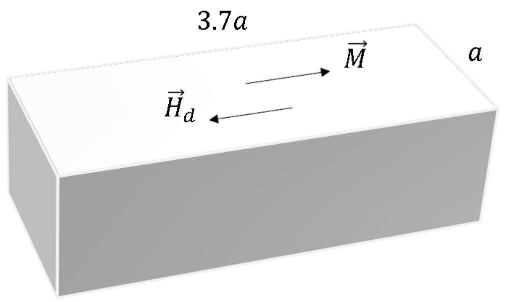

Figure 7.2: Due to the relatively low MAE, a rectangular α''-$Fe_{16}N_2$ magnet should be shaped with c/a ratio $\geqslant 3.7$ in order to withstand self-demagnetization (figure not to scale).

where N_d is the demagnetization factor. In reality however, it is the coercivity H_c which has to stand against the demagnetization and therefore exceed the H_d. For the current α''-$Fe_{16}N_2$ the relation 7.1 would thus lead to $N_d < 0.12$. Based on the relation given in [201], this corresponds to a rectangular prism with c/a ratio of 3.7 as illustrated in Figure 7.2. So, as far as the anisotropy is concerned, the α''-$Fe_{16}N_2$ could operate only at geometries with a low demagnetization factor.

The magnetic magnetic hardness parameter can be defined as follows [184]:

$$k = \sqrt{(K_1/\mu_0 M_s^2}. \tag{7.2}$$

For a permanent magnet k should be larger than 1 [5]. α''-$Fe_{16}N_2$ possesses $k \approx 0.5$ and therefore must be considered as a semi-hard magnetic material.

The Curie temperature of α''-$Fe_{16}N_2$ estimated in this work is $T_C = 634\,\mathrm{K}$. This is higher than the T_C of Nd-Fe-B, and would be suitable for ordinary permanent magnet applications.

Due to the low H_c, a lack of texture and poor squareness, the maximum energy product $(BH)_{max}$ for the α''-$Fe_{16}N_2$ nanoparticles studied in this work reached only $28\,\mathrm{kJm^{-3}}$. This reflects the rather modest performance and at the present stage puts α''-$Fe_{16}N_2$ even below Alnico magnets.

As discussed in the previous chapter, the poor thermal and chemical stability of α''-$Fe_{16}N_2$ indicate that the magnet production might be difficult. Due to the danger of oxidation, the samples should always be handled in protective atmosphere. Under inert conditions α''-$Fe_{16}N_2$ nanoparticles are stable up to roughly 463 K, followed by decomposition into α-Fe and γ'-Fe_4N, which makes conventional processing routes, such as sintering, a very challenging, if not impossible, task.

To conclude, the analysis presented in this section has shown that α''-$Fe_{16}N_2$ is not suitable as a permanent magnet material, but can be considered a magnetically semi-hard phase. As such, it can be used in geometries with very low demagnetization factors or in hard-soft composite magnets in agreement with the assessment provided elsewhere [24, 184].

7.2 Nanocomposite magnets

One possible way of improving the $(BH)_{max}$ in permanent magnets is the concept of *exchange-coupled nanocomposites*. This was demonstrated experimentally for the first time by Coehoorn et al. in 1989 [202] where a remanance enhancement in $Nd_2Fe_{14}B/Fe_3B$ composite magnets was observed. Theoretical aspects were covered later by Kneller and Hawig [203] in 1991 and Skomski and Coey [204] in 1993. The idea builds on the relation

$$(BH)_{max} \leq \frac{M_s^2}{4\mu_0}. \tag{7.3}$$

In reality, significant $(BH)_{max}$ values can only be realized in materials with sufficiently high anisotropy. The criteria for a permanent magnet is that the hardness parameter k (see previous section) should be greater than 1. However, if a hard magnet possesses a k value exceeding 1, a further increase in M_s could be allowed by a K_1 without negatively affecting the hardness performance (Equation 7.2). Hence, a composite material which consists of two well dispersed, exchange-coupled phases - one with large k providing the anisotropy and the other with low k enhancing the M_s - could be realized.

The dimensions of the soft phase are critical for sustaining a coherent magnetization reversal and should not exceed approximately twice the domain-wall width of the hard phase:

$$\delta_h = \pi\sqrt{\frac{A_h}{K_h}}, \tag{7.4}$$

where K_h is the anisotropy constant and A_h is the exchange stiffness of the hard phase [203]. At such dimensions the exchange interactions suppress the reversible rotation of the magnetization in the soft magnetic phase at low fields [205].

As discussed above, α''-$Fe_{16}N_2$ is a semi-hard magnetic phase. This has several interesting advantages in the case of utilization in nanostructured two-phase magnets. The function of the soft phase in exchange-coupled magnets is to enhance the magnetization. However, the coercivity is usually affected negatively. Replacing the soft phase with a semi-hard one would yield an improvement in the coercivity due to the enhanced average anisotropy [24]. The second advantage of a semi-hard instead of a completely soft magnetic material can be understood from Equation 7.4. In the case of a semi-hard phase, the term K_h in the denominator has to be replaced by $K_h - K_s$, where K_s is the anisotropy constant of the soft phase [24]. This shows that the critical dimensions for a semi-hard phase become larger in comparison to a soft phase which makes it easier to practically produce and handle the material.

Table 7.1: Magnetic properties of the $SrAl_2Fe_{10}O_{19}$ (Al_2SrM) nanoparticles used as a hard phase.

M_s (Am^2/kg)	44
$\mu_0 H_c$ (T)	0.789
K_u (MJ/m^3)	0.238
A (pJ/m)	6

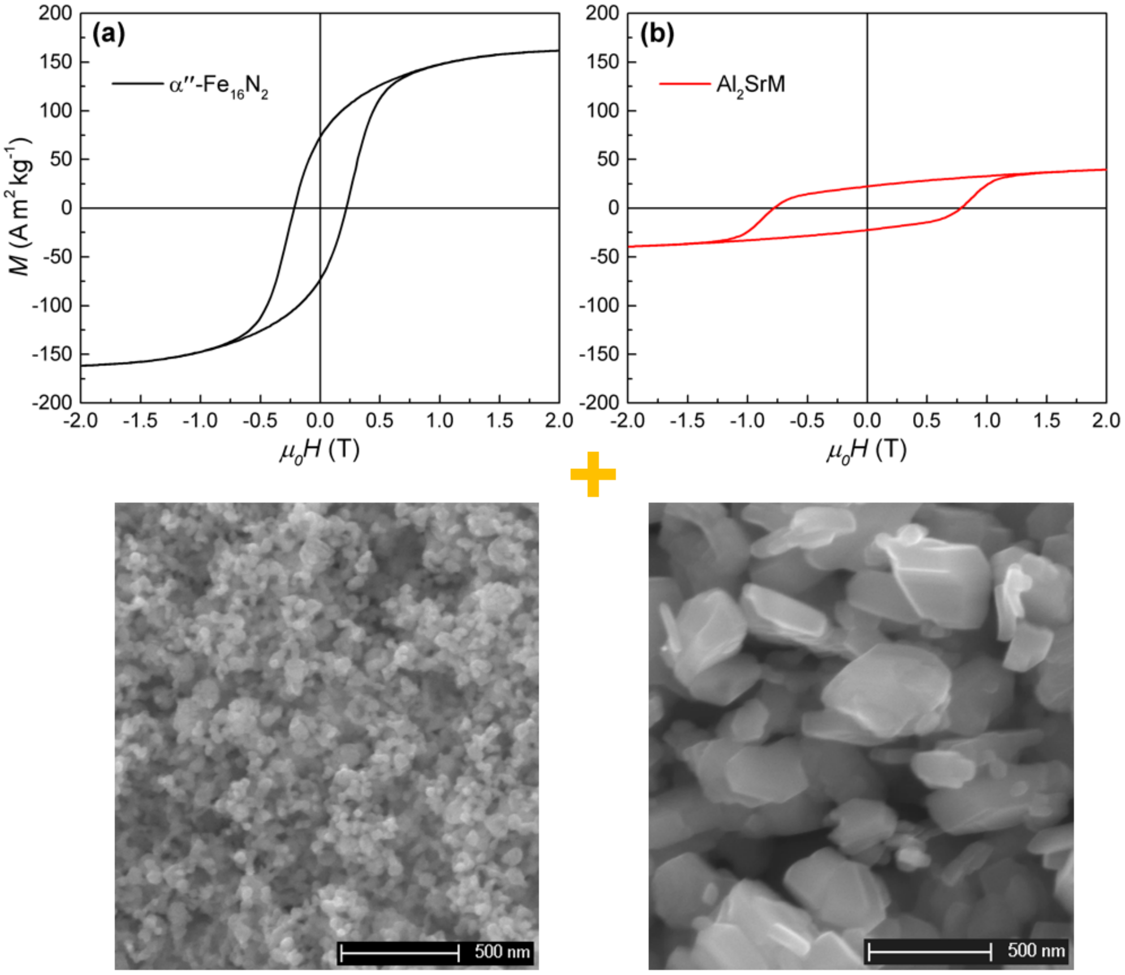

Figure 7.3: Hysteresis loops and microstructure for the (a) α''-$Fe_{16}N_2$ and (b) Al_2SrM nanoparticles used for production of nanocomposite magnets.

The magnetically hard phase for this study was chosen as follows. Instead of looking at typical hard magnet alloys with large K_u, such as $Nd_2Fe_{14}B$ or $Sm_2Fe_{17}N_3$, a different strategy was used. In the previous chapter it was discussed that even after decades of microstructure engineering the coercivity H_c usually reaches only about 30 % of the anisotropy field H_a, which is represented by the factor α in Equation 6.3. Interestingly, α increases with decreasing the ratio R/δ_B, where R is the radius of the magnetically soft regions inside the material and δ_B is the domain wall width given by Equation 7.4 [205]. Consequently, α can be enhanced with increasing the domain wall width, which in turn can be achieved by reducing the anisotropy constant K_u. The feasibility of this approach has been demonstrated by Balasubramanian et al. [206]. A permanent magnet material class possessing relatively low anisotropy constants K_u are hard ferrites. Accordingly, a hexaferrite, namely $SrAl_2Fe_{10}O_{19}$ (will be referred to as Al_2SrM further in the text), was chosen as the hard phase for the present study. Al_2SrM is an Al substituted Sr hexaferrite possessing an enhanced magnetic anisotropy field [207]. The condition $H_c \geq 1/2M_r$ [208] is satisfied which justifies its application as an additional high-remanence material.

The Al_2SrM powders were obtained in cooperation with Siemens AG Corporate Technology (BMBF KomMa project). The given magnetic properties are summarized in Table 7.1 with the respective $M(H)$

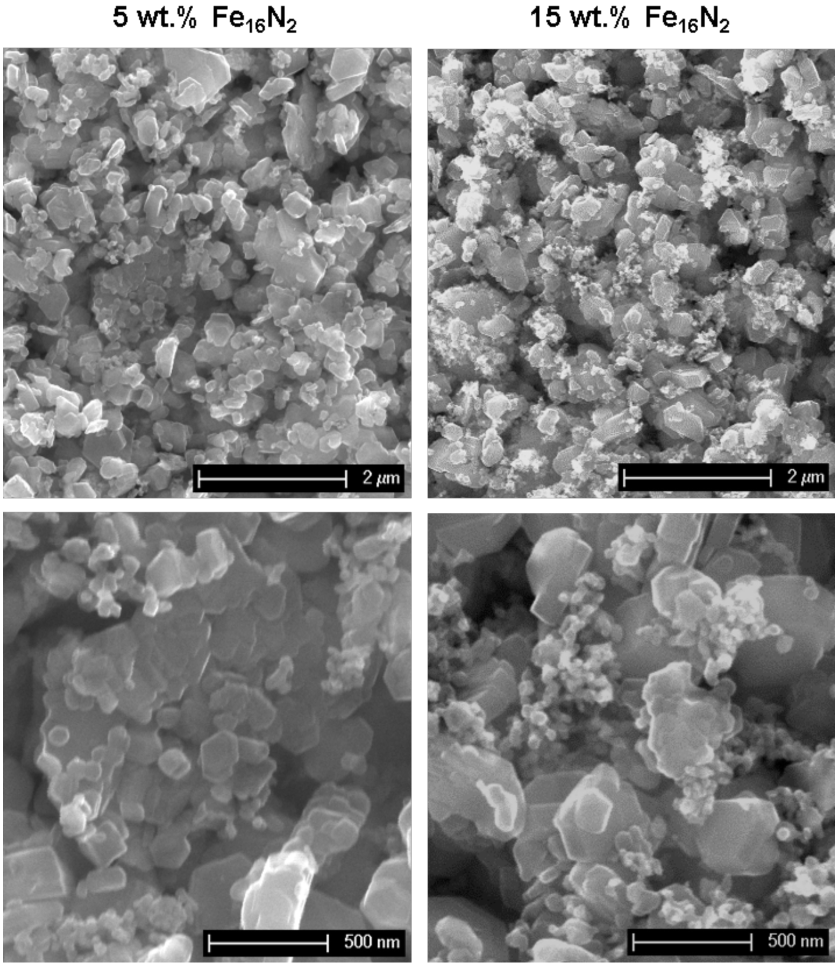

Figure 7.4: SEM images of Al_2SrM/α''-$Fe_{16}N_2$ powders with different fractions mixed by ball milling.

loop and microstructure presented in Figure 7.3b. The ferrite shows a wide hysteresis with a large H_c and a rather low M_s which should be improved by adding the high-magnetization α''-$Fe_{16}N_2$ phase. Given that the H_c can be maintained, this should result in an overall $(BH)_{max}$ improvement. The Al_2SrM powder consists of sub-micron plate-like particles with hexagonal shape.

Both α''-$Fe_{16}N_2$ and Al_2SrM powders were mixed using a SPEX mill with 2 mm steel balls, a ball-to-powder ratio of 5:1, in isopropanol for 60 min (samples were always handled in protective atmosphere). The added amount of α''-$Fe_{16}N_2$ nanoparticles was up to 15 wt.% in a steps of 5 wt.%. The resultant microstructures are presented in Figure 7.4. The amount of the fine α''-$Fe_{16}N_2$ particles increases and they are relatively evenly distributed within the Al_2SrM main material. Several larger agglomerates have not been completely dismembered by the milling procedure and are still present in the samples which is likely to result in a deteriorated magnetic performance. Further optimization was tried by using larger milling balls (higher kinetic energy) and longer milling times. The former lead to a mechanical damage of the Al_2SrM significantly reducing the magnetic properties, whereas the latter one had no observable impact on the final microstructures.

In order to produce bulk composite magnets, the above described powder mixtures were consolidated using a uni-axial hydraulic press with optical heating. The procedure is illustrated in Figure 7.5. Consid-

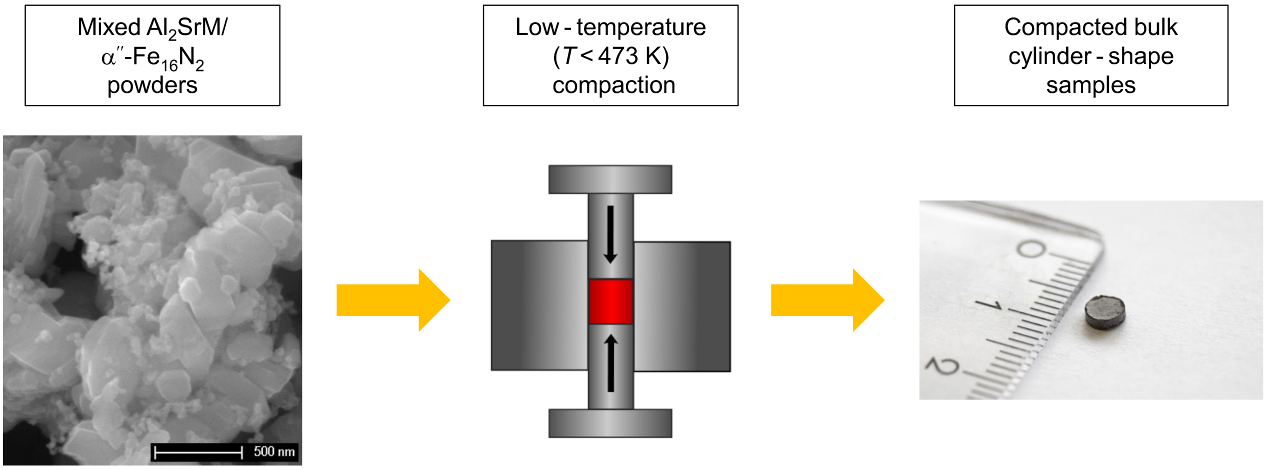

Figure 7.5: Consolidation of the mixed Al_2SrM/α''-$Fe_{16}N_2$ powders.

ering the thermal stability of the α''-$Fe_{16}N_2$ phase reported in Chapter 6, special care had to be taken to the compaction temperature as well as the atmosphere. A series of experiments in a temperature range of 403 K–463 K, a vacuum of 5×10^{-2} mbar were conducted (not shown here) and 403 K chosen as the optimum.

For the at 400 MPa, 403 K consolidated Al_2SrM/α''-$Fe_{16}N_2$ powders room temperature VSM $M(H)$ measurement results are summarized in Figure 7.6. As expected, the magnetization increases continuously with the α''-$Fe_{16}N_2$ concentration. After consolidation no decrease in magnetization can be observed which leads to the conclusion that α''-$Fe_{16}N_2$ is stable and not oxidizing at the pressing conditions. Most likely a passivizing oxide shell has formed already during the mixing stage.

A significant reduction in coercivity as a function of the α''-$Fe_{16}N_2$ concentration is observed, which drops even further after the compaction experiments. The hysteresis loops reveal a two-phase behavior, with the first shoulder in the demagnetization curve corresponding to a switching of the magnetically softer α''-$Fe_{16}N_2$ phase and the second one to the Al_2SrM. These results show that the presented route fails to achieve exchange-coupled nanocomposite magnets, and no $(BH)_{max}$ enhancement in the Al_2SrM/α''-$Fe_{16}N_2$ samples could be realized. Three main reasons for this are most likely:

- As shown in the forgoing chapter, the α''-$Fe_{16}N_2$ nanoparticles are prone to oxidation. It is therefore very likely that at the mixing stage they slightly reduce the Al_2SrM or accumulate oxygen from the environment and form oxide shells. This might compete with the exchange length, $l_0 = \sqrt{A/M_s^2}$ [169], and therefore the Al_2SrM/α''-$Fe_{16}N_2$ composites fail to yield single-phase $M(H)$ loops.

- Even despite the oxidation, the current α''-$Fe_{16}N_2$ nanoparticles are too coarse. According to Equation 7.4, the calculated critical particle dimensions for the soft phase (twice the domain wall width of the hard phase) in the case of Al_2SrM are roughly 32 nm. This is less than the $\approx$ 50 nm for the α''-$Fe_{16}N_2$ synthesized in this work.

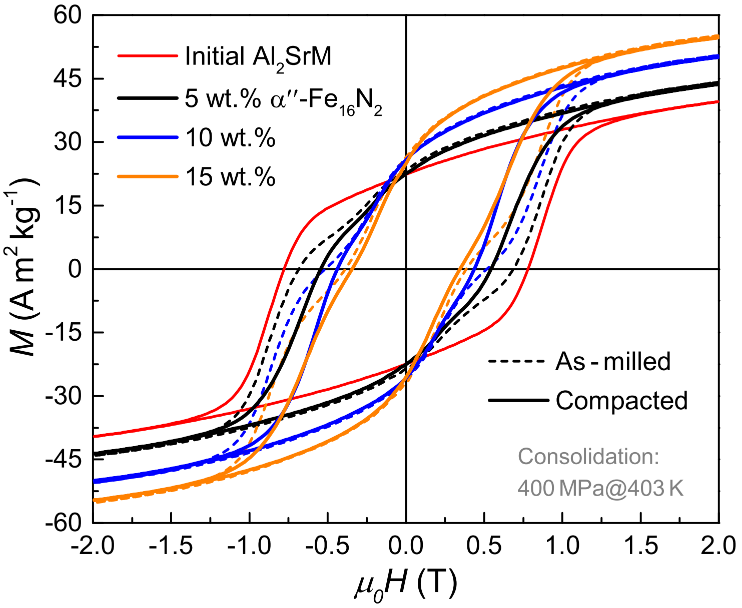

Figure 7.6: VSM results of the mixed (ball milled) and at 400 MPa, 403 K consolidated Al_2SrM/α''-$Fe_{16}N_2$ powders with various α''-$Fe_{16}N_2$ concentrations.

- A successful consolidation could not be realized under the conditions where α''-$Fe_{16}N_2$ is still stable. This is illustrated in Figure 7.7. At the low (403 K) temperature used for the consolidation experiments, diffusion is very limited and no significant sintering takes place which is visible in both, top area (a) as well as the fracture surface (b) micrographs. As a result, the consolidated end products are simply slightly pressed powders with high porosity, loose interfaces and poor mechanical stability. Consequently, no significant exchange-coupling on a nano-scale can be realized in such a state of aggregation.

Interestingly, the denominator term $K_h - K_s$ in Equation 7.4 cannot be used in the case of Al_2SrM/α''-$Fe_{16}N_2$ composites. The K_s (0.96 MJ m^{-3} for α''-$Fe_{16}N_2$) is actually larger than K_h (0.238 MJ m^{-3} for Al_2SrM) and thus would result in a negative number. Therefore, an estimation of the possibly larger critical dimensions for the semi-hard phase by this approach is not applicable for the current choice of materials. Numerical micromagnetic calculations could be beneficial and provide a useful insight here.

7.3 Magnetic nanoparticle hyperthermia

Cancer is among the leading causes of mortality worldwide [209]. Approximately 39.6 percent of the population will be diagnosed with cancer at some point during their lifetimes according to the National Cancer Institute [210].

Interestingly, cancerous tissues undergo cell death at temperatures higher than 43 °C [12] (or 42 °C–46 °C [182]) which opens a door for thermotherapy as a possible cancer treatment. However, in order to reduce the damage to normal tissue, targeted, local heating would be preferred. This can be realized by using magnetic nanoparticles that produce heat in response to an external alternating magnetic field

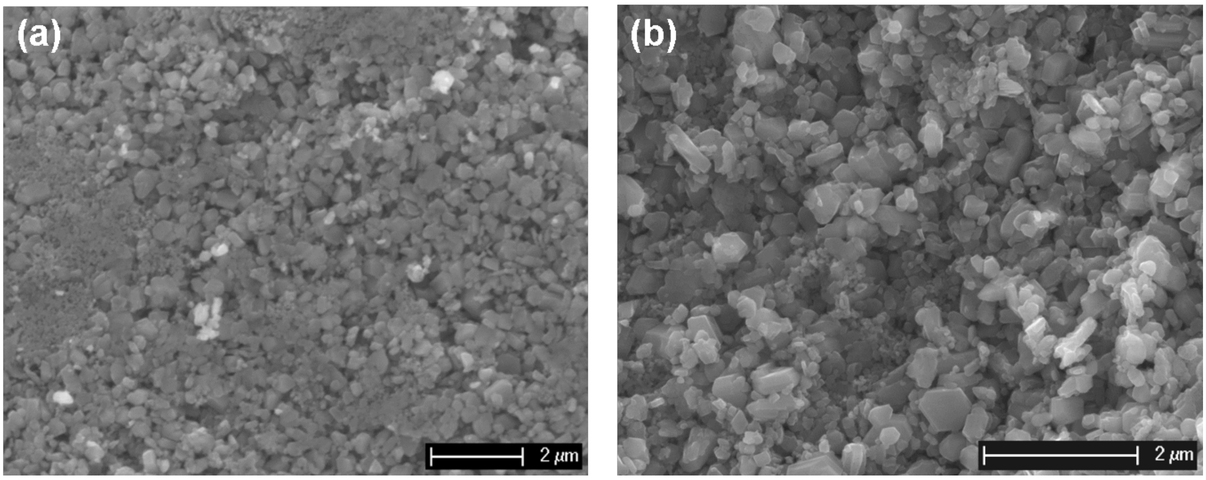

Figure 7.7: SEM images of a consolidated Al_2SrM/α''-$Fe_{16}N_2$ sample. (a) Top view and (b) fracture surface.

(due to frictional, hysteresis or eddy current losses) and are confined to the region of the cancerous tumor tissue. This way, the surrounding healthy tissue remains unaffected.

The nanoparticles for magnetic hyperthermia should ideally fulfill the following criteria:

- Contain no expensive or critical elements
- Biocompatible
- Posses appropriate magnetic properties in order to achieve good heating performance.

α''-$Fe_{16}N_2$ contains only iron and nitrogen, which are both cheap and abundant and thus would qualify for the first point. The second one seems straight-forward as neither Fe nor N are considered toxic or otherwise disturbing. At the same time, the high reactivity (see Chapter 6), at least unless the particles are coated with a protective shell, presents a significant obstacle and should be studied in more detail.

Concerning the magnetic properties, the common choice in magnetic nanoparticle hyperthermia is iron oxides, typically γ-Fe_2O_3 (maghemite) or Fe_3O_4 (magnetite) [211]. However, several theoretical studies [212, 213] have shown that in praxis achieving the required local heating effect might be difficult to realize and it requires large number of nanoparticles due to the high heat transfer in cells (contain mostly water). In this light, a novel material with an enhanced heating performance would be highly beneficial.

The dissipated heat power of a ferrofluid in a magnetic field can be expressed as [73]

$$P_H = \frac{\pi \mu_0^2 M_s^2 V H^2 f}{a k_B T} \frac{\omega \tau}{1 + (\omega \tau)^2}, \tag{7.5}$$

where V is the particle volume, H is the applied alternating magnetic field, f is the field frequency, ω is the angular frequency, a is a constant and τ the effective relaxation time. This shows that at a given set

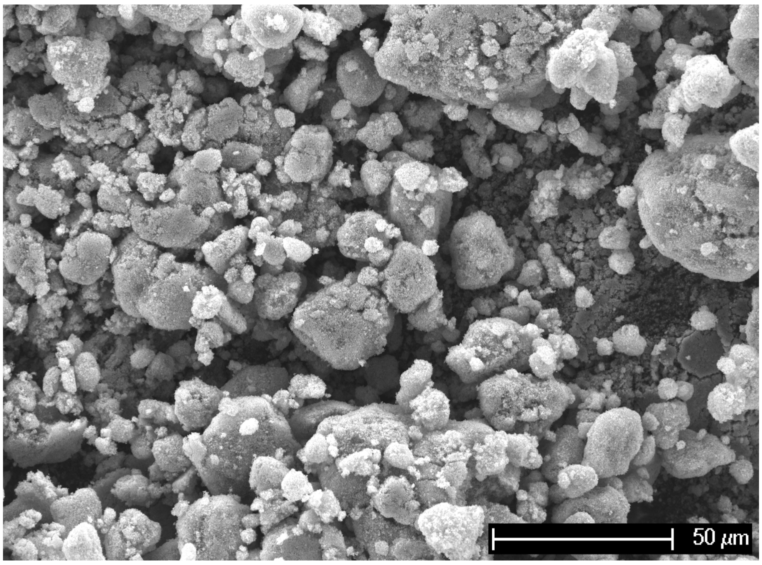

Figure 7.8: SEM image of the α''-$Fe_{16}N_2$ sample, showing pronounced agglomeration in micrometer-range particles.

of external parameters (applied field H, frequency f etc.), the way to enhance the heating performance is by maximizing the magnetization M_s of the nanoparticles. Since $P_H \sim M_s^2$, even a moderate increase in M_s would result in a remarkable improvement in the nanoparticle heating performance.

As shown in Figure 6.13, the α''-$Fe_{16}N_2$ nanoparticles possess much higher M_s than the Fe_2O_3 ($202\,Am^2kg^{-1}$ vs $70\,Am^2kg^{-1}$) and therefore could deliver a better heating performance.

Also, the metallic conductivity of the iron nitride particles in contrast to the insulating nature of the iron oxides could lead to additional heating losses due to eddy currents. However, eddy current losses in fine particles are shown to decrease with the particle size as d^2 [214] and as a result are negligible in the case of α''-$Fe_{16}N_2$ nanoparticles.

In order to investigate the heating performance, hyperthermia measurements were performed. The experiments were conducted with 1 mL nanoparticle dispersions in hexane prepared by sonication. A commercial AC magnetic field applicator (DM100, nanoScale Biomagnetics) with an optical fiber temperature probe located in the middle of the dispersions was used.

As evident from the SEM images (Figure 7.8), the α''-$Fe_{16}N_2$ nanoparticles are severely agglomerated, forming micrometer-sized structures which could not be destroyed with the ultrasonic finger sonicator. An agglomeration is present (not shown here) already in the initial γ-Fe_2O_3 nanoparticles and thus is not a consequence of the applied hydrogen reduction or nitrogenation treatments. TEM analysis (Figure 7.9) provides extra insight, showing formation of long α''-$Fe_{16}N_2$ nanoparticle chains due to magnetostatic interactions between the particles. Ideally, particles for biomedical applicatioins should posses negligible remanent magnetization M_r in order to minimize agglomeration in absence of external field. This can be realized in superparamagnetic particles. Magnetization of a ferromagnetic particles of small radius becomes unstable when the energy barrier KV (K being the anisotropy constant and V the particle volume) is comparable to thermal energy k_BT. A commonly used criterion for blocking is $KV/k_BT = 25$

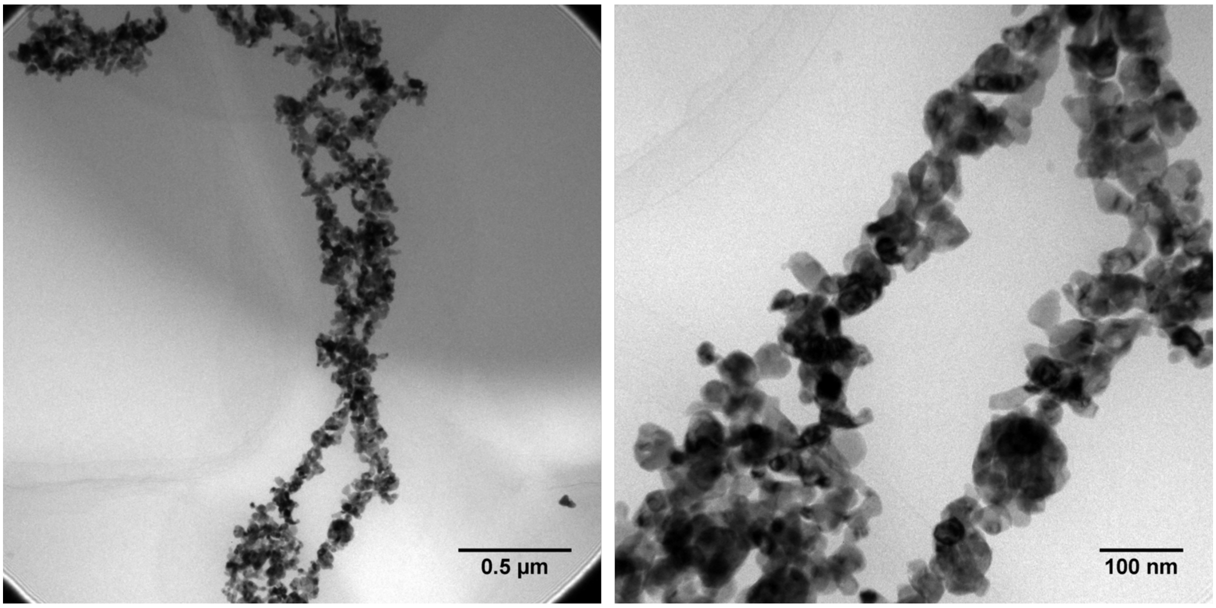

Figure 7.9: TEM images of the α''-$Fe_{16}N_2$ nanoparticles.

[5]. This leads to an expression for the critical superparamagnetic particle diameter (in the case of spherical particles):

$$D_{sp} = \sqrt[3]{\frac{6k_B T}{\pi K}} \cdot 25. \tag{7.6}$$

For the present iron nitride α''-$Fe_{16}N_2$, this would result in a particle size of ≈ 6 nm at 300 K. Obviously, the current particles are much larger and therefore possess a remanent magnetization and thus inevitably attract each other and form large structures. Consequently, a reasonable monodispersity as well as colloidal stability could not be achieved.

α''-$Fe_{16}N_2$ suspensions were prepared with concentrations of roughly $2\,mg\,mL^{-1}$ and used for the hyperthermia heating rate characterization. The measurement results are shown in Figure 7.10. The applied AC field was 0.025 T with a frequency of 402 kHz. The α''-$Fe_{16}N_2$ nanoparticles perform poorly compared to the precursor γ-Fe_2O_3 (same particle size and aggregation). Results of a commercial Fe_3O_4 dispersion (MAGNO, $2\,mg\,mL^{-1}$, nanoScale Biomagnetics) are given as a comparison. The results can be well understood by looking at the minor hysteresis loops of the α''-$Fe_{16}N_2$ nanoparticles as depicted in Figure 7.11a. The performance decreases rapidly with decreasing field. Below about 0.5 T the hysteresis loops become very narrow, which obviously results in significantly reduced M_s, H_c and hysteresis losses, respectively. The resultant minor hysteresis loops for both α''-$Fe_{16}N_2$ and γ-Fe_2O_3 nanoparticles at a maximum applied field similar to that used in the hyperthermia measurements (0.025 T) are shown in Figure 7.11b. The γ-Fe_2O_3 outperform the current α''-$Fe_{16}N_2$ nanoparticles under these conditions. Thus, the low M_s, H_c and area enclosed by the hysteresis loop explains the poor heating performance observed in the hyperthermia measurements.

Using higher fields will enhance the heat generated by α''-$Fe_{16}N_2$. This however has limitations imposed by the interaction of the AC magnetic field and the biological tissue (such as induced eddy currents).

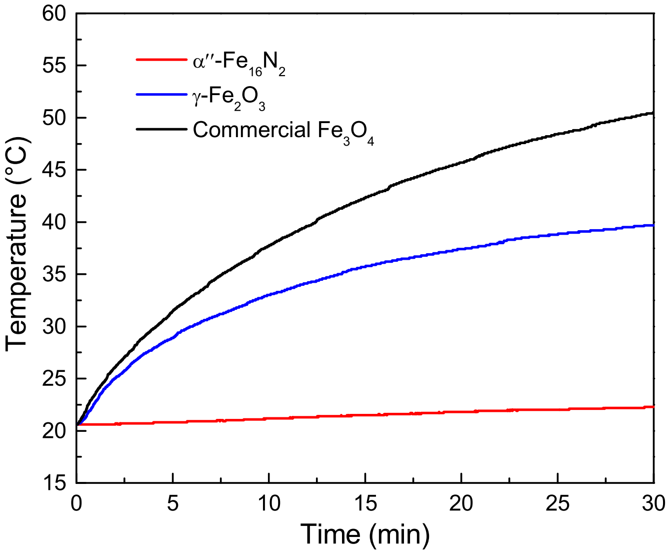

Figure 7.10: Hyperthermia measurements for the initial γ-Fe$_2$O$_3$ and in this work synthesized α''-Fe$_{16}$N$_2$ nanoparticles. The maximum applied field is $0.025\,\mathrm{T}$ and frequency $402\,\mathrm{kHz}$. A commercial Fe$_3$O$_4$ is shown as a comparison.

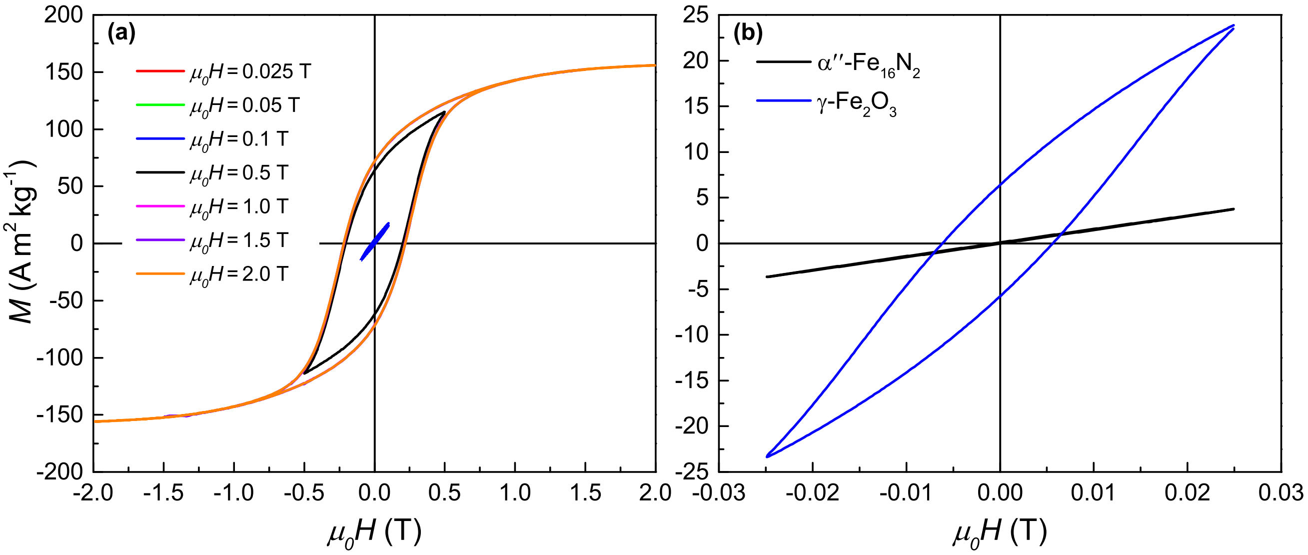

Figure 7.11: (a) Hysteresis loops at different maximum applied fields for α''-Fe$_{16}$N$_2$ nanoparticles. (b) Comparison of the minor loops with a maximum applied field corresponding to the hyperthermia measurement ($0.025\,\mathrm{T}$) for the γ-Fe$_2$O$_3$ and α''-Fe$_{16}$N$_2$ nanoparticles.

A commonly used reference here is known as the *Brezovich citerion* [211], which tells that the product $H \cdot f$ should not exceed $4.85 \times 10^8\,\mathrm{Am^{-1}s^{-1}}$. Therefore, moving towards high fields is limited.

To conclude, in principle due to the superior M_s compared to conventionally used iron oxides, α''-$Fe_{16}N_2$ could be a competitive material for magnetic hyperthermia. However, multiple challenges have to be tackled. Much finer particles need to be synthesized to reach the superparamagnetic limit at room temperature, hence minimizing the M_r and avoiding agglomeration. The hysteresis needs to be engineered so that the relatively high M_s can be transferred into higher heating power at the rather low magnetic fields used in hyperthermia therapy. Another important challenge remains the chemical stability of the α''-$Fe_{16}N_2$ nanoparticles.

7.4 Magnetic recording

Magnetic storage density in commercially available hard disks has doubled every one to two years with the disk drives continuously becoming smaller and faster [215, 216]. However, further development might be hampered due to thermal stability problems of the recorded bits caused by the recording medium approaching the superparamagnetic limit [217]. As the grain size decreases the magnetic anisotropy energy K_uV becomes comparable to the thermal energy k_BT. The criteria for maintaining good data storage signal stability at normal operating temperatures of about 340 K is

$$K_uV > C \cdot k_BT \tag{7.7}$$

with $C = 36$-60 for a storage time of ten years [218, 219, 5, 216, 73]. For example, a spherical $CoCr_{20}Pt_{15}$ alloy ($K_1 = 0.25\,\mathrm{MJ\,m^{-3}}$ [73]) should not be operated below a grain size of $\approx 13\,\mathrm{nm}$ according to Equation 7.7. Decreasing the bit size requires a material with larger K_u. In comparison, the α'-Fe_8N films showed a $K_u = 0.54\,\mathrm{MJ\,m^{-3}}$ and the ordered α''-$Fe_{16}N_2$ is reported to possess $K_u = 0.96\,\mathrm{MJ\,m^{-3}}$ [20], which is also in a reasonable agreement with the anisotropy field measurement results presented in this work (see Chapter 6). This would in principle enable a further recording media size reduction to about 10 nm for α' and 8 nm for α'' respectively. Due to the high uniaxial anisotropy, Fe_8N could perhaps also be interesting for perpendicular magnetic recording media. However, as the $M_s \gg H_c$ the material is likely to demagnetize 'in the bit' [215]. Other hard magnetic phases, such as FePt or CoPt, possess even larger K_u and thus could lead to much higher areal densities. Consequently, the write field required to switch the magnetization would also have to be considerably increased. This competition between thermal stability, write-ability and read-ability is known as the "trilemma" of magnetic recording [220, 221, 222]. The write field can be expressed as [216]

$$H_w \approx \frac{K_u}{M_s}. \tag{7.8}$$

Relation 7.8 shows that the write field can be reduced by using a material with high magnetization. With this in mind, the α'-Fe_8N/α''-$Fe_{16}N_2$ system has a significant advantage compared to other high anisotropy phases such as FePt or CoPt, namely the high M_s. In Chapter 5 the μ_0M_s for α'-Fe_8N reached

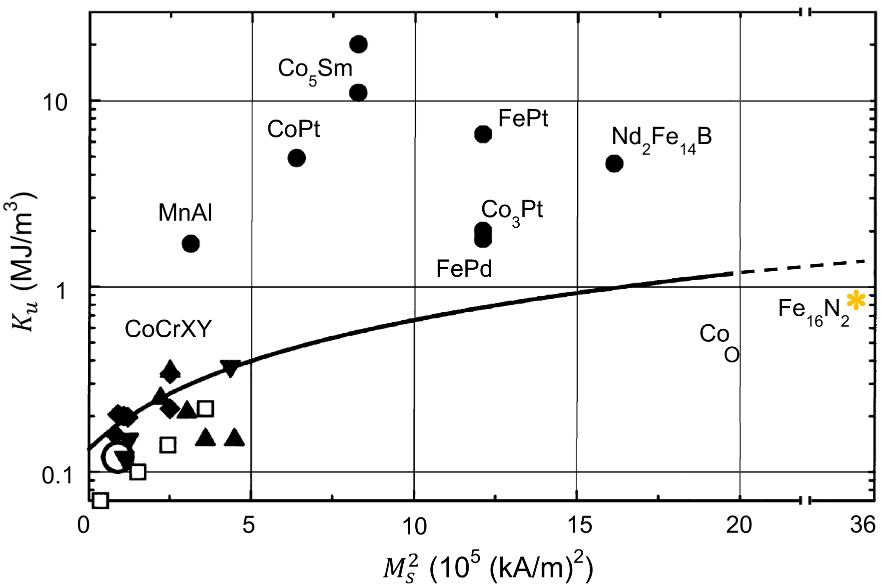

Figure 7.12: Recording stability boundary (for 0.51 T write field) plot for various materials used in magnetic recording. α''-Fe$_{16}$N$_2$ is positioned at the very high M_s^2 side and below the stability line (adapted from [219]).

$\approx 2.4\,\mathrm{T} \pm 0.09\,\mathrm{T}$ at 10 K. This is much higher than 1.43 T for FePt, for example. However, as appealing as it might seem, the M_s for α'-Fe$_8$N/α''-Fe$_{16}$N$_2$ is actually too high at the given K_u for achieving stable magnetic recording. This is illustrated in Figure 7.12. Optimal materials should lie in the vicinity of the stability boundary line. Alloys above have too high anisotropy and therefore are not writable, whereas the ones below the line do not maintain stability. α''-Fe$_{16}$N$_2$ is positioned far to the right with $M_s^2 \approx 36 \times 10^5\,(\mathrm{kA/m})^2$ and below the stability boundary indicating that the demagnetization fields would potentially destabilize the bit patterns.

A conceptually interesting idea for application of α'-Fe$_8$N$_x$/α''-Fe$_{16}$N$_2$ system could be in *graded media*. As already discussed, the ever-reducing bit dimensions lead to a dilemma. On one hand the anisotropy energy density K_u has to be maximized in order to maintain good thermal stability of the stored information over extended periods of time despite the competition with the thermal energy $k_B T$ when length scales approach the superparamagnetic limit. On the other hand higher K_u leads to enhanced nucleation field and coercivity, respectively, which is not accessible with the state-of-the-art write heads. One possible loophole is the concept of composite or exchange-spring media. The principal phenomenon is in analogy to the previously discussed nanocomposite magnets. By exchange-coupling a magnetically hard (e.g. FePt) layer with a soft (e.g. FeRh) layer [223] it is possible to reduce the coercivity of the composite by a factor of five without compromising the thermal stability [224].

Micromagnetic simulations show that both soft and hard layers should ideally possess similar magnetizations in order to maximize the thermal stability [224]. Moreover, another very interesting effect observed by Suess [224] is that the pinning field and the respective coercivity become smaller with increasing the number of layers. For example, a four-layer structure would result in only 1/13 H_c of the hardest layer.

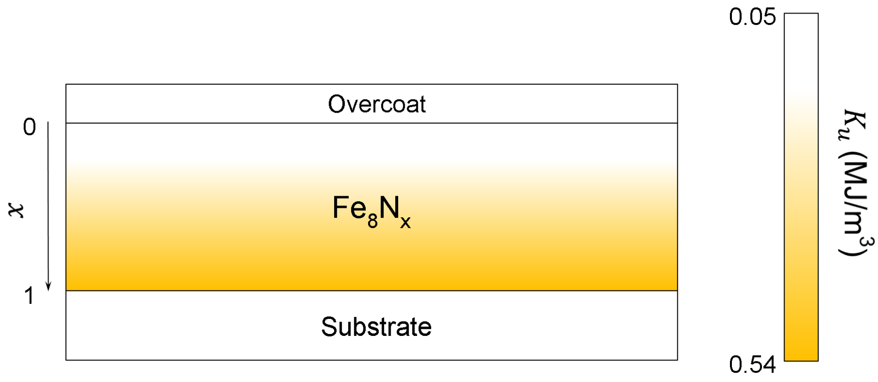

Figure 7.13: Schematic illustration of the composite exchange-spring media for α'-Fe_8N_x. The anisotropy K_u can be continuously adjusted from magnetically soft (pure α-Fe, $x = 0$) to hard ($x = 1$) by varying the nitrogen content.

This phenomena has been discussed also in context of the Brown's paradox [225] mentioned earlier in regard to the limited coercivity in permanent magnets.

In Chapter 5 it was shown that α'-Fe_8N_x thin films can be fabricated in the full range of $0 \leq x \leq 1$. The nitrogen incorporation led to a gradual increase in K_u, from a purely soft α-Fe ($x = 0$) to a significantly enhanced $K_u = 0.54\,\mathrm{MJ\,m^{-3}}$ at $x = 1$. The volume magnetization changed only slightly. Thus, this could be a suitable system for realizing the exchange-spring media. A possible film structure is illustrated schematically in Figure 7.13. Sputtering process would have to be performed with gradually changing the nitrogen concentration in the plasma gas. By this, a continuous film with a gradually variable anisotropy could be realized. Using diverse magnetic materials with different unit cell parameters for the individual soft and hard regions raise questions about the interface quality. However, as the in-plane lattice constant changes only slightly (see Table 5.1) within the α'-Fe_8N_x series, the epitaxial film growth would be coherent, without significant interface defects and crystallographic orientation changes across the entire stack. The whole process could be done uninterruptedly and with a single elemental target instead of having to switch materials for the hard and soft layers respectively.

An obstacle for using α'-Fe_8N/α''-$Fe_{16}N_2$ in magnetic recording media might be the poor chemical stability of the compounds. In the case of bulk matter, several nanometers of surface oxidation is not really an issue, whereas for the miniaturized data storage structures with an average grain size of about 10 nm it plays crucial role and is not tolerable. This can in principle be solved by depositing an additional protective capping layer. Carbon overcoats and a lubricant layers are used in conventional recording systems [216]. Therefore, no additional architecture design would be necessary here.

8 Conclusions and outlook

In this thesis, the iron nitride Fe_8N_x material synthesis, an analysis of structure, phase stability and the corresponding magnetic properties are presented. The focus lies on thin films and nanoparticles. By performing advanced synthesis and in-depth characterization of Fe_8N_x samples in a phase-pure form, it was possible to study the fundamental properties as well as the feasibility for the proposed applications. Two cases were distinguished - when the N atom occupation is random (α'-Fe_8N_x) and when the N atoms occupy specific interstitial sites in an ordered manner (α''-$Fe_{16}N_2$).

In the first part of this work α-Fe, γ'-Fe_4N and α'-Fe_8N_x thin films have been grown epitaxially onto a MgO (001) substrates by RF magnetron sputtering. Despite the amount of research dedicated to synthesis and characterization of α'-Fe_8N and α''-$Fe_{16}N_2$ phases within the last decades, even the intrinsic magnetic properties are still unclear and debated within the magnetism community. Therefore, pure α-Fe and the well understood γ'-Fe_4N were used as a reference materials in order to assess the reliability of the employed characterization techniques and henceforth exclude possible errors in interpretation of the magnetic properties for the studied Fe-N phases.

The nitrogen incorporation in α'-Fe_8N_x lead to a gradually increased tetragonal unit cell expansion of the compounds reaching $c/a = 1.1$. The average magnetic moment per iron was found to scale with the lattice expansion, reaching $2.50\,\mu_B \pm 0.09\,\mu_B$ per Fe atom at 10 K. This corresponds to an increase as compared to α-Fe of about 12.6 %. Within the measurement error this is in agreement with the majority of theoretically predicted and experimental values reported in literature. The origin of the increased magnetic moment is attributed to the magnetovolume effect. Along with the increase in magnetic moment also a progressive development of a uniaxial anisotropy component along the out-of-plane direction was observed for α'-Fe_8N_x thin films. By combining experimental and theoretical studies, the occurrence of the enhanced uniaxial magnetic anisotropy has been explained. The results suggest that the interstitial N atoms play a decisive role in stabilizing the PMA due to anisotropy in orbital moments along the different crystallographic directions in the Fe atoms directly above and below N.

The second part of the thesis explores synthesis and characterization of phase-pure α''-$Fe_{16}N_2$ nanoparticles. A comprehensive analysis of the structure, elemental composition, thermal stability, electronic, and magnetic properties of the samples has been conducted. The α''-$Fe_{16}N_2$ nanoparticles showed semi-hard magnetic properties with magnetization at 0 K of $M_s(0) = 215\,\mathrm{Am^2kg^{-1}}$ and coercivity $\mu_0 H_c = 0.22\,\mathrm{T}$. The M_s is lower than the "giant" values found in literature, but slightly higher than the precursor α-Fe which agrees well with the theoretical predictions and mainstream opinions within the scientific community. Under inert atmosphere α''-$Fe_{16}N_2$ nanoparticles are stable up to roughly 463 K whereas in air already at around 433 K oxidation takes place. Considering, for example, conventional sintering temperatures, this clearly indicates the complications regarding production of high quality, dense, bulk α''-$Fe_{16}N_2$ material. The samples are overall very sensitive to oxidation. Microscopy results demonstrate that the outer surface of the nanoparticles is oxidizing when exposed to air and formation of Fe-O shells could be the reason for the decreased magnetization at ambient conditions.

The last part of the thesis correlates the results presented in the different foregoing chapters with the potential Fe_8N_x applications. Fe_8N_x is an unique material possessing both, high magnetization together with a decent magnetic hardness. Nevertheless, in many cases the anisotropy is insufficient for a hard magnet and too high for soft magnet applications. The anisotropy field H_a was shown to be too low for realizing satisfactory coercivities in rare-earth-free permanent magnets, unless the shape anisotropy contribution is utilized constructively. α''-$Fe_{16}N_2$ could potentially be interesting for hard-soft composite systems, although special care should be exercised to the phase stability and the resultant oxide layer which might reduce the efficient exchange. Regarding the magnetic hyperthermia, much finer particles need to be synthesized to reach the superparamagnetic limit at room temperature. The hysteresis needs to be engineered so that the relatively high M_s can be transferred into enhanced heating power at the magnetic fields used in hyperthermia therapy. An ongoing challenge remains the thermal and chemical stability of the α''-$Fe_{16}N_2$ nanoparticles.

In the case of thin films and nanoparticles, surface, interface as well as oxidation effects cannot be ruled out. Ideally, bulk single-crystal samples would be preferred for proper future studies of the long-debated controversial magnetic properties of Fe_8N_x. This can be tried by starting from α-Fe single-crystals and performing, for example, magnetic field-assisted nitrogenation experiments. Yet, considering the sluggish diffusion of nitrogen in iron at low temperatures as well as energetically much more preferable formation of the competing phases, this appears to be a very challenging assignment.

Bibliography

[1] S. Desheng and L. Guodong, *History of Electromagnetism* (Popular Press Publishers, Guang Xi, 1987).

[2] H. Orsted, K. Jelved, A. Jackson, O. Knudsen, and A. Wilson, *Selected Scientific Works of Hans Christian Orsted* (Princeton University Press, 1998), No. 1.

[3] D. Jiles, *Introduction to Magnetism and Magnetic Materials* (CRC Press, 2015).

[4] IPCC, 2014: Climate Change 2014: Synthesis Report. Contribution of Working Groups I, II and III to the Fifth Assessment Report of the Intergovernmental Panel on Climate Change [Core Writing Team, R.K. Pachauri and L.A. Meyer (eds.)]. IPCC, Geneva, Switzerland.

[5] J. M. D. Coey, *Magnetism and Magnetic Materials* (Cambridge University Press, 2010).

[6] J. D. Livingston, JOM **42**, 30 (1990).

[7] O. Gutfleisch, M. A. Willard, E. Brück, C. H. Chen, S. G. Sankar, and J. P. Liu, Adv. Mater. **23**, 821 (2011).

[8] K. Bourzac, Technol. Rev. **114**, 58 (2011).

[9] M. D. Kuz'min, K. P. Skokov, H. Jian, I. Radulov, and O. Gutfleisch, J. Phys.: Condens. Matter **26**, 064205 (2014).

[10] J. Coey, Scr. Mater. **67**, 524 (2012).

[11] K. M. Krishnan, A. B. Pakhomov, Y. Bao, P. Blomqvist, Y. Chun, M. Gonzales, K. Griffin, X. Ji, and B. K. Roberts, J. Mater. Sci. **41**, 793 (2006).

[12] A. K. Gupta and M. Gupta, Biomaterials **26**, 3995 (2005).

[13] T. K. Jain, M. A. Morales, S. K. Sahoo, D. L. Leslie-Pelecky, and V. Labhasetwar, Mol. Pharmaceutics **2**, 194 (2005).

[14] S. Mornet, S. Vasseur, F. Grasset, and E. Duguet, J. Mater. Chem. **14**, 2161 (2004).

[15] R. Hergt, W. Andra, C. G. d'Ambly, I. Hilger, W. A. Kaiser, U. Richter, and H. G. Schmidt, IEEE Trans. Magn. **34**, 3745 (1998).

[16] A. J. Giustini, A. A. Petryk, S. M. Cassim, J. A. Tate, I. Baker, and P. J. Hoopes, Nano LIFE **01**, 17 (2010).

[17] H. Mamiya, J. Nanomaterials **2013**, 752973 (2013).

[18] T. K. Kim and M. Takahashi, Appl. Phys. Lett. **20**, 492 (1972).

[19] H. Takahashi, M. Igarashi, A. Kaneko, H. Miyajima, and Y. Sugita, IEEE Trans. Magn. **35**, 2982 (1999).

[20] T. Ogawa, Y. Ogata, R. Gallage, N. Kobayashi, N. Hayashi, Y. Kusano, S. Yamamoto, K. Kohara, M. Doi, M. Takano, and M. Takahashi, Appl. Phys. Express **6**, 073007 (2013).

[21] K. Takagi, M. Akada, K. Ozaki, N. Kobayashi, T. Ogawa, Y. Ogata, and M. Takahashi, J. Appl. Phys. **115**, (2014).

[22] Y. Jiang, J. Liu, P. K. Suri, G. Kennedy, N. N. Thadhani, D. J. Flannigan, and J.-P. Wang, Adv. Eng. Mater. **18**, 1009 (2016).

[23] T. Ogi, Q. Li, S. Horie, A. Tameka, T. Iwaki, and K. Okuyama, Adv. Powder Technol. **27**, 2520 (2016).

[24] R. Skomski, G. C. Hadjipanayis, and D. J. Sellmyer, J. Appl. Phys. **105**, (2009).

[25] Y. Sasaki, N. Usuki, K. Matsuo, and M. Kishimoto, IEEE Trans. Magn. **41**, 3241 (2005).

[26] Y. Namiki, T. Fuchigami, N. Tada, R. Kawamura, S. Matsunuma, Y. Kitamoto, and M. Nakagawa, Acc. Chem. Res. **44**, 1080 (2011).

[27] M. Takahashi and H. Shoji, J. Magn. Magn. Mater. **208**, 145 (2000).

[28] M. Coey, Phys. World **6**, 25 (1993).

[29] R. M. Brown, *Sudden Death* (Bantam, 1983).

[30] I. Dirba, M. B. Yazdi, A. Radetinac, P. Komissinskiy, S. Flege, O. Gutfleisch, and L. Alff, J. Magn. Magn. Mater. **379**, 151 (2015).

[31] I. Dirba, P. Komissinskiy, O. Gutfleisch, and L. Alff, J. Appl. Phys. **117**, (2015).

[32] H. Zhang, I. Dirba, T. Helbig, L. Alff, and O. Gutfleisch, APL Mater. **4**, (2016).

[33] I. Dirba, C. A. Schwöbel, L. V. B. Diop, M. Duerrschnabel, L. Molina-Luna, K. Hofmann, P. Komissinskiy, H.-J. Kleebe, and O. Gutfleisch, Acta Mater. **123**, 214 (2017).

[34] A. Machlet, Treatment of steel, iron, &c., 1913, US Patent 1,065,379.

[35] A. Fry, Process for hardening steel alloys, 1924, US Patent 1,487,554.

[36] E. Mittemeijer, in *ASM Handbook, Volume 4A, Steel Heat Treating Fundamentals and Processes*, edited by J. Dossett and G. Totten (ASM International, 2013), Vol. 4A, pp. 619–646.

[37] L. J. Dijkstra, Trans. AIME **185**, 252 (1949).

[38] V. Paranjpe, M. Cohen, M. Bever, and C. Floe, Trans. AIME **188**, 261 (1950).

[39] K. H. Jack, Acta Cryst. **5**, 404 (1952).

[40] K. H. Jack, Proc. R. Soc. London A **195**, 34 (1948).

[41] K. H. Jack, Proc. R. Soc. A **208**, 200 (1951).

[42] J. Fast and M. Verrijp, Acta Metall. **3**, 203 (1955).

[43] T. Takahashi and W. A. Bassett, Science **145**, 483 (1964).

[44] M. A. Werner Pepperhoff, *Constitution and Magnetism of Iron and its Alloys* (Springer Berlin Heidelberg, 2001).

[45] S. Ohba, Y. Saito, and Y. Noda, Acta Crystallogr. Sect. A **38**, 725 (1982).

[46] H.-K. Mao, W. A. Bassett, and T. Takahashi, J. Appl. Phys. **38**, 272 (1967).

[47] K. H. Jack, Proc. R. Soc. London A **208**, 216 (1951).

[48] J. D. Fast, *Interaction of Metals and Gases: Kinetics and Mechanisms* (Macmillan, 1971), Vol. 2.

[49] H. Jacobs, D. Rechenbach, and U. Zachwieja, J. Alloys Compd. **227**, 10 (1995).

[50] D. M. Roy and D. G. Pettifor, J. Phys. F: Met. Phys. **7**, L183 (1977).

[51] M. van Schilfgaarde, I. A. Abrikosov, and B. Johansson, Nature 46 (1999).

[52] H. C. Herper, E. Hoffmann, and P. Entel, Phys. Rev. B **60**, 3839 (1999).

[53] H. Wang, P.-W. Ma, and C. H. Woo, Phys. Rev. B **82**, 144304 (2010).

[54] A. Sakuma, J. Phys. Soc. Jpn. **60**, 2007 (1991).

[55] S. F. Matar, G. Demazeau, and B. Siberchicot, IEEE Trans. Magn. **26**, 60 (1990).

[56] S. Kokado, N. Fujima, K. Harigaya, H. Shimizu, and A. Sakuma, Phys. Rev. B **73**, 172410 (2006).

[57] A. Narahara, K. Ito, T. Suemasu, Y. K. Takahashi, A. Ranajikanth, and K. Hono, Appl. Phys. Lett. **94**, (2009).

[58] E. L. P. y. Blancá, J. Desimoni, N. E. Christensen, H. Emmerich, and S. Cottenier, Phys. Status Solidi B **246**, 909 (2009).

[59] J. Q. Xiao and C. L. Chien, Appl. Phys. Lett. **64**, 384 (1994).

[60] S. Atiq, H.-S. Ko, S. A. Siddiqi, and S.-C. Shin, J. Appl. Phys. **92**, (2008).

[61] K. Ito, G. H. Lee, K. Harada, M. Suzuno, T. Suemasu, Y. Takeda, Y. Saitoh, M. Ye, A. Kimura, and H. Akinaga, Appl. Phys. Lett. **98**, (2011).

[62] G. Shirane, W. J. Takei, and S. L. Ruby, Phys. Rev. **126**, 49 (1962).

[63] B. C. Frazer, Phys. Rev. **112**, 751 (1958).

[64] H. Xiang, F.-Y. Shi, M. S. Rzchowski, P. M. Voyles, and Y. A. Chang, J. Appl. Phys. **109**, (2011).

[65] G. K. Williamson and R. E. Smallman, Acta Crystallogr. **6**, 361 (1953).

[66] L. Cheng, A. Böttger, T. de Keijser, and E. Mittemeijer, Scr. Metall. Mater. **24**, 509 (1990).

[67] P. Weiss, J. Phys. Theor. Appl. **6**, 661 (1907).

[68] V. Moruzzi, J. Janak, and A. Williams, *Calculated Electronic Properties of Metals* (Pergamon, 1978).

[69] R. Pauthenet, J. Appl. Phys. **53**, 8187 (1982).

[70] A. Sommerfeld and H. Bethe, in *Aufbau Der Zusammenhängenden Materie* (Springer Berlin Heidelberg, 1933), pp. 333–622.

[71] J. C. Slater, J. Appl. Phys. **8**, 385 (1937).

[72] L. Pauling, Phys. Rev. **54**, 899 (1938).

[73] K. M. Krishnan, *Fundamentals and Applications of Magnetic Materials* (Oxford University Press, 2016).

[74] V. L. Moruzzi, P. M. Marcus, and P. C. Pattnaik, Phys. Rev. B **37**, 8003 (1988).

[75] V. L. Moruzzi and P. M. Marcus, Phys. Rev. B **38**, 1613 (1988).

[76] K. Mitsuoka, H. Miyajima, H. Ino, and S. Chikazumi, J. Phys. Soc. Jpn. **53**, 2381 (1984).

[77] I. M. L. Billas, J. A. Becker, A. Châtelain, and W. A. de Heer, Phys. Rev. Lett. **71**, 4067 (1993).

[78] F. J. Himpsel, Phys. Rev. Lett. **67**, 2363 (1991).

[79] C. D. Graham, Phys. Rev. **112**, 1117 (1958).

[80] H. Gengnagel and U. Hofmann, Phys. Status Solidi B **29**, 91 (1968).

[81] G. M. Kalvius and R. S. Tebble, *Experimental Magnetism* (Wiley-VCH Verlag GmbH & Co. KGaA, Weinheim, 1980), No. 1.

[82] P. Bruno, in *Magnetismus von Festkörpern und grenzflächen*, edited by P. G. P.H. Dederichs and W. Zinn (Forschungszentrum Jülich, 1993).

[83] T. Burkert, L. Nordström, O. Eriksson, and O. Heinonen, Phys. Rev. Lett. **93**, 027203 (2004).

[84] T. Burkert, O. Eriksson, P. James, S. I. Simak, B. Johansson, and L. Nordström, Phys. Rev. B **69**, 104426 (2004).

[85] H. J. Neuhäuser and W. Pitsch, Phys. Status Solidi A **19**, K7 (1973).

[86] N. Ji, M. S. Osofsky, V. Lauter, L. F. Allard, X. Li, K. L. Jensen, H. Ambaye, E. Lara-Curzio, and J.-P. Wang, Phys. Rev. B **84**, 245310 (2011).

[87] W. Dürr, M. Taborelli, O. Paul, R. Germar, W. Gudat, D. Pescia, and M. Landolt, Phys. Rev. Lett. **62**, 206 (1989).

[88] M. Komuro, Y. Kozono, M. Hanazono, and Y. Sugita, J. Appl. Phys. **67**, 5126 (1990).

[89] Y. Sugita, K. Mitsuoka, M. Komuro, H. Hoshiya, Y. Kozono, and M. Hanazono, J. Appl. Phys. **70**, 5977 (1991).

[90] Y. Sugita, H. Takahashi, M. Komuro, K. Mitsuoka, and A. Sakuma, J. Appl. Phys. **76**, 6637 (1994).

[91] Y. Sugita, H. Takahashi, M. Komuro, M. Igarashi, R. Imura, and T. Kambe, J. Appl. Phys. **79**, 5576 (1996).

[92] R. Coehoorn, G. H. O. Daalderop, and H. J. F. Jansen, Phys. Rev. B **48**, 3830 (1993).

[93] M. Takahashi, H. Shoji, H. Takahashi, H. Nashi, T. Wakiyama, M. Doi, and M. Matsui, J. Appl. Phys. **76**, 6642 (1994).

[94] J. M. D. Coey, K. O'Donnell, Q. Qinian, E. Touchais, and K. H. Jack, J. Phys.: Condens. Matter **6**, L23 (1994).

[95] J. M. D. Coey, J. Appl. Phys. **76**, 6632 (1994).

[96] M. Takahashi, H. Takahashi, H. Nashi, H. Shoji, T. Wakiyama, and M. Kuwabara, J. Appl. Phys. **79**, 5564 (1996).

[97] K. Nakajima and S. Okamoto, Appl. Phys. Lett. **56**, 92 (1990).

[98] A. Sakuma, J. Magn. Magn. Mater. **102**, 127 (1991).

[99] S. Matar, Z. Phys. B. Con. Mat. **87**, 91 (1992).

[100] H. Sims, W. H. Butler, M. Richter, K. Koepernik, E. Şaşıoğlu, C. Friedrich, and S. Blügel, Phys. Rev. B **86**, 174422 (2012).

[101] L. Ke, K. D. Belashchenko, M. van Schilfgaarde, T. Kotani, and V. P. Antropov, Phys. Rev. B **88**, 024404 (2013).

[102] N. Ji, L. F. Allard, E. Lara-Curzio, and J.-P. Wang, Appl. Phys. Lett. **98**, (2011).

[103] M. Abdellateef, C. Heiden, H. Lemke, F. El-Hossary, and K. Baerner, J. Magn. Magn. Mater. **256**, 214 (2003).

[104] H. Takahashi, K. Mitsuoka, M. Komuro, and Y. Sugita, J. Appl. Phys. **73**, 6060 (1993).

[105] M. Yang, L. F. Allard, N. Ji, X. Zhang, G.-H. Yu, and J.-P. Wang, Appl. Phys. Lett. **103**, (2013).

[106] T. Weber, L. de Wit, F. Saris, and P. Schaaf, Thin Solid Films **279**, 216 (1996).

[107] M. Q. Huang, W. E. Wallace, S. Simizu, A. T. Pedziwiatr, R. T. Obermyer, and S. G. Sankar, J. Appl. Phys. **75**, 6574 (1994).

[108] Y. Jiang, M. A. Mehedi, E. Fu, Y. Wang, L. F. Allard, and J.-P. Wang, Sci. Rep. **6**, (2016).

[109] Y. Jiang, V. Dabade, L. F. Allard, E. Lara-Curzio, R. James, and J.-P. Wang, Phys. Rev. Applied **6**, 024013 (2016).

[110] M. Widenmeyer, L. Shlyk, A. Senyshyn, R. Mönig, and R. Niewa, Z. Anorg. Allg. Chem. **641**, 348 (2015).

[111] E. Kita, K. Shibata, H. Yanagihara, Y. Sasaki, and M. Kishimoto, J. Magn. Magn. Mater. **310**, 2411 (2007).

[112] C. A. Bridges, O. Rios, L. F. Allard, H. M. Meyer, A. Huq, Y. Jiang, J.-P. Wang, and M. P. Brady, Phys. Chem. Chem. Phys. **18**, 13010 (2016).

[113] B. I. Min, Phys. Rev. B **46**, 8232 (1992).

[114] S. Ishida and K. Kitawatase, J. Magn. Magn. Mater. **104**, 1933 (1992).

[115] G. W. Fernando, R. E. Watson, M. Weinert, A. N. Kocharian, A. Ratnaweera, and K. Tennakone, Phys. Rev. B **61**, 375 (2000).

[116] M. Widenmeyer, T. C. Hansen, and R. Niewa, Z. Anorg. Allg. Chem. **639**, 2851 (2013).

[117] A. Sakuma, J. Appl. Phys. **79**, 5570 (1996).

[118] H. Takahashi, M. Komuro, K. Mitsuoka, Y. Sugita, T. Kobayashi, and E. Kita, J. Magn. Soc. Jpn. **19**, 353 (1995).

[119] M. D. Kuz'min, Phys. Rev. Lett. **94**, 107204 (2005).

[120] D. Bierwagen, Masters thesis, TU Darmstadt, 2009.

[121] X. Bao, R. M. Metzger, and M. Carbucicchio, J. Appl. Phys. **75**, 5870 (1994).

[122] A. Nagatomi, S. Kikkawa, T. Hinomura, S. Nasu, and F. Kanamaru, J. Jpn. Soc. Powder Powder Metal. **46**, 151 (1999).

[123] S. Kikkawa, K. Kubota, and T. Takeda, J. Alloys Compd. **449**, 7 (2008).

[124] S. Kikkawa, A. Yamada, Y. Masubuchi, and T. Takeda, Mater. Res. Bull. **43**, 3352 (2008).

[125] S. Yamashita, Y. Masubuchi, Y. Nakazawa, T. Okayama, M. Tsuchiya, and S. Kikkawa, J. Solid State Chem. **194**, 76 (2012).

[126] T. Ogi, A. B. Dani Nandiyanto, Y. Kisakibaru, T. Iwaki, K. Nakamura, and K. Okuyama, J. Appl. Phys. **113**, (2013).

[127] R. Zulhijah, A. B. Dani Nandiyanto, T. Ogi, T. Iwaki, K. Nakamura, and K. Okuyama, Nanoscale **6**, 6487 (2014).

[128] R. Zulhijah, A. B. D. Nandiyanto, T. Ogi, T. Iwaki, K. Nakamura, and K. Okuyama, J. Magn. Magn. Mater. **381**, 89 (2015).

[129] D. Nagai, Y. Kinemuchi, K. Suzuki, A. Towata, and M. Yasuoka, J. Solid State Chem. **225**, 455 (2015).

[130] I. Diakonov, I. Khodakovsky, J. Schott, and E. Sergeeva, Eur. J. Mineral. **6**, 967 (1994).

[131] P. Atkins and J. de Paula, *Atkins' Physical Chemistry* (OUP Oxford, 2010).

[132] 4600&4700 general pourpose pressure vessels, Parr Instrument Company.

[133] M. Yasaka, Rigaku Journal **26 (2)**, (2010).

[134] M. Birkholz, *Thin Film Analysis by X-Ray Scattering* (Wiley-VCH Verlag GmbH & Co. KGaA, 2006).

[135] H. Kiessig, Ann. Phys. **402**, 769 (1931).

[136] A. Einstein, Ann. Phys. **322**, 132 (1905).

[137] J. Moulder, W. Stickle, P. Sobol, and K. Bomben, *Handbook of X-ray Photoelectron Spectroscopy* (Perkin-Elmer: Eden Prairie, 1992).

[138] P. van der Heide, *X-Ray Photoelectron Spectroscopy* (John Wiley & Sons, Inc., 2011).

[139] A. G. O'Donnell, I. M. Young, S. P. Rushton, M. D. Shirley, and J. W. Crawford, Nat. Rev. Microbiol. **5**, 689 (2007).

[140] S. Foner, Rev. Sci. Instrum. **30**, 548 (1959).

[141] B. D. Josephson, Rev. Mod. Phys. **46**, 251 (1974).

[142] J. Clarke, Proc. IEEE **61**, 8 (1973).

[143] J. Rodriguez-Carvajal, *FULLPROF: A Rietveld Refinement and Pattern Matching Analysis Program, Laboratory Leon Brillouin (CEA-CNRS), France*, 2011.

[144] P. Mohn and S. Matar, J. Magn. Magn. Mater. **191**, 234 (1999).

[145] J. L. Costa-Krämer, D. M. Borsa, J. M. García-Martín, M. S. Martín-González, D. O. Boerma, and F. Briones, Phys. Rev. B **69**, 144402 (2004).

[146] R. Loloee, K. R. Nikolaev, and W. P. Pratt, Appl. Phys. Lett. **82**, 3281 (2003).

[147] C. Guillaud and H. Creveaux, Compt. Rend. Acad. Sci. (Paris) 1170 (1946).

[148] X. Wang, W. Zheng, H. Tian, S. Yu, and L. Wang, J. Magn. Magn. Mater. **283**, 282 (2004).

[149] C. Navio, J. Alvarez, M. J. Capitan, D. Ecija, J. M. Gallego, F. Yndurain, and R. Miranda, Phys. Rev. B **75**, 125422 (2007).

[150] E. J. Miola, S. D. de Souza, P. A. Nascente, M. Olzon-Dionysio, C. A. Olivieri, and D. Spinelli, Appl. Surf. Sci. **144-145**, 272 (1999).

[151] W. Diekmann, G. Panzner, and H. Grabke, Surf. Sci. **218**, 507 (1989).

[152] H. Takahashi, M. Igarashi, A. Sakuma, and Y. Sugita, IEEE Trans. Magn. **36**, 2921 (2000).

[153] Y. Takahashi, M. Katou, H. Shoji, and M. Takahashi, J. Magn. Magn. Mater. **232**, 18 (2001).

[154] Y. Komasaki, M. Tsunoda, S. Isogami, and M. Takahashi, J. Appl. Phys. **105**, (2009).

[155] R. Stephan, S. Zabrocki, P. Wetzel, D. Berling, A. Mehdaoui, J.-L. Bubendorff, G. Garreau, C. Pirri, G. Gewinner, N. Boudet, and J. Berar, Surf. Sci. **600**, 3003 (2006).

[156] N. Tournerie, P. Schieffer, B. Lépine, C. Lallaizon, P. Turban, and G. Jézéquel, Phys. Rev. B **78**, 134401 (2008).

[157] J. Buschbeck, I. Opahle, M. Richter, U. K. Rößler, P. Klaer, M. Kallmayer, H. J. Elmers, G. Jakob, L. Schultz, and S. Fähler, Phys. Rev. Lett. **103**, 216101 (2009).

[158] N. Ji, L. F. Allard, E. Lara-Curzio, and J.-P. Wang, Appl. Phys. Lett. **98**, (2011).

[159] F. Tessier, A. Navrotsky, R. Niewa, A. Leineweber, H. Jacobs, S. Kikkawa, M. Takahashi, F. Kanamaru, and F. DiSalvo, Solid State Sci. **2**, 457 (2000).

[160] S. Yamamoto, R. Gallage, Y. Ogata, Y. Kusano, N. Kobayashi, T. Ogawa, N. Hayashi, K. Kohara, M. Takahashi, and M. Takano, Chem. Commun. **49**, 7708 (2013).

[161] L. Vegard, Z. Phys. **5**, 17 (1921).

[162] Y. D. Zhang, J. I. Budnick, W. A. Hines, M. Q. Huang, and W. E. Wallace, Phys. Rev. B **54**, 51 (1996).

[163] M. Takahashi and H. Shoji, J. Magn. Magn. Mater. **208**, 145 (2000).

[164] N. Ji, V. Lauter, X. Zhang, H. Ambaye, and J.-P. Wang, Appl. Phys. Lett. **102**, (2013).

[165] M.-Z. Huang and W. Y. Ching, Phys. Rev. B **51**, 3222 (1995).

[166] Y. Martin and H. K. Wickramasinghe, Appl. Phys. Lett. **50**, 1455 (1987).

[167] F. Virot, L. Favre, R. Hayn, and M. D. Kuz'min, J. Phys. D: Appl. Phys. **45**, 405003 (2012).

[168] S. Chikazumi, *Physics of Ferromagnetism*, 2nd ed. (Clarendon Press, 1997).

[169] R. Skomski, *Simple Models of Magnetism* (Oxford University Press, 2008).

[170] B. Predel, Cu-Fe (Copper-Iron): Datasheet from Landolt-Börnstein - Group IV Physical Chemistry · Volume 5D: “Cr-Cs – Cu-Zr” in SpringerMaterials (http://dx.doi.org/10.1007/10086090_1073), copyright 1994 Springer-Verlag Berlin Heidelberg.

[171] K. Sumiyama, Y. Nakamura, and K. Tanaka, Hyperfine Interact. **53**, 143 (1990).

[172] S. F. Matar, C. R. Chim. **5**, 539 (2002).

[173] S. Ishida, K. Kitawatase, S. Fujii, and S. Asano, J. Phys.: Condens. Matter **4**, 765 (1992).

[174] W. Zhou, L.-j. Qu, Q.-m. Zhang, and D.-s. Wang, Phys. Rev. B **40**, 6393 (1989).

[175] P. Bruno, Phys. Rev. B **39**, 865 (1989).

[176] Y. Jiang, V. Dabade, M. P. Brady, O. Rios, R. D. James, and J.-P. Wang, J. Appl. Phys. **115**, (2014).

[177] Y. Watanabe, A. Nakano, and A. Sato, Mater. Sci. Eng. A **146**, 151 (1991).

[178] G. Sauthoff and W. Pitsch, Philos. Mag. B **56**, 471 (1987).

[179] T. Koyano, H. Ikeda, R. Yoshizaki, K. Uehara, A. Tasaki, H. Ohtsuka, T. Takamasu, H. Wada, G. Kido, and T. Ohba, Mater. Trans., JIM **41**, 923 (2000).

[180] M. Takahashi, H. Shoji, H. Takahashi, T. Wakiyama, M. Kinoshita, and W. Ohta, IEEE Transactions on Magnetics **29**, 3040 (1993).

[181] K. Helmut and F. Manfred, *Micromagnetism and the Microstructure of Ferromagnetic Solids* (New York, Cambridge University Press, 2003).

[182] K. M. Krishnan, IEEE Trans. Magn. **46**, 2523 (2010).

[183] ASTM International. ASTM E112-13 Standard Test Methods for Determining Average Grain Size. West Conshohocken, PA: ASTM International, 2013.

[184] R. Skomski and J. Coey, Scr. Mater. **112**, 3 (2016).

[185] J. M. D. Coey, Phys. Rev. Lett. **27**, 1140 (1971).

[186] C.-M. Hsu, H.-M. Lin, K.-R. Tsai, and P.-Y. Lee, J. Appl. Phys. **76**, 4793 (1994).

[187] E. C. Stoner and E. P. Wohlfarth, Phil. Trans. R. Soc. A **240**, 599 (1948).

[188] W. F. Brown, Phys. Rev. **105**, 1479 (1957).

[189] H. Kronmüller, Phys. Status Solidi B **144**, 385 (1987).

[190] F. Bødker, S. Mørup, and S. Linderoth, Phys. Rev. Lett. **72**, 282 (1994).

[191] G. Asti and S. Rinaldi, Phys. Rev. Lett. **28**, 1584 (1972).

[192] G. Asti and S. Rinaldi, J. Appl. Phys. **45**, 3600 (1974).

[193] S. Arajs and R. V. Colvin, J. Appl. Phys. **35**, 2424 (1964).

[194] P. Talagala, P. S. Fodor, D. Haddad, R. Naik, L. E. Wenger, P. P. Vaishnava, and V. M. Naik, Phys. Rev. B **66**, 144426 (2002).

[195] V. Nefedov, Y. Salyn, G. Leonhardt, and R. Scheibe, J. Electron Spectrosc. Relat. Phenom. **10**, 121 (1977).

[196] H. Park, P. Ayala, M. A. Deshusses, A. Mulchandani, H. Choi, and N. V. Myung, Chem. Eng. J. **139**, 208 (2008).

[197] C. C. Ahn, *Transmission Electron Energy Loss Spectrometry in Materials Science and The EELS Atlas*, second edition ed. (Wiley-VCH Verlag GmbH & Co. KGaA, 2004).

[198] J. P. Wang, S. He, and Y. Jiang, Iron nitride permanent magnet and technique for forming iron nitride permanent magnet, 2013, WO Patent App. PCT/US2012/051,382.

[199] D. Matthiesen, Transformation Enabled Nitride Magnets Absent Rare Earths and a Process of Making the Same, 2014, US Patent App. 14/304,102.

[200] S. Yamamoto, M. Takano, M. Takahashi, T. Ogawa, and N. Kobayashi, Process for producing ferromagnetic iron nitride particles, anisotropic magnet, bonded magnet and compacted magnet, 2014, US Patent App. 14/346,338.

[201] A. Aharoni, J. Appl. Phys. **83**, 3432 (1998).

[202] R. Coehoorn, D. de Mooij, and C. de Waard, J. Magn. Magn. Mater. **80**, 101 (1989).

[203] E. F. Kneller and R. Hawig, IEEE Trans. Magn. **27**, 3588 (1991).

[204] R. Skomski and J. M. D. Coey, Phys. Rev. B **48**, 15812 (1993).

[205] T. Schrefl, H. Kronmüller, and J. Fidler, J. Magn. Magn. Mater. **127**, L273 (1993).

[206] B. Balasubramanian, P. Mukherjee, R. Skomski, P. Manchanda, B. Das, and D. J. Sellmyer, Sci. Rep. **4**, 6265 (2014).

[207] D. J. D. Bitetto, J. Appl. Phys. **35**, 3482 (1964).

[208] H. Kronmüller, R. Fischer, M. Bachmann, and T. Leineweber, J. Magn. Magn. Mater. **203**, 12 (1999).

[209] World Cancer Report 2014. Geneva, Switzerland: World Health Organization, International Agency for Research on Cancer, WHO Press, 2015.

[210] National Cancer Institute, Cancer Statistics, https://www.cancer.gov/about-cancer/understanding/statistics/, accessed on 09.01.2017.

[211] D. Ortega and Q. A. Pankhurst, *Nanoscience: Volume 1: Nanostructures through Chemistry* (The Royal Society of Chemistry, 2013), Vol. 1, pp. 60–88.

[212] Y. Rabin, Int. J. Hyperthermia **18**, 194 (2002).

[213] P. Keblinski, D. Cahill, A. Bodapati, C. Sullivan, and T. Taton, J. Appl. Phys. **100**, (2006).

[214] R. K. Gilchrist, R. Medal, W. D. Shorey, R. C. Hanselman, J. C. Parrott, and C. B. Taylor, Ann. Surg. **146(4)**, 596 (1957).

[215] H. J. Richter, J. Phys. D: Appl. Phys. **32**, R147 (1999).

[216] A. Moser, K. Takano, D. T. Margulies, M. Albrecht, Y. Sonobe, Y. Ikeda, S. Sun, and E. E. Fullerton, J. Phys. D: Appl. Phys. **35**, R157 (2002).

[217] D. Weller and A. Moser, IEEE Trans. Magn. **35**, 4423 (1999).

[218] A. Moser, D. Weller, and M. F. Doerner, Appl. Phys. Lett. **75**, 1604 (1999).

[219] D. Weller and M. F. Doerner, Annu. Rev. Mater. Sci. **30**, 611 (2000).

[220] H. Richter and A. Dobin, J. Magn. Magn. Mater. **287**, 41 (2005).

[221] K. Z. Gao, O. Heinonen, and Y. Chen, J. Magn. Magn. Mater. **321**, 495 (2009).

[222] G. Scheunert, O. Heinonen, R. Hardeman, A. Lapicki, M. Gubbins, and R. M. Bowman, Appl. Phys. Rev. **3**, 011301 (2016).

[223] J.-U. Thiele, S. Maat, and E. E. Fullerton, Appl. Phys. Lett. **82**, 2859 (2003).

[224] D. Suess, Appl. Phys. Lett. **89**, 113105 (2006).

[225] F. B. Hagedorn, J. Appl. Phys. **41**, 2491 (1970).

Curriculum Vitae

Personal information	
Name	Imants Dirba
Date of birth	11 June, 1987
Place of birth	Riga, Latvia
Citizenship	Latvian
Education	
03.2013 - 06.2017	Ph. D. in Materials Science TU Darmstadt, Darmstadt, Germany
09.2009 - 07.2011	M. Sc. in Physics University of Latvia, Riga, Latvia
09.2005 - 07.2008	B. Sc. in Physics University of Latvia, Riga, Latvia
07.2005	General Certificate of Secondary Education Agenskalna State Gymnasium, Riga, Latvia
Research interests	
	Advanced synthesis and characterization of functional magnetic materials
	Magnetic thin films
	Net-shape production of anisotropic Nd-Fe-B magnets
	Exchange-coupled nanocomposites
	Interstitial modification of rare earth-transition metal alloys
	Magnetic nanoparticles for biomedicine applications
Conferences	
	INTERMAG 2017, Dublin, Ireland, Oral presentation
	REPM 2016, Darmstadt, Germany, Oral presentation
	DPG-Frühjahrstagung 2016, Regensburg, Germany, Poster presentation
	INTERMAG 2015, Beijing, China, Oral presentation

DPG-Frühjahrstagung 2014, Dresden, Germany, Oral presentation

MMM 2013, Denver, USA, Oral presentation

JEMS 2013, Rhodes, Greece, Oral presentation

MMM/Intermag 2013, Chicago, USA, Oral presentation

Own publications

Peer-reviewed publications

H. Zhang, **I. Dirba**, T. Helbig, L. Alff, and O. Gutfleisch, *Engineering perpendicular magnetic anisotropy in Fe via interstitial nitrogenation: N choose K*, APL Materials **4**, 116104 (2016)

I. Dirba, C.A. Schwöbel, L.V.B. Diop, M. Duerrschnabel, L. Molina-Luna, K. Hofmann, P. Komissinskiy, H.-J. Kleebe, O. Gutfleisch, *Synthesis, morphology, thermal stability and magnetic properties of α''-$Fe_{16}N_2$ nanoparticles obtained by hydrogen reduction of γ-Fe_2O_3 and subsequent nitrogenation*, Acta Mater. **123**, 214-222 (2017)

I. Dirba, P. Komissinskiy, O. Gutfleisch and L. Alff, *Increased magnetic moment induced by lattice expansion from α-Fe to α'-Fe_8N*, J. Appl. Phys. **117**, 173911 (2015)

I. Dirba, M. Baghaie Yazdi, A. Radetinac, P. Komissinskiy, S. Flege, O. Gutfleisch, L. Alff, *Growth, structure and magnetic properties of γ'-Fe_4N thin films*, J. Magn. Magn. Mater. **379**, 151-155 (2015)

S. Sawatzki, **I. Dirba**, H. Wendrock, L. Schultz, O. Gutfleisch, *Diffusion processes in hot-deformed Nd-Fe-B magnets with DyF_3 additions*, J. Magn. Magn. Mater. **358**, 163-169 (2014)

I. Dirba, S. Sawatzki, O. Gutfleisch, *Net-shape and crack-free production of Nd-Fe-B magnets by hot deformation*, J. Alloys Compd. **589**, 301-306 (2014)

S. Sawatzki, **I. Dirba**, L. Schultz, O. Gutfleisch, *Electrical and magnetic properties of hot-deformed Nd-Fe-B magnets with different DyF_3 additions*, J. Appl. Phys. **114**, 133902 (2013)

Acknowledgments

First, I would like to thank my Ph.D. supervisor, Prof. Dr. Oliver Gutfleisch, for giving me the opportunity to do research in his group at the IFW Dresden and continue here at the TU Darmstadt. I was given noteworthy scientific freedom, provided with an environment to work on various exciting research topics and develop my own ideas. This time has been a truly great experience, encouraging growth, both personally and professionally.

I want to thank Prof. Dr. Rainer Niewa, who kindly agreed to review my doctoral thesis.

I am thankful to Prof. Dr. Lambert Alff for supporting my thin film studies.

I thank all the members of the Functional Materials group. Special thanks to Dr. Konstantin Skokov for numerous interesting research activities, Dr. Iliya Radulov for the PPMS, Tim Helbig for the MFM, and Christoph Schwöbel for the SEM measurements. I am grateful to Dr. Leopold Diop for many fruitful discussions about phenomena of magnetism in the solid state. Additionally, I thank Dr. Konrad Löwe, Dr. Semih Ener and Maximilian Fries for correcting my thesis. I also thank Marc Pabst and Bernd Stoll for their substantial practical help with the experimental equipment. I very much enjoyed working together.

I had the opportunity to collaborate with many other researchers from the department of Materials Science. I thank Jun. Prof. Hongbin Zhang for the theoretical insights, Mehrdad Baghaie Yazdi for the productive and fun time with magnetron sputtering, Dr. Philipp Komissinskiy for the XPS, Dr. Stefan Flege for the SIMS, and Claudia Fasel for the DSC measurements. I am thankful to Dr. Aldin Radetinac for the advice on thin film XRD, Mahdad Mohammadi for his essential help with the nanocomposites, Sandra Schäfer for the nanowires study, Dr. Shrikant Bhat for the high-pressure experiments, Dr. M. Duerrschnabel and Dr. L. Molina-Luna for the TEM investigations, as well as Jean-Christophe Jaud for his patience with having to change the XRD capillary setup frequently.

I also want to thank Franziska Scheibel from the University of Duisburg-Essen for the FMR, Yu-Chun Chen from the Max Planck Institute for Intelligent Systems, Stuttgart for the XMCD, Prof. Olivier Isnard from the Institut NEEL, Grenoble, France for the neutron diffraction, and Prof. Franca Albertini from the Institute of Materials for Electronics and Magnetism (IMEM), Parma, Italy for the SPD measurements.

My thanks go to the BMBF for financial support within the project KomMa, 03X3582 for funding my thesis.